UNIVERSITÀ DEGLI STUDI DI PADOVA

Dipartimento di Fisica e Astronomia "Galileo Galilei"

Master Degree in Astrophysics and Cosmology

Final dissertation

Axion Dynamics Across First-Order Phase Transitions

Supervisor:
Prof. Francesco D'Eramo
Co-supervisors:
Dr. Ville Vaskonen

Candidate:
Galymzhan Baltabay
Student ID: **2071414**

Academic Year 2024/2025

Abstract

In this work, we study axion dynamics during first-order phase transitions and investigate the bubble misalignment mechanism. First, we review the evidence for dark matter at different scales and explore various dark matter production mechanisms, including thermal and non-thermal relics. Then, we discuss the key theoretical framework of quantum field theory at finite temperature to understand phase transitions in the early universe, with specific attention to bubble nucleation and expansion processes that characterize first-order transitions. We then introduce the axion as a solution to the strong CP problem and explore its properties, interactions, and production processes, including the conventional misalignment mechanism. The main focus of this work is to analyze the bubble misalignment mechanism, in which axions interact with expanding bubble walls during a first-order phase transition. We classify different dynamical regimes based on the hierarchy between the Hubble parameter, axion masses, and phase transition duration. Through analytical calculations and numerical simulations, we demonstrate that axion waves undergo Fermi acceleration when reflecting off the bubble walls, eventually gaining sufficient energy to penetrate the bubbles. This mechanism modifies the axion abundance and momentum distribution compared to standard scenarios. Finally, our novel analysis of multiple bubble simulations shows how the number density of axions scales with the bubble wall velocity and bubble number with important implications for the axion dark matter abundance. These results contribute to our understanding of axion dynamics in the early universe and may have implications for the parameter space of axion searches.

Introduction

Our present understanding of the universe requires the existence of dark matter (DM), a non-luminous element that makes up approximately 27% of the cosmic energy budget. Despite considerable experimental and theoretical work spanning many years, the essential characteristics of DM continue to be one of the key unresolved issues in physics. Observational evidence from galactic rotation curves, galaxy clusters, gravitational lensing, and the cosmic microwave background consistently indicates the presence of this exotic component, yet its particle physics origin continues to elude detection.

Unlike many particles proposed solely to account for cosmic mass discrepancies, the axion emerges with substantial theoretical motivation due to its origins in resolving fundamental problems within particle physics. While the axion was originally proposed as a solution to the strong CP problem in quantum chromodynamics (QCD), it satisfies the necessary DM constraints. This theoretical foundation gives axions a compelling advantage that distinguishes them from other candidate particles, as they simultaneously resolve a fundamental issue in particle physics while potentially accounting for the observed DM abundance.

The axion arises from the Peccei-Quinn mechanism, which dynamically explains why the strong nuclear force preserves CP symmetry even though the Standard Model allows its violation. This mechanism introduces a new global $\mathrm{U}(1)_{\mathrm{PQ}}$ symmetry which, when spontaneously broken, produces a pseudo-Nambu-Goldstone boson - the axion. Crucially, the $U(1)_{\mathrm{PQ}}$ symmetry is anomalous under QCD, meaning that while the classical theory respects this symmetry, quantum effects break it through the chiral anomaly. This anomaly creates an essential coupling term $\theta G\tilde{G}$, allowing the axion to interact with gluon field configurations and QCD instantons. Its coupling to gluons produces a small mass and a potential after confinement that dynamically drives the CP-violating parameter to zero. The properties that make the axion an elegant solution to this particle physics puzzle also make it an excellent DM candidate, since its weak couplings and potential for non-thermal production fit well with DM requirements.

The aim of this work is to investigate the bubble misalignment mechanism that can increase axion abundance compared to standard production scenarios. Nakagawa et al. [1] first showed that discontinuous mass changes during first-order phase transitions (FOPTs) can increase axion production. Lee et al. [2] extended this analysis by explicitly modelling bubble formation and coalescence. Building upon this foundation, this thesis provides significant extensions to the theoretical framework and develops comprehensive numerical simulations that go beyond previous work. Our novel contributions include: detailed multi-bubble simulations that verify the predicted $N^{1/3}$ scaling of axion number density with bubble count, implementation of dynamic bubble wall evolution incorporating axion pressure feedback effects, and systematic investigation of different velocity regimes revealing distinct scaling behaviors. We further develop the theoretical understanding of axion shock wave formation and provide the first numerical verification of Fermi acceleration mechanisms in realistic multi-bubble environments.

In Chapter 1 we review the evidence for DM at different scales, from galactic rotation curves to the cosmic microwave background. We examine production mechanisms, both thermal and non-thermal relics.

Chapter 2 introduces finite-temperature quantum field theory to understand phase transitions in the early universe. We focus on first-order phase transitions, bubble nucleation and bubble expansion. We use the thin-wall approximation and study the dynamics of the walls in the surrounding plasma. These concepts help to understand transitions through bubble nucleation and expansion.

Chapter 3 explores the axion as a solution to the strong CP problem. We discuss the CP problem in QCD and how the Peccei-Quinn mechanism solves it. We examine axion properties, interactions with Standard Model particles, and standard production mechanisms such as misalignment. We also review constraints from experiments, astrophysical observations and cosmology that establish axion as a viable DM candidate.

Chapter 4 is the main focus of this thesis, where we analyze the bubble misalignment mechanism. We classify axion dynamics during FOPTs into different regimes based on the hierarchy between Hubble parameter, axion masses and transition duration. Our analysis shows how axion waves reflect and transmit through bubble walls, undergo Fermi acceleration and form shock waves in certain regimes. We implement multi-bubble simulations that verify axion number density scales with bubble number as $N^{1/3}$ and exhibit velocity dependent scaling. Our analysis extended to simulations where bubble wall dynamics incorporate feedback from axion-induced pressure. These simulations demonstrated that bubble walls rapidly accelerate to near-luminal velocities ($v \approx 1$) before experiencing significant deceleration as the accumulating axion pressure begins to counteract the vacuum energy driving the expansion.

This work advances understanding of axion production during FOPTs and has implications for axion DM phenomenology, particularly regarding abundance estimates and momentum distributions in cosmological scenarios involving phase transitions.

Contents

Chapter 1

What is Dark Matter?

State-of-the-art cosmological models rely on non-standard matter, which we call dark matter (DM), to explain a variety of astronomical observations. The nature of this matter remains an open question, as despite numerous search attempts, it has evaded all detection attempts. In this chapter, we review the evidence at several cosmological scales that requires the addition of this "exotic" matter component. We then discuss possible theoretical frameworks for DM production and review current experimental approaches to detection.

1.1 Evidence for Dark Matter

DM evidence exists across multiple astronomical scales, with independent observations reinforcing its presence. From galactic rotation curves to cosmic microwave background anisotropies, these measurements provide compelling support for DM throughout the universe. The following subsections examine key observations at increasing distance scales that establish the need for this non-baryonic component.

1.1.1 The Galactic Rotation Curves

One of the most compelling pieces of evidence supporting the existence of DM comes from the unexpected gravitational effects observed in galactic rotation curves. A galaxy's rotation curve is a fundamental astrophysical tool that graphically represents the orbital velocities of visible matter (stars and gas) as a function of their radial distance from the galactic center. These empirical relationships provide crucial insights into the mass distribution and gravitational dynamics within galaxies [3]. From Newtonian dynamics, we can derive the expected behaviors of rotation curves. For an object of mass m on a circular orbit of radius r around the center of a galaxy, the object experiences a gravitational force given by:

$$F_{\mathrm{g}} = \frac{GmM(r)}{r^2}, \tag{1.1}$$

where $M(r)$ represents the total mass enclosed within the radius r. This treatment assumes spherical symmetry, which serves as a useful approximation for understanding galactic dynamics, particularly in the central bulge region where the mass distribution is more spherically symmetric. While real galaxies exhibit spiral structure and departures from perfect spherical symmetry, this approximation captures the essential physics of orbital motion under gravitational influence. This force provides the centripetal acceleration:

$$a_c = \frac{v_{\rm circ}^2(r)}{r}, \tag{1.2}$$

where $v_{\rm circ}(r)$ is the circular velocity. Equating the gravitational force to the centripetal force, $F_g = ma_c$, expression can be simplified to $v_{\rm circ}(r) = \sqrt{\frac{GM(r)}{r}}$. The enclosed mass $M(r)$ is given by:

$$M(r) \equiv 4\pi \int_0^R \rho(r) r^2 \, dr, \tag{1.3}$$

where $\rho(r)$ is the mass density. For visible matter concentrated in the galactic bulge and disk, we expect $M(r)$ to approach a constant value beyond the visible disk, leading to a Keplerian decline in velocity $v_{\rm circ}(r) \propto r^{-1/2}$. However, observations of galactic rotation curves reveal a striking phenomenon: the velocity profile remains approximately constant even at large radii, well beyond the visible extent of the galaxy (see Fig. 1.1). This discrepancy between the expected Keplerian decline and the observed flat rotation curves implies the presence of an additional mass component distributed in an extended halo around the galaxy. To reconcile these observations with gravitational theory, the mass profile of galaxies must be approximately proportional to radius, extending well beyond the visible disk. This requirement naturally explains the observed flat rotation curves. The most widely accepted explanation for this phenomenon is the presence of a DM halo surrounding the visible galaxy.

From this evidence, we can infer several characteristics of DM. Since this matter remains undetected through electromagnetic observations despite its substantial gravitational influence, its interaction with ordinary matter and radiation should be minimal. The persistence of these stable halo structures over billions of years indicates that it must be stable on cosmological timescales, limiting the potential for self-interaction.

Alternative theories, particularly Modified Newtonian Dynamics (MOND), have been proposed to explain these observations without invoking DM. MOND suggests that Newton's laws of gravity require modification at the low accelerations typical of galactic scales. Although MOND can successfully explain some aspects of galactic dynamics, it faces significant challenges in accounting for other astronomical phenomena, such as gravitational lensing in galaxy clusters, the dynamics of galaxy clusters themselves, and the observed features in the cosmic microwave background. These limitations, combined with the success of DM in explaining a broad range of astronomical observations across different scales, have led to widespread acceptance of DM as the most promising solution to the rotation curve problem.

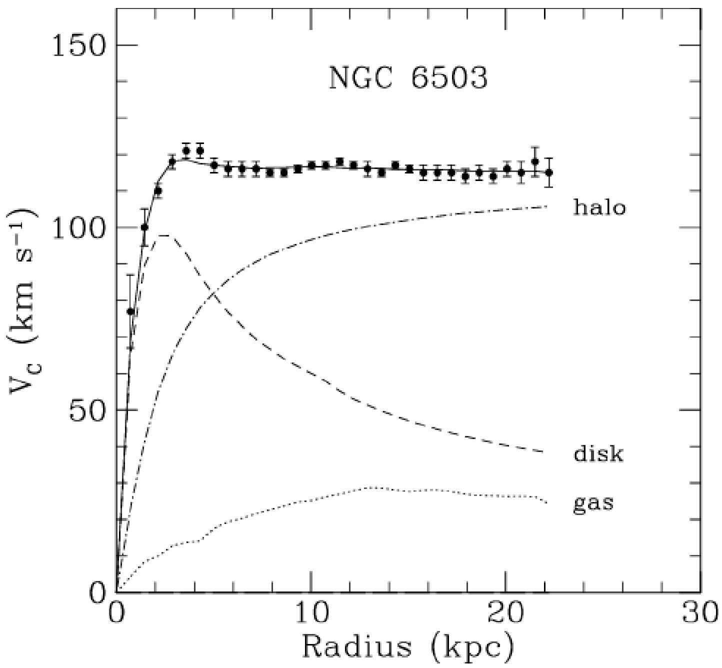

Figure 1.1: NGC6503 rotation curve. The dotted line represents the contribution from the gas, the dashed from the galaxy disk, and the dash-dotted line from the DM halo. Figure from [4]

1.1.2 Galaxy Clusters

The total mass of galaxy clusters can be determined by three primary methods. First, astronomers apply the virial theorem to observed velocity distributions which relates the kinetic energy of galaxies to the gravitational potential of the cluster. Second, they study X-ray emission profiles from hot intracluster gas, which reveals how the gas is distributed in the gravitational potential well of the cluster. Third, they analyze weak gravitational lensing effects, where the cluster's mass distorts the images of background galaxies, allowing for direct mapping of the total mass distribution. Each of these independent methods consistently indicates the presence of substantially more mass than can be accounted for by visible matter alone.

Virial Theorem Analysis

The earliest evidence for DM in galaxy clusters emerged from Fritz Zwicky's pioneering work in the 1930s [5]. Through his study of velocity dispersion in the Coma cluster, Zwicky applied the virial theorem, which establishes a fundamental relationship between the average kinetic energy and potential energy of a system:

$$\langle K \rangle = -\frac{1}{2}\langle V \rangle. \tag{1.4}$$

Modeling galaxy clusters as spheres of constant density ρ and radius R, the average potential energy can be expressed as:

$$\langle V \rangle = -\int_0^R 4\pi r^2 \rho \frac{GM(r)}{r} dr = -\frac{3GM^2}{5R}, \tag{1.5}$$

where $M(r)$ follows from Eq. (1.3) with an assumption of constant density. The kinetic energy term takes the form:

$$\langle K \rangle = \frac{1}{2}\sum_i^N m_i v_i^2 = \frac{1}{2}M\langle v^2 \rangle = \frac{3}{2}M\sigma_v^2, \tag{1.6}$$

with σ_v representing the velocity dispersion. Here, the assumption of isotropic velocities gives $\langle v_x^2 \rangle = \langle v_y^2 \rangle = \langle v_z^2 \rangle = \sigma_v^2$, yielding $\langle v^2 \rangle = 3\sigma_v^2$. Combining Eq. (1.5) and Eq. (1.6) with the virial theorem:

$$2\left(\frac{3}{2}M\sigma_v^2\right) - \frac{3GM^2}{5R} = 0, \tag{1.7}$$

leads to a relation for the total mass $M = \frac{5R\sigma_v^2}{G}$. Zwicky's application of this formula to observed values of σ_v and R yielded mass estimates that far exceeded the visible mass, providing the first indication of DM in clusters.

X-ray Emission Analysis

Since the 1980s, X-ray observations have emerged as a powerful method for assessing the distribution of both ordinary and dark matter in galaxy clusters. These clusters contain large amounts of ionized hydrogen and helium gas. As this gas falls into the gravitational potential well of the cluster, it undergoes shock heating and adiabatic compression, reaching temperatures of $T_{gas} \sim m_p v_{esc}^2 \sim 10\,\mathrm{keV} \sim 10^8\,\mathrm{K}$. Despite such high temperatures, nuclear fusion remains negligible because of the low ambient density. Instead, the hot gas primarily emits X-rays through thermal bremsstrahlung radiation. Assuming spherical symmetry and hydrostatic equilibrium, we can write the equation relating the gas pressure gradient to the gravitational potential:

$$\frac{1}{\rho_{\mathrm{gas}}(r)}\frac{dP}{dr} = -\frac{d\phi}{dr} = -\frac{GM(r)}{r^2}, \tag{1.8}$$

where $\rho_{gas}(r)$ is the gas density and $M(r)$ represents the total gravitating mass (including both the gas and DM) within radius r. For this intracluster gas, we can apply the ideal gas law:

$$P = \frac{\rho_{\mathrm{gas}} k T_{\mathrm{gas}}}{\mu m_p}, \tag{1.9}$$

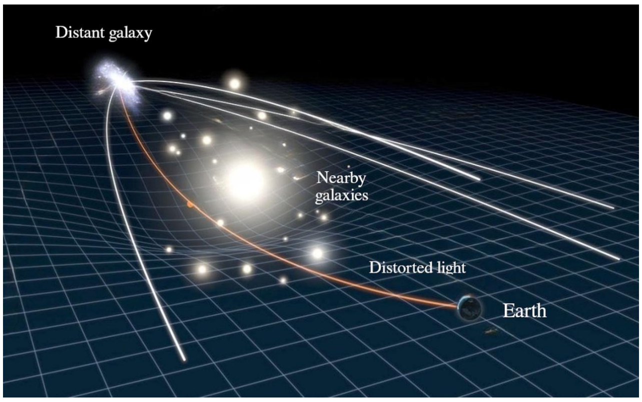

Figure 1.2: Illustration of the gravitational lensing phenomenon. The gravity of the nearby galaxy and the DM surrounding it acts like a lens, bending the light of the distant galaxy. Credit:NASA, ESA and L.Calcada.

where $\mu \approx 0.6$ is the mean molecular weight for a typical mixture of 75% hydrogen and 25% helium. The crucial observables in this analysis are the gas density, which is determined from the X-ray intensity profile, and the gas temperature, which is measured from the X-ray spectrum. Together, these measurements allow astronomers to reconstruct the gravitational potential and mass distribution throughout the cluster, revealing the substantial presence of the DM component in explaining the observed gas properties. From these measurements and Eq. (1.8), we can reconstruct the total cluster mass profile:

$$M(r) = -\frac{kT_{\text{gas}} r}{G\mu m_p} \left(\frac{d \ln \rho_{\text{gas}}}{d \ln r} + \frac{d \ln T_{\text{gas}}}{d \ln r} \right). \tag{1.10}$$

In essence, X-ray observations provide a microscopic analog to Zwicky's method: instead of using galaxy velocities, we use the temperature (kinetic energy) of gas molecules to infer the total gravitating mass of the cluster. This independent line of evidence strongly supports the presence of DM in galaxy clusters.

Gravitational Lensing and the Bullet Cluster

Gravitational lensing provides perhaps the most direct evidence for DM. Based on general relativity, massive objects bend light rays by curving spacetime (Fig. 1.2). This effect allows astronomers to map the total mass distribution, including DM, in astronomical systems. The Bullet Cluster (1E0657-56) presents particularly compelling evidence for DM. Located 3.7 Gyr away, this system of colliding clusters exhibits a striking separation between its baryonic and total mass distributions (Fig. 1.3). X-ray observations reveal the distribution of hot gas, whereas weak lensing maps the total mass distribution. During the collision approximately 150 million years ago, the clusters' baryonic components interacted through electromagnetic forces, creating a distinctive shock wave pattern. However, the DM components, which interact only gravitationally, passed through each other largely undisturbed,

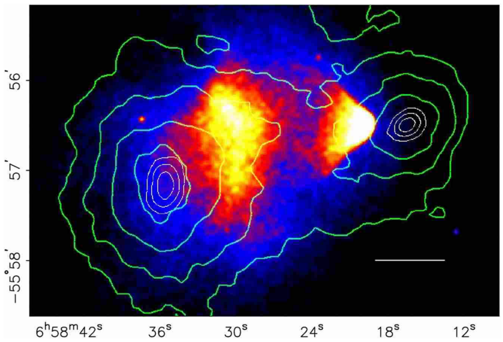

Figure 1.3: Bullet cluster (1E0657-56). Collision of two galaxy clusters where colored map represents the X-ray image of the hot baryonic gas and green contours represents displaced distribution of the total mass obtained from the weak lensing. Figure from [6].

resulting in the observed separation between the bulk of the mass and the visible matter. This spatial separation between the collisional (baryonic) and collisionless (dark) components provides strong evidence for the existence of DM. Subsequently, similar systems have been discovered [7], strengthening this line of evidence.

1.1.3 Cosmological Scales

The mismatch between observed galactic rotation curves and predictions based on visible matter alone, along with galaxy cluster temperature profiles, indicates substantial unseen matter. These smaller-scale observations align with evidence from larger cosmological scales, which we explore in this section.

Large Scale Structure formation

The standard cosmological model relies on homogeneity and isotropy on a large scale, which is not true at small scales due to structures. Galaxy surveys show a variety of structures, voids, and filaments. To understand structure formation and describe the role of DM in it, this subsection briefly shows that ordinary matter alone cannot form structures observed today and cannot drive the growth of primordial inhomogeneities. Dark matter plays this crucial role because it lacks standard interactions with radiation. While baryonic matter remains coupled to the radiation field until recombination ($z \approx 1100$), DM decouples much earlier and begins seeding the gravitational wells that later develop into galaxies and clusters.

To provide a quantitative analysis of the process, we need to study the interplay between gravitational attraction and cosmic expansion that drives the growth of density fluctuations. The Jeans instability criterion essentially captures the nature of the competition between these two effects. For a static universe, the Jeans length describes the minimum scale at which pressure can counteract gravitational collapse, while for an expanding universe, the scales depend on the scale factor and the Hubble parameter [8].

The matter power spectrum $P(k)$ is a useful tool for quantifying the distribution of matter inhomogeneities at different scales. Firstly, it is a function of the wave number k and is inversely proportional to scale, which means that the larger k corresponds to a smaller physical scale. The high values for $P(k)$ at specific k represent the clustering strength on that scale, and we can use the dimensionless power spectrum $\Delta^2(k) = \frac{k^3 P(k)}{2\pi^2}$ to obtain a more pronounced representation of the clustering strength across different scales. Observations of the Cosmic Microwave Background show that primordial density fluctuations are at the order of $\delta \approx 10^{-5}$, which then seeds subsequent structure formations.

Jeans Analysis I: Static Universe

We first consider how density perturbations evolve in a static universe before incorporating expansion effects. The fluid dynamics in this Newtonian case can be described by three fundamental equations. The continuity equation,

$$\frac{\partial \rho}{\partial t} + \nabla \cdot (\rho \mathbf{v}) = 0, \tag{1.11}$$

ensures mass conservation by relating density changes to mass flow, where v represents the velocity field and ρ is the fluid density. The Euler equation,

$$\frac{\partial \mathbf{v}}{\partial t} + (\mathbf{v} \cdot \nabla)\mathbf{v} = -\frac{1}{\rho}\nabla P - \nabla \Phi, \tag{1.12}$$

describes the evolution of the velocity field under pressure and gravitational forces, ensuring momentum conservation. The Poisson equation,

$$\nabla^2 \Phi = 4\pi G \rho. \tag{1.13}$$

connects the mass density with the gravitational potential.

From these, we can derive the Jeans equation for the density contrast $\delta = \frac{\delta\rho}{\rho_0}$:

$$\frac{\partial^2 \delta}{\partial t^2} = c_s^2 \nabla^2 \delta + 4\pi G \rho_0 \delta. \tag{1.14}$$

To analyze this equation, we move to the Fourier space. Assuming a plane-wave solution for the perturbation of the form:

$$\delta \propto e^{i(\mathbf{k}\cdot\mathbf{r} - \omega t)},$$

the Fourier transform of $\nabla^2 \delta$ becomes $-k^2 \delta$, where k is the wavenumber. Substituting this into Eq. (1.14), we get:

$$\omega^2 \delta = (c_s^2 k^2 - 4\pi G \rho_0)\delta. \tag{1.15}$$

For perturbations to grow (δ increasing over time), the angular frequency ω^2 must be negative, which implies:

$$k^2 < \frac{4\pi G \rho_0}{c_s^2} \tag{1.16}$$

This defines the critical Jeans wavenumber and corresponding Jeans length:

$$k_J = \sqrt{\frac{4\pi G\rho_0}{c_s^2}}. \tag{1.17}$$

$$\lambda_J = \frac{2\pi}{k_J} = \sqrt{\frac{\pi c_s^2}{G\rho_0}}. \tag{1.18}$$

Perturbations with wavelengths exceeding λ_J undergo gravitational collapse, while smaller perturbations are stabilized by pressure.

Jeans Analysis II: Expanding Universe

In an expanding universe, the equations must be modified to account for cosmic expansion. The modified continuity, Euler, and Poisson equations become:

$$\frac{\partial \rho}{\partial t} + 3H\rho + \frac{1}{a}\nabla \cdot (\rho \mathbf{v}) = 0, \tag{1.19}$$

$$\frac{\partial \mathbf{v}}{\partial t} + H\mathbf{v} + \frac{1}{a}(\mathbf{v} \cdot \nabla)\mathbf{v} = -\frac{1}{a}\left(\frac{1}{\rho}\nabla P + \nabla \Phi\right), \tag{1.20}$$

$$\nabla^2 \Phi = 4\pi G \delta\rho. \tag{1.21}$$

where $H = \dot{a}/a$ is the Hubble parameter. In this framework, the Jeans criterion still applies, but the growth of perturbations is slowed due to the expansion of the universe. During the matter-dominated universe, these equations give a second-order differential equation for δ:

$$\frac{\partial^2 \delta}{\partial t^2} + 2H\frac{\partial \delta}{\partial t} = 4\pi G\rho_m \delta, \tag{1.22}$$

where ρ_m is the matter density, including contributions from baryons and DM. The general solution for $\delta(t)$ is:

$$\delta(t) = C_1 t^{2/3} + C_2 t^{-1}, \tag{1.23}$$

where C_1 and C_2 are constants determined by initial conditions. The term $t^{2/3}$ represents the growing mode, while t^{-1} represents the decaying mode. In the context of matter domination, we focus on the growing mode:

$$\delta(t) \propto t^{2/3}. \tag{1.24}$$

Using the relationship between time and the scale factor during matter domination, $a(t) \propto t^{2/3}$, this implies:

$$\delta(a) \propto a. \tag{1.25}$$

This shows that density perturbations grow linearly with the scale factor during the matter-dominated era.

The Critical Role of Dark Matter in Structure Formation

The main difference between baryons and DM lies in their coupling to radiation. Before recombination, baryonic matter is tightly coupled to photons through Thomson scattering, which prevents baryons from gravitationally clustering effectively. This coupling is maintained by radiation pressure, which supports the baryon-photon fluid against gravitational collapse. The sound speed for the baryon-photon fluid is given by:

$$c_s \approx \frac{1}{\sqrt{3(1+R)}}, \quad R = \frac{3\rho_b}{4\rho_\gamma}, \tag{1.26}$$

where R is the ratio of baryon to photon energy densities and it determines how perturbations propagate within it. The sound speed c_s reflects the effect of radiation pressure in resisting compression, smoothing out density perturbations on small scales. The radiation pressure suppresses perturbation growth for modes smaller than the horizon, leading to a damping effect known as Silk damping. As a result, baryonic matter cannot effectively cluster until after photon decoupling at $z \sim 1100$, when the universe cools sufficiently for neutral atoms to form. By this time, the horizon scale corresponds to structures as large as galaxy clusters, leaving smaller-scale structures unformed. Without DM, which does not couple to radiation and can gravitationally collapse earlier, the delay in baryonic clustering makes it impossible to account for the observed large-scale structure of the universe.

Cosmic Microwave Background Evidence for Dark Matter

The Cosmic Microwave Background provides powerful independent evidence for DM through its temperature anisotropies. These fluctuations are quantified by the angular power spectrum:

$$C_l = \frac{2}{\pi} \int_0^\infty dk k^2 P(k) |\Theta_l(k)|^2. \tag{1.27}$$

where $P(k)$ is the primordial power spectrum of density perturbations, and $\Theta_l(k)$ is the transfer function describing evolution of perturbations on scales corresponding to angular multipole momentum l. This equation links the observed power spectrum to the underlying physical processes, which are shaped by the gravitational influence of DM. While the detailed derivation of this expression requires a significant theoretical framework, we will skip the intricate details in this section and focus only on the necessary aspects to understand DM existence.

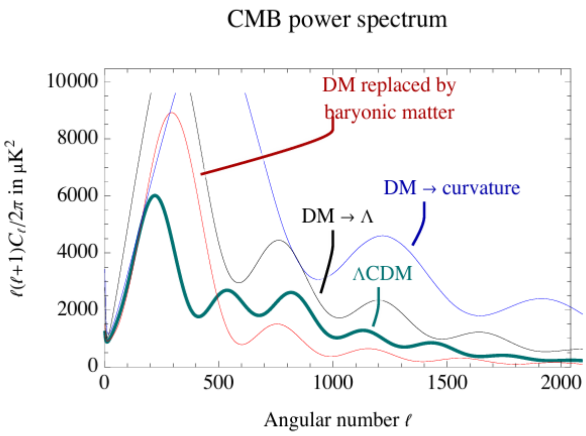

Figure 1.4: Effect of DM on the CMB angular power spectrum. Figure from [5]
.

Dark matter leaves several distinctive signatures in this spectrum. First, the DM potential wells anchor acoustic oscillations in the baryon-photon fluid, producing an asymmetry in peak heights. In Fig. 1.4, odd-numbered peaks represent compressions in gravitational wells and even-numbered peaks represent rarefactions. The plot shows the increased amplitude of the odd peaks compared to the even peaks. The position of the first peak constrains the sound horizon at matter-radiation equality and provides strong evidence for DM. The overall shape of the power spectrum constrains the cosmic matter density and provides evidence that baryonic matter alone is insufficient to account for the observed structure.

As shown in Fig. 1.4, the ΛCDM model (thick green line) accurately predicts the observed pattern of acoustic peaks and troughs. When the DM is replaced by an equivalent mass of baryonic matter (red line), the model fails to match the observations. This is due to the coupling of the baryonic matter with the radiation pressure prior to recombination. This coupling fundamentally alters the dynamics of the acoustic oscillations, as baryons and photons behave as a single fluid prior to recombination, leading to higher compression in overdense regions (first peak) while preventing the formation of the gravitational wells needed to sustain subsequent oscillations at the right amplitudes. Dark matter, decoupled from the radiation, provides the persistent gravitational potential needed to produce the observed peak pattern. The precise agreement between the ΛCDM model and the measurements thus provides compelling evidence that DM must account for about 26% of the energy content of the universe.

1.2 Dark Matter Production

In the previous section,we examined the observational evidence for DM across a range of cosmic scales, from galactic rotation curves to the cosmic microwave background. While the gravitational effects of DM are well established, its fundamental nature remains an open question. To improve our understanding of potential DM candidates, we need to consider how these particles could have been produced in the early universe. In this section, we explore different mechanisms for the production of DM, which are typically classified according to whether DM was ever in thermal equilibrium with the Standard Model plasma. We will first discuss thermal relics, focusing on the freeze-out mechanism, in which DM initially remains in equilibrium with the cosmic plasma before decoupling as the universe expands and cools. This includes both hot DM (which decouples while still relativistic) and cold DM (which decouples when non-relativistic), with particular emphasis on the WIMP paradigm. We then consider non-thermal production mechanisms, including freeze-in processes where DM is gradually produced from the thermal bath without ever reaching equilibrium. Additional non-thermal mechanisms such as the misalignment mechanism for axion-like particles will be discussed in detail in Chapter 3. Each production scenario implies different properties for DM particles, thus guiding experimental searches and theoretical developments.

1.2.1 Thermal Relics

For our first scenario, we consider thermal relics: DM particles which were in thermal equilibrium with primordial plasma. The evolution of these particles is governed by the Boltzmann equation that tracks the number density changes as the universe expands and interactions occur. The full Boltzmann equation can be written as:

$$\mathbb{L}(f) = \mathbb{C}(f) \tag{1.28}$$

where we denoted the Liouville ($\mathbb{L}(f) = \left(p^\mu \frac{\partial}{\partial x^\mu} - \Gamma^\mu_{\nu u} p^\nu p^u \frac{\partial}{\partial p^\mu}\right) f$) and the Collision $\mathbb{C}$ operator, as a function of f, which is the phase space distribution function. In the context of the expanding FLRW universe, and focusing on number density rather than the full distribution function, this simplifies to:

$$\frac{\partial}{\partial t} n(t) + 3Hn(t) = \frac{g}{(2\pi)^3} \int \frac{d^3p}{E} \mathbb{C}(f) \tag{1.29}$$

From Eq. (1.29), it is clear that if $\mathbb{C} = 0$, the particles do not interact and the number density evolution only depends on the expansion, which gives $n(t) \propto a^{-3}(t)$. If the equilibrium is broken, then the right-hand side term is nonzero and the equation takes the form:

$$\dot{n}_\chi(t) + 3Hn_\chi(t) = -\langle \sigma v \rangle (n_\chi^2 - n_{\chi_{eq}}^2) \tag{1.30}$$

where the right-hand side term represents the annihilation contribution. Generally, such processes can be written as $\chi\bar{\chi} \to \Psi\bar{\Psi}$, where the particle Ψ is considered to be in equilibrium with the thermal bath and in principle can have more interaction channels than χ. We also assume that $n_\chi = n_{\bar{\chi}}$ and $n_\Psi = n_{\bar{\Psi}}$. We introduce another useful quantity to isolate the effects of interactions from cosmic expansion: co-moving number density $Y = \frac{n_\chi}{s}$; where s is the entropy density. Introducing the variable $z = m_\chi/T$ (represents the mass-to-temperature ratio, not to be confused with cosmological redshift) to track cosmic cooling, the Boltzmann equation can be expressed as:

$$Y' = -\frac{\langle\sigma v\rangle sz}{H(z=1)}[Y^2 - Y_{eq}^2] \tag{1.31}$$

We now have the expression for the evolution of the DM abundance, and this allows us to distinguish between different production scenarios. Once the particle is decoupled from the thermal plasma, its abundance freezes at a value determined by the interaction rate at the time.

Hot Dark Matter

Having established the Boltzmann framework for tracking particle abundances in the expanding universe, we can now consider our first specific case: hot DM (HDM). This scenario occurs when DM decouples from the primordial plasma while still relativistic (see Fig. 1.5). The thermal relic mechanism provides an important framework for understanding of the origin and present DM density [9]. In the early universe, temperatures were sufficiently high to sustain frequent interactions between DM and other particle species. However, as the universe expanded and cooled, a critical point was reached where the interaction rate dropped below the expansion rate (Hubble parameter), causing DM to decouple from thermal equilibrium and "freeze out". After this point, the abundance of DM remains constant, a relic density that persists to the present day (represented by the dashed orange line in Fig. 1.5). To explore this mechanism in detail let us consider the Boltzmann equation derived in the previous subsection. If we take the z_f to be freeze out epoch:

$$Y(z) = Y(z_{eq}) \qquad \text{for} \qquad z < z_f \tag{1.32}$$

$$Y_{eq}(z) < Y(z) \approx Y_{eq}(z_f) \qquad \text{for} \qquad z > z_f \tag{1.33}$$

The behavior illustrated in Fig.1.5 demonstrates the Boltzmann-suppressed equilibrium distribution for DM particles in the early universe (solid blue line). If particles decoupled at epoch $z_f < 1$, which means that they were relativistic when decoupled from the plasma, they are called "hot" DM. These particles retain large velocity dispersion after decoupling, significantly impacting large-scale structure formation processes. This high velocity dispersion effectively erases small-scale perturbations and suppresses the formation of structure at early times. The present-day value for the co-moving number density Y can be calculated by recognizing that it equals the equilibrium value at freeze-out:

$$Y_0 = Y_{eq}(z_f) = \frac{\zeta(3)}{\pi^2} g_{eff} \left[\frac{2\pi^2}{45} g_{*s}(z_f)\right]^{-1} \tag{1.34}$$

From this, the present-day energy density of the DM particles is obtained as:

$$\rho_{0\chi} = m_\chi n_{0\chi} = m_\chi s_0 Y_0 \tag{1.35}$$

The Standard Model neutrino represents the canonical example of a particle with these characteristics, decoupling while still relativistic at $T \approx 1$ MeV. The density parameter for neutrinos can be calculated as follows:

$$Y_0 = Y_{eq}(z_f) = \frac{\zeta(3)}{\pi^2} g_{eff} \left[\frac{2\pi^2}{45} g_{*s}(z_f)\right]^{-1/3} \tag{1.36}$$

$$\rho_{0\nu} = m_\nu n_{0\nu} = m_\nu s_0 Y_0 \tag{1.37}$$

where Y_0 is the neutrino-to-photon ratio, g_{eff} and g_{*s} are effective degrees of freedom for energy density and entropy density, respectively. The density parameter for neutrinos, Ω_ν, can then be calculated as:

$$\Omega_\nu = \frac{\rho_{0\nu}}{\rho_c} = \frac{m_\nu s_0 Y_0}{3H_0^2} \tag{1.38}$$

where ρ_c is the critical density and H_0 is the Hubble constant. For a neutrino mass of $m_\nu \approx 0.05$ eV, we find $\Omega_\nu \approx 0.001$. While this value is small compared to the total matter density, it still contributes to the overall energy density of the universe.

Cold Dark Matter and WIMP paradigm

In contrast to hot DM, we now consider particles that decouple from the plasma when $z_f > 1$, which are classified as cold DM (CDM). This indicates that they have become non-relativistic before decoupling (See Fig. 1.5). These particles have low velocity dispersion and play a crucial role in initiating the structure formation process. In this section, we examine the theoretical framework of cold DM and the WIMP paradigm through the thermal relic mechanism. The Weakly Interacting Massive Particle (WIMP) is the prototypical candidate for cold DM. With their characteristic weak-scale interactions, WIMPs typically span a mass range of 1 GeV to 1 TeV. The thermal evolution of WIMPs follows a distinct pattern governed by the interplay between the interaction rates and the cosmic expansion. At high temperatures $T \gg m_\chi$, while WIMPs are in equilibrium with the cosmic plasma, their number density is given by:

$$n_\chi^{eq} \approx g_\chi \left(\frac{m_\chi T}{2\pi}\right)^{3/2} e^{-\frac{m_\chi}{T}} \tag{1.39}$$

As the universe cools, the rate of annihilation drops below the rate of Hubble expansion, leading to the decoupling from the plasma. Their abundance after that freezes out as represented in the Fig. 1.5, leaving the fraction of particles that we observe today. To estimate the relic density, we can use a similar approach to the above and work with Eq. (1.31). In the non-relativistic limit, for $z \gg 1$, the equilibrium abundance is exponentially suppressed, leaving the relic abundance as:

$$Y_0 \approx \frac{1}{\langle\sigma v\rangle m_\chi M_{Pl} \sqrt{g_*} z_f} \tag{1.40}$$

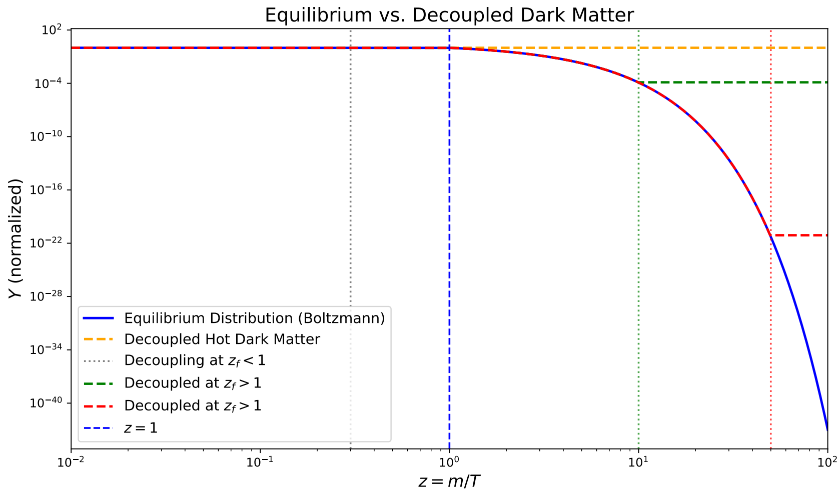

Figure 1.5: Boltzmann suppressed equilibrium distribution and decoupled particle behavior for $z_f \ll 1$ and $z_f \gg 1$.

where the $z_f = m\chi/T_f$ is our freeze-out parameter, typically assumed to be at the order of ten for WIMP-like particles. Then the present day density parameter for WIMPs can be found to be:

$$\Omega_\chi h^2 = \frac{m_\chi s_0 Y_0}{\rho_{crit}} \tag{1.41}$$

The Cross-Section Perspective

Examining Eq. (1.40) from another perspective reveals that the relic abundance is inversely proportional to the thermally averaged annihilation cross section. This relationship yields a remarkable coincidence known as the "WIMP miracle": a cross section value of $\langle \sigma v \rangle \approx 3 \cdot 10^{-26} \text{cm}^3/\text{s}$ naturally produces the observed DM density in the universe today. This relationship between cross-section and relic density follows a clear physical principle. When annihilation processes are more efficient (higher cross sections), DM particles continue to annihilate effectively for a longer period as the universe cools, resulting in a smaller final abundance. Conversely, with less efficient annihilation (lower cross sections), the freeze-out occurs earlier while more DM particles remain, leading to a higher relic density. This behavior establishes a direct connection between particle physics parameters and cosmological observations, creating a powerful framework for constraining DM models.

1.2.2 Non-Thermal Relics

Freeze-in: Feebly Interacting Massive Particles (FIMPs)

Another possible mechanism for the production of DM is the freeze-in mechanism. In contrast to freeze-out, this mechanism involves Feebly Interacting Massive Particles

(FIMPs), which are so weakly coupled to the thermal bath that they never achieve thermal equilibrium. The freeze-in mechanism builds up the abundance of these particles gradually as interactions with the thermal bath produce them over time. For example, consider the direct freeze-in process that involves two bath particles, B_1 and B_2, interacting through a coupling $\lambda B_1 B_2 \chi$, where χ represents the candidate DM. For $m_{B_1} > m_{B_2} + m_\chi$, the dominant production channel is the decay of the heavier bath particle:

$$B_1 \to B_2 + \chi. \tag{1.42}$$

The evolution of the number density of χ is governed by the Boltzmann equation [10]:

$$\begin{aligned}\dot{n}_\chi + 3Hn_\chi = \int d\Pi_\chi d\Pi_{B_1} d\Pi_{B_2} (2\pi)^4 \delta^4(p_\chi + p_{B_2} - p_{B_1}) \\ \times \Big[|M|^2_{B_1 \to B_2 + \chi} f_{B_1} (1 \pm f_{B_2})(1 \pm f_\chi) \\ - |M|^2_{B_2 + \chi \to B_1} f_{B_2} f_\chi (1 \pm f_{B_1}) \Big].\end{aligned} \tag{1.43}$$

Since FIMPs begin with negligible initial abundance, $f_\chi \approx 0$, and the production rate is dominated by the decay term. Assuming thermal equilibrium for the bath particles, $f_{B_1} \approx e^{-E_{B_1}/T}$, and negligible Pauli-blocking effects, the abundance can be expressed as:

$$Y_\chi \approx \frac{135 g_{B_1}}{8\pi^4 g_{*s}\sqrt{g_{*\rho}}} \frac{M_{\rm Pl}\Gamma_{B_1}}{m_{B_1}^2}, \tag{1.44}$$

where g_{B_1} is the internal degrees of freedom of B_1, Γ_{B_1} is its decay width, and $g_{*s}, g_{*\rho}$ are the effective degrees of freedom for entropy and energy densities [10].

A fundamental distinction between freeze-in and freeze-out mechanisms is their opposite response to interaction strength λ: DM abundance increases with coupling in freeze-in scenarios, while decreasing in freeze-out production. This relationship highlights the opposite trends in abundance generation: freeze-out relies on the eventual decoupling from equilibrium, while freeze-in builds up gradually as the universe cools. Experimental signals of freeze-in could include long-lived metastable particles, potentially detectable at the LHC or through cosmological observations.

Feebly Interacting Massive Particles (FIMPs) are characterized by several distinctive properties. They interact very weakly with Standard Model particles, resulting in significantly suppressed production rates. Their generation primarily occurs at late times in the universe's evolution when temperatures have decreased substantially. Compared to conventional thermal relics, FIMPs typically yield smaller relic abundances due to their limited interaction with the primordial plasma. Several theoretical particles serve as promising FIMP candidates. Sterile neutrinos represent one possibility—these heavy neutrinos interact exclusively through weak force and gravitational channels, and can be produced via mixing processes with active neutrinos. Dark photons constitute another candidate category, arising as hypothetical gauge bosons from a dark $U(1)$ gauge symmetry. These particles can undergo mixing with ordinary photons and can be generated during the early universe. Axion-like particles also belong to this category, characterized by their light mass and weak interactions. Various mechanisms can produce these particles, including the decay of more massive particles or through misalignment of a scalar field, similar to processes described for axion production.

1.2.3 Dark Matter Constraints

While a variety of theoretical models for DM have been presented, each is constrained by astrophysical observations, cosmological data, or laboratory experiments. These constraints not only narrow down the parameter space for viable dark matter candidates, but also provide crucial guidance for designing experiments and interpreting their results, creating a productive feedback loop between theory development and experimental testing. The thermal relic scenario, often invoked for WIMPs, im-

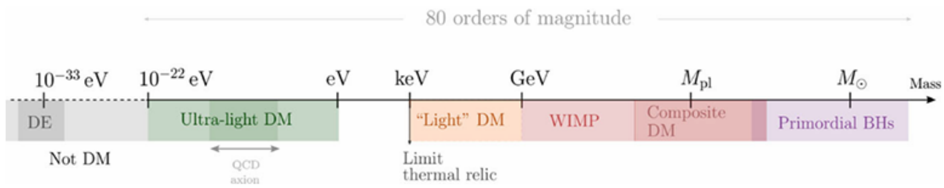

Figure 1.6: Broad mass range of DM candidates. Figure from [11]

poses a well-defined upper limit on the annihilation cross-section $\langle \sigma v \rangle$ due to the requirement of producing the correct DM abundance. Specifically, the value of the annihilation cross-section is constrained by the requirement to produce the observed relic abundance. Deviations from this value either overproduce or underproduce DM, providing a strong constraint on models with weakly interacting candidates.

Similarly, light DM particles such as sterile neutrinos are constrained by X-ray observations. Decays of such particles into photons are expected to produce characteristic spectral lines, which have yet to be unambiguously observed. These non-detections translate into stringent bounds on the mixing angle and mass of sterile neutrinos, pushing their parameter space into narrower regions. For ultra-light axion-like particles, astrophysical observations provide robust constraints. The suppression of structure formation due to the quantum pressure of ultra-light particles excludes masses below $\approx 10^{-22} eV$, as such candidates would erase small-scale structures, which are inconsistent with the observed distribution of galaxies. Similarly, searches for axion-photon conversion in strong magnetic fields, including the CAST experiment and various astrophysical observations, have explored couplings spanning several orders of magnitude, ruling out a large portion of the parameter space. Finally, gravitational lensing investigations, dynamical impacts on star populations, and the possibility of their contribution to cosmic gamma-ray backgrounds - all place restrictions on primordial black holes. The strongest constraints rule out PBHs in the mass range $10^{17}g \leq M_{PBH} \leq 10^{22}g$ as the primary contributors to DM density; however, heavier PBHs remain an intriguing option.

With these constraints narrowing the field of possibilities, experimental searches continue to play a pivotal role in guiding us toward a deeper understanding of DM's true nature.

1.3 Dark Matter Detection

In the previous sections, we discussed the observational evidence for the existence of DM and the theoretical particles proposed as DM candidates. Now we will focus on the main experimental approaches used for DM detection. A schematic representa-

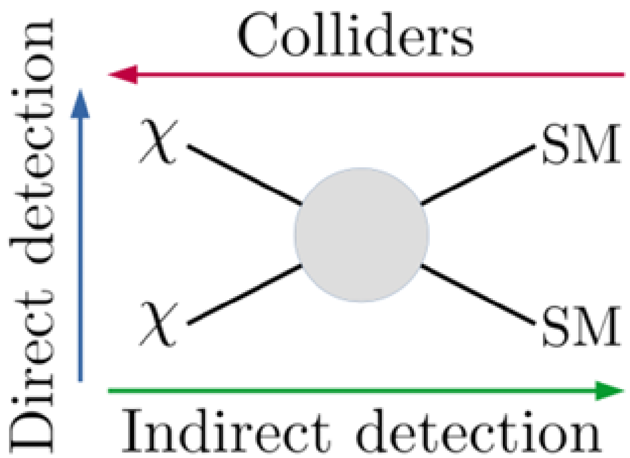

Figure 1.7: Main DM search strategies. Figure from [7]

tion of the major strategies and interplay between the three search types is shown in Fig. 1.7. These approaches—direct, indirect, and collider searches—complement each other in the hunt for DM. To date, no unambiguous detection of DM has been made, but these experiments have progressively narrowed down the viable parameter range. In the following sections, we outline theoretical considerations for each detection method.

1.3.1 Direct Detection

Direct detection experiments represent the most straightforward approach to DM searches. These experiments aim to observe interactions that occur when DM particles from the galactic halo pass through detector materials on Earth. These experiments directly probe the ambient DM that should be passing through our local environment, and offer several advantages: direct access to the DM population responsible for the galactic rotation curves, and controlled laboratory testing of multiple interaction types simultaneously. The fundamental observation in this type of detection is the event rate, which represents the number of scatterings per unit time per unit detector mass. In the following sections, we examine different direct detection strategies.

Nuclear scattering

After the elastic (or inelastic) scattering, the resulting momentum transfer gives rise to a nuclear recoil, potentially detectable signal. In such a process, the recoil energy transmitted to the nucleus is:

$$E_R = \frac{|\mathbf{q}|^2}{2m_N} = \frac{\mu^2 v^2}{m_N}(1 - cos\theta) \tag{1.45}$$

with the expected rate:

$$R \propto N \frac{\rho_\chi}{m_\chi} \langle \sigma_\chi N \rangle \tag{1.46}$$

where N is a number of target nuclei in detector, ρ_χ local WIMP density with m_χ being WIMP mass, and $\mu = m_\chi m_N/(m_\chi + m_N)$. Expected dominant interaction mechanism is the elastic scattering attributed to spin-independent interactions. The differential recoil energy spectrum of such interaction is:

$$\frac{dR}{dQ} = \frac{\sigma_\chi \rho_\chi}{\sqrt{\pi} m_\chi m_\mu^2} F^2(Q) T(Q) \tag{1.47}$$

where the $F(Q)$ is nuclear form factor and $T(Q)$ dimensionless integral over local DM velocity distribution. The cross section behavior depends on the nature of the interaction. For spin-independent scattering in DM-nucleus interactions, the cross section scales approximately as $\sigma_{SI} \propto A^2 \sigma_{\chi-p}$, where A is the atomic mass number. The A^2 dependence arises from coherent scattering where all nucleons contribute in phase, providing significant advantages for detectors using heavier elements. In contrast, for spin-dependent scattering, the cross section follows $\sigma_{SD} = (J+1)/J \cdot \sigma_\chi$, showing dependence on the total nuclear spin J rather than the total count. Currently, experiments like LUX-ZEPLIN, XENONnT, and PandaX-4T utilize xenon detectors to measure nuclear recoil events with remarkable sensitivity. These experiments have achieved constraints on the spin-independent cross-section down to approximately [12–14]:

$$\sigma_\chi \approx 2.1 \cdot 10^{-48} \mathrm{cm}^2 \text{ for } m_\chi \approx 36 \mathrm{GeV}/c^2 \tag{1.48}$$

For lighter DM candidates, electron scattering experiments such as SENSEI and DAMIC aim to detect sub-electron ionization signals caused by DM-electron interactions. These approaches extend the search for DM to lower mass ranges where nuclear recoil is kinematically suppressed.

1.3.2 Indirect Detection

Indirect detection of DM relies on observing the radiation resulting from the DM annihilation or decay. Moreover, the presence of DM in galaxies/stars might change their structure or evolution, leading to unexpected behavior. One such phenomenon stems from the freeze-out scenario: when the annihilation rate of DM particles becomes slower than the Hubble expansion rate, the particles decouple from thermal equilibrium. However, residual annihilations still occur after this freeze-out and can produce observable signals. If the products of annihilation interact electromagnetically, this can affect the Big Bang Nucleosynthesis and CMB. Indeed, if the DM particles annihilate into Standard Model particles (electrons, photons, or neutrinos), during the BBN it leads to an increase of the Hubble rate and additional electromagnetic energy into the thermal bath. If the freeze-out happened after neutrino decoupling, it can lead to decrease/increase of the neutrino-to-photon temperature ratio. Assuming that DM does not interact with the SM particles, we can still look for observables. DM decay into invisible (non-interacting with SM particles) particles can still affect structure formation, affecting the Lyman-α power spectra. We can also find an upper-limit for the DM self-interaction rate from the Bullet Cluster. In addition, since DM is more concentrated in galaxies, if residual interactions result in SM particles, these can be detected. The flux of neutral particles from either decay or annihilation can be expressed as:

$$\Phi(E, \phi) = \frac{\Gamma}{4\pi m_\chi^a} \frac{dN}{dE} \int \rho[r, (l, \phi)]^a dl \tag{1.49}$$

In this expression, Φ represents the flux of neutral particles originating from either decay or annihilation processes, with the exponent a taking values of 1 or 2. The interaction rate Γ equals $\langle \sigma v \rangle/2$ for annihilation processes and $1/\tau$ for DM decay, where τ is the DM lifetime. The energy spectrum of decay or annihilation products is denoted by $\frac{dN}{dE}$, which depends on the DM particle mass that determines the energy transferred to decay or annihilation products. The DM density profile is represented by ρ. Although this method offers certain advantages, there are significant drawbacks coming from background interference and large systematic errors. Several optimization approaches can improve detection sensitivity. One approach focuses on regions with enhanced annihilation or decay rates; while most DM models have annihilation rates determined by relic density, phenomena such as Sommerfeld-enhanced annihilation can significantly increase these rates. Another strategy involves isolating energy bands where the signal spectrum peaks relative to the background. Researchers also concentrate observations on high-density DM regions, as galactic halos can effectively amplify DM annihilation signals.

1.3.3 Accelerator-based Detection

Collider experiments play a crucial role in the DM search quest, providing an environment to potentially probe DM interactions with Standard Model particles. The forefront tool of this method, the Large Hadron Collider (LHC), explores a wide range of DM scenarios. Here we provide a brief overview of collider-based DM searches. Their main focus is on identifying events where DM particles are produced after high energy collisions. For WIMP particles, it is expected to observe DM particles interacting weakly, but leaving no direct signals (just as neutrinos invisibly pass through the detector). In fact, their presence can be inferred from the missing transverse momentum (E_T^{miss}), as can be seen in Fig. 1.8. These searches are guided by theoretical frameworks that predict specific DM production channels. For example,

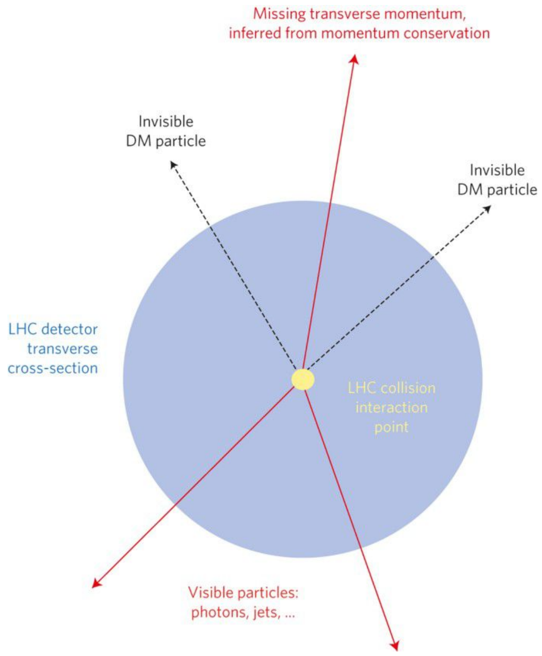

Figure 1.8: Schematic representation of the missing transverse momentum E_T^{miss} for DM production

the supersymmetry (SUSY) framework provides well-established candidates such as the neutralino. Effective field theories (EFTs), on the other hand, describe DM-SM interactions in terms of high-energy operators, providing model-independent interpretations of experimental results. The primary detection method uses "Mono-X" searches, where researchers look for events in which a visible particle recoils from unseen DM candidates. These searches target high-energy events with significant missing transverse momentum, using the visible particle as an "event tag". Mono-jet searches analyze events with high-momentum jets accompanied by significant E_{miss}^T. Mono-photon searches examine events where photons recoil from invisible particles. Similar approaches using Z or W bosons as tags provide additional sensitivity to different production mechanisms.

Chapter 2

Phase Transitions

Phase transitions in cosmology are fundamental to understanding the evolution of the universe. As the universe cooled, it underwent phase transitions, including the QCD phase transition at temperatures of about 100 MeV and the electroweak phase transition at about 100 GeV [9]. These transitions could provide explanations for crucial cosmic features, such as the observed matter-antimatter asymmetry [15], and may produce potentially detectable gravitational wave signals [16, 17]. This chapter provides a comprehensive overview of the theoretical framework required to understand phase transitions in the early universe, with a particular focus on first-order phase transitions. The first section introduces quantum field theory at finite temperature and develops the mathematical tools necessary to derive the effective potential that governs the phase transition dynamics. The characteristics of first-order phase transitions are then examined and distinguished from second-order transitions. The final section of this study analyzes how these transitions proceed through bubble nucleation and expansion, with particular attention to the bubble wall dynamics in the surrounding cosmic plasma.

2.1 Quantum Field Theory at Finite Temperature

To study phase transitions and symmetry recovery at high temperatures, standard quantum field theory (QFT) needs to be extended to include thermal effects. At zero temperature, the vacuum state contains only quantum fluctuations, while systems in thermal equilibrium must account for thermal fluctuations arising from the energy exchange with the thermal bath [18]. In this chapter, we study these phenomena for a real scalar field theory, since it provides the simplest framework for understanding thermal effects while still capturing the essential physics of the system. The mathematical methods used in this simplified approach can be generalized to more complex theories involving fermions and gauge fields, allowing a comprehensive understanding of thermal phenomena in QFT relevant to cosmological phase transitions.

2.1.1 Partition Function and Euclidean Action

At zero temperature, the partition function for a scalar field theory can be written as:

$$Z = \int [d\phi] e^{iS[\phi]} = \int [d\phi] e^{i\int d^4x \mathcal{L}}, \tag{2.1}$$

where $[d\phi] = \prod_x d\phi(x)$ represents functional integration over all field configurations. The Lagrangian density for a real scalar field is:

$$\mathcal{L} = \frac{1}{2}(\partial_\mu \phi)^2 - V(\phi). \tag{2.2}$$

The partition function contains all thermodynamic information about the system. Key thermodynamic quantities can be derived from it:

$$F = -T \ln Z \quad \text{(free energy)} \tag{2.3}$$

$$E = -\frac{\partial \ln Z}{\partial \beta} = \langle H \rangle \quad \text{(average energy)} \tag{2.4}$$

$$S = \frac{E - F}{T} = k_B \ln Z + \frac{\langle H \rangle}{T} \quad \text{(entropy)} \tag{2.5}$$

$$P = T \frac{\partial \ln Z}{\partial V} \quad \text{(pressure).} \tag{2.6}$$

We are particularly interested in the free energy density, which is minimized in equilibrium and can be interpreted in a constant background as the effective potential:

$$V_{\text{eff}} = \frac{F}{\mathcal{V}}, \tag{2.7}$$

where $\mathcal{V}$ is the volume of the system. This effective potential will be crucial for understanding the dynamics of phase transitions [19]. Two aspects of the partition function require careful consideration for cosmological applications. First, our use of the Euclidean space-time formulation, while mathematically convenient, means that we can no longer follow the real-time dynamics of the system. The imaginary time formalism is only strictly valid for systems in or very close to thermal equilibrium. After Wick rotation, the field equations transform from hyperbolic to elliptic differential equations, which changes their mathematical character. This transformation replaces wave-like propagation dynamics with diffusion-like behavior, limiting the formalism's ability to fully capture dynamical processes during first-order phase transitions. Although this approach proves inadequate for modeling non-equilibrium phenomena such as bubble nucleation and expansion, it remains sufficiently reliable for determining when transitions begin, as the system still maintains near-equilibrium conditions at the onset [20].

Second, the chemical potential μ appears in the partition function as the Lagrange multiplier conjugate to conserved particle number N. In the early universe, temperature effects dominated the energy scales ($\mu \ll T$), as evidenced by the observed tiny baryon asymmetry $n_B/n_\gamma \sim 10^{-10}$ [9]. Therefore, we can safely approximate $\mu = 0$

in our calculations, simplifying our analysis while maintaining physical accuracy. To implement the thermal formalism, we apply two key mathematical transformations: a Wick rotation to Euclidean time ($t \to -i\tau$) and compactification of the time direction ($0 \le \tau \le \beta$). The Euclidean formalism naturally connects quantum mechanics to statistical mechanics, where the partition function is given by the trace of the Boltzmann weight. The Wick rotation transforms the real-time action into the Euclidean action, where $L_E = -L(t \to -i\tau)$. Under this transformation, the path integral weight becomes:

$$Z_\beta = \int [d\phi] e^{-S_E[\phi]} = \int [d\phi] e^{-\int_0^\beta d\tau \int d^3x \mathcal{L}_E}, \tag{2.8}$$

with periodic boundary conditions for bosonic fields:

$$\phi(x, \tau = 0) = \phi(x, \tau = \beta). \tag{2.9}$$

These boundary conditions arise naturally from the trace operation in the partition function.

2.1.2 Effective Potential at Finite Temperature

To derive the effective potential, we split the field into classical and quantum parts:

$$\phi(x, \tau) = \phi_0 + \delta\phi(x, \tau), \tag{2.10}$$

where ϕ_0 is the constant classical background and $\delta\phi$ represents quantum/thermal fluctuations. Expanding the Euclidean action around this decomposition:

$$S_E[\phi] = S_E[\phi_0] + \frac{1}{2} \int_0^\beta d\tau \int d^3x\, \delta\phi(x, \tau)[-\partial^2 + V''(\phi_0)]\delta\phi(x, \tau) + \mathcal{O}(\delta\phi^3). \tag{2.11}$$

The boundary conditions (Eq. (2.9)) combined with the compactified time direction lead to discrete Matsubara frequencies in the imaginary time formalism. Due to the spin-statistics theorem, different fields exhibit distinct periodicity conditions:

$$\omega_n = \begin{cases} 2\pi n T & \text{for bosons (scalar fields and gauge bosons)} \\ (2n+1)\pi T & \text{for fermions (spin-1/2 fields),} \end{cases} \tag{2.12}$$

where n runs over all integers [21]. These frequencies emerge naturally when we decompose fields that satisfy the respective periodic or antiperiodic boundary conditions in imaginary time [19,20]. The quantum fluctuations can be expressed in terms of Matsubara frequencies as:

$$\delta\phi(x, \tau) = \sqrt{\frac{T}{\mathcal{V}}} \sum_{n=-\infty}^{\infty} \int \frac{d^3k}{(2\pi)^3} \delta\phi(k, \omega_n) e^{i(k\cdot x + \omega_n \tau)}, \tag{2.13}$$

where $\omega_n = 2\pi n T$ for bosons as defined above [21]. After integrating out the quantum fluctuations, the effective potential becomes:

$$\begin{aligned} V_{\text{eff}}(\phi_0, T) &= \frac{F}{\mathcal{V}} = -\frac{T}{\mathcal{V}} \ln Z \\ &= V(\phi_0) + \int \frac{d^3k}{(2\pi)^3} \left[\frac{E_k}{2} + T \ln(1 - e^{-E_k/T}) \right], \end{aligned} \tag{2.14}$$

where $E_k = \sqrt{k^2 + m^2(\phi_0)}$ and $m^2(\phi_0) = V''(\phi_0)$. The first term in the integral is the zero-temperature Coleman-Weinberg correction, which is UV divergent:

$$\begin{aligned} V_{1-loop}(\phi_0) &= \int \frac{d^3k}{(2\pi)^3} \frac{E_k}{2} \\ &= \frac{m^4(\phi_0)}{64\pi^2} \left[\frac{2}{\epsilon} + \ln\left(\frac{m^2(\phi_0)}{\mu^2} \right) - \frac{3}{2} \right] + \text{finite terms}, \end{aligned} \tag{2.15}$$

where ϵ appears in dimensional regularization ($d = 4 - \epsilon$) and μ is the renormalization scale. The divergent terms are absorbed into counterterms in the classical potential through renormalization, yielding finite corrections that depend logarithmically on the field-dependent mass:

$$V_{1-loop}^{ren}(\phi_0) = \frac{m^4(\phi_0)}{64\pi^2} \ln\left(\frac{m^2(\phi_0)}{\mu^2} \right) + \text{finite terms}. \tag{2.16}$$

The second term gives the finite temperature correction:

$$V_T(\phi_0) = T \int \frac{d^3k}{(2\pi)^3} \ln(1 - e^{-E_k/T}). \tag{2.17}$$

In the high-temperature limit ($T \gg m$), this can be expanded as:

$$V_T(\phi_0) = -\frac{\pi^2}{90} T^4 + \frac{m^2(\phi_0)}{24} T^2 - \frac{m^3(\phi_0)}{12\pi} T + \mathcal{O}(m^4 \ln(m/T)). \tag{2.18}$$

This high-temperature expansion reveals several important physical effects. The T^4 term represents the free energy of radiation, but does not affect phase transition dynamics because it is field independent. The T^2 term modifies the mass term and leads to symmetry restoration at high temperatures. In particular, the term proportional to T, which is cubic in mass, can induce first-order phase transitions by creating a barrier between phases. When the temperature becomes comparable to or smaller than the field-dependent mass, higher-order terms in the expansion become increasingly important, requiring us to use the full integral expression instead. The full effective potential can thus be written as a sum of classical, quantum, and thermal effects:

$$V_{\text{eff}}(\phi_0, T) = V(\phi_0) + V_{1-loop}^{ren}(\phi_0) + V_T(\phi_0). \tag{2.19}$$

The critical temperature T_c for symmetry restoration can be determined by solving:

$$\left. \frac{\partial^2 V_{\text{eff}}}{\partial \phi_0^2} \right|_{\phi_0 = 0} = 0. \tag{2.20}$$

In the next section, we apply these tools to analyze first-order phase transitions, including bubble nucleation and expansion, which are crucial for understanding phase transitions in the early universe.

2.2 First Order Phase Transitions

In thermodynamic systems, phase transitions can be characterized by the behavior of the free energy and its derivatives. A first-order phase transition (FOPT) is distinguished by discontinuities in the first derivatives of the free energy, indicating non-analytic behavior at the transition point. The average energy of a system can be expressed in terms of the free energy F and temperature T as:

$$E = F - T\frac{\partial F}{\partial T}. \tag{2.21}$$

From this equation, we can see that a discontinuity in $\frac{\partial F}{\partial T}$ leads to a corresponding discontinuity in the energy E. Such an abrupt change in energy during a transition characterizes first-order phase transitions and corresponds to the release or absorption of latent heat. This latent heat L, defined as the difference in energy between the two phases, can be written as:

$$L = E_2 - E_1 = \Delta E = T\Delta s, \tag{2.22}$$

where Δs represents the entropy difference between phases. This discontinuous change in both energy and entropy is a defining characteristic of first-order phase transitions.

The finite temperature QFT framework from the previous section provides a powerful tool for analyzing these transitions through the effective potential, which incorporates quantum and thermal fluctuations. To illustrate the physical nature of FOPT, we can examine the behavior of the Higgs field H as a concrete example, though the formalism applies to any scalar field theory. As shown in Fig. 2.1a, during a FOPT, the Higgs potential develops a barrier between degenerate minima at the critical temperature $T = T_c$ (red line). This barrier, which arises primarily from the cubic term $T|m|^3$ in the effective potential, creates a discontinuity that requires quantum tunneling for the transition to proceed. The evolution of the potential is demonstrated clearly as temperature decreases from high values ($T \gg T_c$, blue curve), where the Higgs field has zero vacuum expectation value, through the critical temperature, to zero temperature (black curve), where the Higgs acquires a non-zero expectation value.

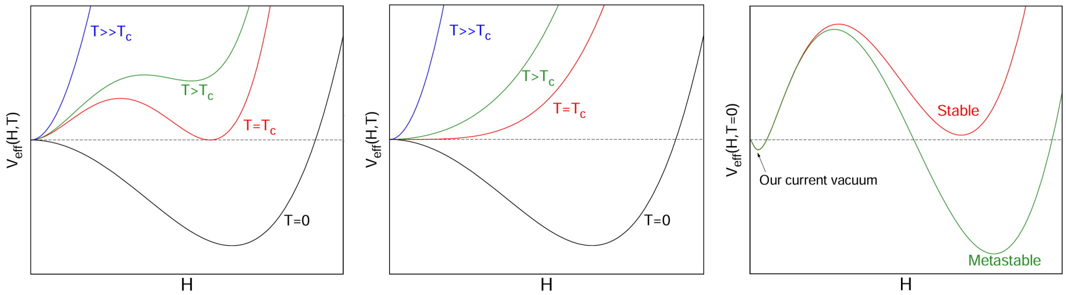

(a) First-order phase transition: The Higgs potential develops a barrier between degenerate minima at $T = T_c$ (red line). The evolution is shown from high temperature ($T \gg T_c$, blue) where the Higgs field has zero vacuum expectation value, through the critical temperature, to zero temperature (black) where the Higgs acquires a non-zero vacuum expectation value.

(b) Second-order phase transition: The potential evolves continuously from a single minimum at $H = 0$ to a broken phase minimum at $H \neq 0$, without developing a barrier at $T = T_c$.

(c) Vacuum stability at $T = 0$: Comparison between a stable potential (red) where our current vacuum is the global minimum, and a metastable potential (green) where a deeper minimum exists at large field values.

Figure 2.1: Evolution of the effective potential $V_{eff}(H,T)$ for the Higgs field H at different temperatures. Figure from [22].

This behavior contrasts sharply with second-order phase transitions (Fig. 2.1b), which proceed continuously without developing a barrier. In second-order transitions, the curvature at $H = 0$ changes sign smoothly at T_c, and the minimum shifts continuously to non-zero field values as temperature decreases, with no metastable state or tunneling involved. The stability of our vacuum state depends on the behavior of the potential at large field values, as illustrated in Fig. 2.1c. If a deeper minimum exists at large field values (green curve), our current vacuum is only metastable. A truly stable vacuum (red curve) requires that our current minimum represents the global minimum of the potential.

2.3 Bubble Nucleation

The cosmological phase transition proceeds from the high-temperature symmetric minimum, $\phi = 0$, to the low-temperature symmetry-breaking vacuum, $\phi = \sigma$. As in ordinary quantum mechanics, the decay of the false vacuum to the true vacuum occurs via quantum tunneling. However, in a QFT context, this tunneling is more subtle because the path-integral formulation is manifestly real, whereas the decay rate computation relies on imaginary (exponential) contributions. Two main approaches have been discussed in the literature:

- **The semi-classical method** developed by Coleman and Callan, which we will explore in this section [23, 24].

- **The direct method**, which provides a non-perturbative approach to computing the decay rate [25, 26].

The early universe is typically assumed to be nearly homogeneous, with the new phase emerging solely through thermal or quantum fluctuations. The transition proceeds via bubble nucleation: bubbles of the new ground state spontaneously form within the false vacuum. At temperatures below the critical temperature, a newly formed bubble will grow if its radius exceeds the critical radius (R_C), which is determined by the balance between volume and surface energy contributions. Again, we focus on the semi-classical approach, which has become the standard tool for calculating false vacuum decay rates. In this method, we begin by expanding the field around a classical solution $\bar{\phi}$, called the bounce:

$$\phi = \bar{\phi} + \delta\phi. \tag{2.23}$$

The bounce satisfies the classical equation of motion:

$$\partial_r^2 \bar{\phi} + \frac{d-1}{r}\partial_r \bar{\phi} = \frac{dV}{d\bar{\phi}}, \tag{2.24}$$

where d is number of dimensions ($d = 4$ for zero temperature, $d = 3$ for finite temperature). The bounce must satisfy the boundary conditions

$$\bar{\phi}(r \to \infty) = \phi_{\text{false}}, \quad \partial_r \bar{\phi}\big|_{r=0} = 0. \tag{2.25}$$

where the first condition ensures that we start in the false vacuum far from the bubble center, while the second condition ensures smoothness of the solution at the origin. The decay rate can then be written in terms of the partition function:

$$\Gamma = -2\,\mathrm{Im}(F) \;=\; 2\,T\,\mathrm{Im}\big[\ln Z\big]. \tag{2.26}$$

This expression follows from quantum mechanics, where a metastable state evolving in time has a complex energy, and the imaginary part determines the decay rate. For a state $|\phi(t)\rangle = e^{-iEt}|\phi(0)\rangle$ with $E = \mathrm{Re}(E) + i\,\mathrm{Im}(E)$, the probability decays as

$$\langle \phi(t) \mid \phi(t)\rangle = e^{2\,\mathrm{Im}(E)\,t}\,\langle \phi(0) \mid \phi(0)\rangle, \tag{2.27}$$

giving $\Gamma = -2\,\mathrm{Im}(E)$. At finite temperature, this generalizes to $\Gamma = -2\,\mathrm{Im}(F)$. Applying the saddle-point approximation around the bounce solution $\bar{\phi}$, we can express the decay rate as:

$$\Gamma \;\sim\; \frac{T}{Z_0}\,\mathrm{Im}\!\left[\big(\det S_E''[\bar{\phi}]\big)^{-\frac{1}{2}} e^{-S_E[\bar{\phi}]}\right], \tag{2.28}$$

where Z_0 is the partition function dominated by the false vacuum solution ϕ_{FV}, ($S_E''[\bar{\phi}]$) represents the second functional derivative of the Euclidean action (accounting for quantum fluctuations around the bounce), and $S_E[\bar{\phi}]$ is the Euclidean action evaluated on the bounce configuration — a field configuration interpolating between ϕ_{FV} and ϕ_{TV}. The bounce has one negative eigenvalue in its fluctuation spectrum, making the Gaussian integral around this solution divergent for real integration contours. This necessitates Coleman's complex contour-deformation approach. The negative mode appears because the bounce is not a minimum, but rather a saddle point of the Euclidean action — it represents the most probable "escape path" from the false vacuum. At finite temperature, the O(4) symmetry of the zero-temperature case is reduced to O(3) due to the compactification of Euclidean time. Consequently, the decay rate per unit volume (or tunneling rate per unit volume) is

$$\frac{\Gamma}{\mathcal{V}} = A(T)\, e^{-S_3/T}, \tag{2.29}$$

where S_3 is the three-dimensional Euclidean action:

$$S_3 = \int d^3x \left[\frac{1}{2}(\nabla\phi)^2 + V(\phi, T)\right], \tag{2.30}$$

and $A(T)$ contains both the determinant factors from quantum fluctuations and thermal corrections. For a phase transition to occur fully, the bubbles must expand and coalesce after nucleation. This requires a nucleation rate sufficient to produce at least one bubble per Hubble time, a condition that can be expressed as:

$$\Gamma/\mathcal{V} \sim H^4, \tag{2.31}$$

where $\mathcal{V} \sim H^{-3}$ represents the Hubble volume. The temperature at which this condition is satisfied defines the nucleation temperature T_N, which is typically lower than the critical temperature T_c. For strong phase transitions with large barriers, T_N can be significantly smaller than T_c; if the barrier is extremely large, the universe may remain trapped in the false vacuum (on timescales of the age of the universe) and the phase transition never takes place. Conversely, transitions with shallow barriers will have $T_N \approx T_c$. In general, there is no general analytical solution to Eq. (2.24), which describes the equation of motion for the bounce field configuration during bubble nucleation. This differential equation is challenging to solve exactly for arbitrary potentials. However, in the phenomenology of cosmological phase transitions, the energy difference between the two vacua, $\epsilon = V(\phi_{FV}) - V(\phi_{TV})$, can often be treated as small compared to the height of the potential barrier, ($\epsilon \ll V_{\text{barrier}}$). This condition allows us to employ the thin-wall approximation, which provides analytical insight into the bubble profile and nucleation rate. This condition is naturally satisfied near the critical temperature, where the two minima are nearly degenerate. In this limit, we can analytically understand key features of the first-order phase transition, including the bubble profile and the nucleation rate. In the thin-wall limit, we can evaluate the Euclidean action explicitly for each region. To do so, we model the bubble as having radius R, with the following three distinct regions:

- Inside the bubble ($r < R$): the field is in the true vacuum ϕ_{TV};
- The bubble wall ($r = R$): the field rapidly transitions between vacua;

- Outside the bubble ($r > R$): the field remains in the false vacuum ϕ_{FV}.

For the outside region ($r > R$), the field stays at ϕ_{FV} where $V(\phi_{FV}) = 0$ (by our normalization choice), giving:

$$S_3^{\text{outside}} = 0. \tag{2.32}$$

For the inside region ($r < R$), the field sits at ϕ_{TV} where $V(\phi_{TV}) = -\epsilon$:

$$S_3^{\text{inside}} = \int_0^R 4\pi r^2 dr\, V(\phi_{TV}) = -\frac{4\pi}{3} R^3 \epsilon. \tag{2.33}$$

For the wall region ($r \approx R$), we can neglect the friction term since R is large, and the action becomes:

$$S_3^{\text{wall}} = 4\pi R^2 \int dr \left[\frac{1}{2}(\partial_r \phi)^2 + V(\phi)\right] \equiv 4\pi R^2 S_1, \tag{2.34}$$

where in the second line we used energy conservation in the wall region, and S_1 is defined as the surface tension. The total action is thus:

$$S_3 = 4\pi R^2 S_1 - \frac{4\pi}{3} R^3 \epsilon, \tag{2.35}$$

which represents the competition between surface tension and volume energy. The critical radius R_c is found by minimizing the action with respect to R, as this gives the most probable bubble configuration for tunneling:

$$\left.\frac{\partial S_3}{\partial R}\right|_{R=R_c} = 8\pi R_c S_1 - 4\pi R_c^2 \epsilon = 0 \;\Rightarrow R_c = \frac{2S_1}{\epsilon}. \tag{2.36}$$

This critical radius represents the size at which surface tension and volume energy balance. Bubbles smaller than R_c collapse due to surface tension, while larger bubbles expand as the volume term dominates. Substituting this critical radius back into the action gives:

$$S_3(R_c) = \frac{16\pi S_1^3}{3\epsilon^2}. \tag{2.37}$$

This expression determines the tunneling rate $\Gamma/\mathcal{V} \sim e^{-S_3/T}$ in the thin-wall approximation. Using this result, we can rewrite the nucleation condition given in Eq. (2.31) as:

$$A(T) e^{-S_3/T} \sim H^4, \tag{2.38}$$

where by using the expression $H^2 \sim T^4/M_P^2$ during the radiation domination, we can recast the equation to get nucleation temperature T_N. For electroweak-scale transitions, a typical value is:

$$\frac{S_3}{T_N} \sim \ln\left(\frac{M_P^4}{T_N^4}\right) \approx 140, \tag{2.39}$$

where we assumed $T_N \sim 100$ Gev and $M_P \sim 10^{19}$ GeV. Once bubbles nucleate according to the conditions derived above, the subsequent dynamics of their expansion plays a crucial role in the completion of the phase transition, which will be examined in the following section.

2.4 Bubble Expansion

Following successful nucleation, as described previously, true vacuum bubbles must expand and convert the surrounding space to complete the phase transition. This expansion process is governed by the interplay of several competing forces acting on the bubble wall: an inward surface tension proportional to $\frac{S_1}{R}$, where S_1 is the surface tension and R is the bubble radius; and friction resulting from interactions with the surrounding plasma as the wall propagates through the medium. The condition for expansion is given by $V(\phi_{TV}) < V(\phi_{FV})$, where the interior pressure must be larger than the exterior pressure. The pressure can be written as $p = \frac{\pi^2}{90} g_{\text{eff}} T^4 - V_T(\phi)$. This condition can only be satisfied for $T < T_c$, when the true vacuum becomes energetically favorable (see Fig. 2.1a). The dynamics of an expanding bubble wall during FOPT are governed by the field equation which describes the evolution of the field in the potential and its coupling to the surrounding plasma [27]:

$$\Box\phi + \frac{\partial V(\phi)}{\partial \phi} = \eta \frac{\partial \phi}{\partial t}, \tag{2.40}$$

where the first term describes how the field propagates in time and space (capturing inertial effects), the second term represents the potential gradient acting as a driving force, and the third term represents friction with the plasma. For a plasma in thermal equilibrium, the friction coefficient η is given by:

$$\eta(\phi) = \sum_i g_i \int \frac{d^3k}{(2\pi)^3} \frac{\partial m_i^2(\phi)}{\partial \phi^2} \frac{f_i(1 \pm f_i)}{4E_i^2}, \tag{2.41}$$

where g_i is the number of internal degrees of freedom for species i, $m_i(\phi)$ is the field-dependent mass, f_i is the thermal distribution function, E_i is the particle energy, and the $\pm$ sign corresponds to bosons $(+)$ and fermions $(-)$. This friction arises from particles in the plasma interacting with the bubble wall and having their masses changed as they pass through it. According to Eq. (2.40), in the initial phase where the bubble nucleates, the potential gradient dominates the friction, leading to wall acceleration. During the expansion phase, the friction term becomes significant. Depending on the competition between the potential gradient and friction, the wall either reaches a terminal velocity or enters a runaway regime where it continues to accelerate. Next, to simplify and solve the field equation, we make several assumptions about bubble dynamics. First, we treat bubbles as macroscopic objects, allowing us to approximate the bubble wall as planar. We also assume that the wall speed is constant in the rest frame of the universe and that the system is in a steady state. Given the planar symmetry, we further simplify by choosing coordinates in which the wall moves along the z-direction, so that the field profile depends only on z, i.e., $\phi = \phi(z)$. Under these assumptions, we can rewrite Eq. (2.40) as:

$$\partial_z^2 \phi \; - \; V_T'(\phi) \; = \; -\, \eta_T(\phi)\, \gamma_w\, v_w\, \partial_z \phi, \tag{2.42}$$

where γ_w represents the Lorentz factor associated with the wall velocity v_w. Multiplying both sides by $\partial_z\phi$ and integrating over z:

$$\int dz \left[\frac{1}{2}\partial_z(\partial_z\phi)^2 - \frac{dV_T}{dz}\right] = -\int dz\eta_T(\phi)\gamma_w v_w(\partial_z\phi)^2, \tag{2.43}$$

we find that the Eq. (2.42) takes the form:

$$\Delta V_T \simeq \gamma_w v_w \int dz\eta_T(\phi)(\partial_z\phi)^2, \tag{2.44}$$

where $\Delta V_T = V_T(z=+\infty) - V_T(z=-\infty)$ is the potential difference across the wall. This equation relates the pressure difference driving the expansion to friction effects. Solving Eq. (2.44) yields the bubble wall speed v_w, although finding the exact solution is typically challenging. Qualitatively, the bubble wall dynamics can be classified into different modes based on the wall velocity and plasma behavior. We can characterize these modes by comparing the wall velocity with the speed of sound in the plasma $c_s = \frac{1}{\sqrt{3}}$. In deflagration, where $v_w < c_s$, the wall moves at subsonic speed, heating and pushing the plasma ahead of it, which leads to the formation of a shock wave in front of the wall. For detonations, characterized by $v_w > c_s$, the wall propagates supersonically, leaving the plasma in front unperturbed while heating occurs behind the wall. An intermediate case exists in hybrid or supersonic deflagration, where the wall velocity falls between the sound speed and the Chapman-Jouguet velocity ($c_s < v_w < v_J$), resulting in both shock wave formation and plasma heating. This completes the physical picture of bubble expansion in first-order phase transitions.

Chapter 3

Axions

Building on our discussion of phase transitions, we now focus on the axion, a compelling DM candidate that elegantly emerges from one of the most important puzzles in particle physics. The phase transitions framework sets the conditions under which specific particles that could account for DM can be produced. The axion, a pseudo-Nambu-Goldstone boson arising from the spontaneous breaking of a global symmetry, represents an intersection of particle physics and cosmology, simultaneously presenting a solution to the strong CP problem and fulfilling the constraints for DM outlined in Chapter 1.

3.1 The Strong CP-Problem

The axion emerges as a solution to what is known as the strong CP problem, a fundamental theoretical inconsistency within QCD. This problem arises from the term in the QCD Lagrangian:

$$\Delta\mathcal{L} = \frac{\alpha_s}{8\pi}\theta_0 G^a_{\mu\nu}\tilde{G}^{\mu\nu a}, \tag{3.1}$$

where $\alpha_s = g_s^2/(4\pi)$ is the gauge coupling of $SU(3)_c$, $G^a_{\mu\nu}$ is the gluon field strength tensor, $\tilde{G}^{\mu\nu a} = \frac{1}{2}\epsilon^{\mu\nu\rho\lambda}G^a_{\lambda\rho}$ is its dual, and θ_0 is a dimensionless parameter. Although this term preserves the gauge symmetries of the Standard Model, it violates both parity (P) and charge-parity (CP) symmetry. Its origin can be traced to the *"θ-vacua"* of QCD, which reflect the nontrivial topology structure of the QCD vacuum. Including this term is essential for a complete description of theory, as ignoring it would fail to account for important quantum effects, particularly tunneling between different vacuum states. The θ-term in the Lagrangian is influenced not only by the topology of the QCD vacuum but also by quantum effects from the quark sector. These effects emerge through the **chiral anomaly**, which contributes an additional term of the same form as (3.1), with a coefficient related to the phase of the quark mass matrix, $\hat{M}_q$. The quark mass term in the Lagrangian is expressed as:

$$\mathcal{L}_m = \bar{q}_L\hat{M}_q q_R, \tag{3.2}$$

where $\bar{q}_L$ and q_R are the left- and right-handed quark fields. A chiral rotation of these quark fields, necessary to produce physical quark masses, induces an additional phase term in the Lagrangian:

$$\Delta\mathcal{L}_m = \frac{\alpha_s}{8\pi}\mathrm{Arg}(\mathrm{Det}\hat{M}_q)G^a_{\mu\nu}\tilde{G}^{\mu\nu a}. \tag{3.3}$$

This contribution effectively shifts the CP-violating parameter to:

$$\theta_{\text{eff}} = \theta_0 + \mathrm{Arg}(\mathrm{Det}\hat{M}_q), \tag{3.4}$$

highlighting how CP violation in the strong sector depends on both the fundamental structure of the QCD vacuum and the properties of the quark mass matrix. The presence of a non-zero θ_{eff} term in the Lagrangian would lead to observable CP violation, with most notable being an **electric dipole moment (EDM)** for the neutron. The neutron EDM is estimated as:

$$d_n \approx 3.6 \cdot 10^{-16}\theta \cdot \mathrm{e\,cm}, \tag{3.5}$$

where e is the electron charge. However, experimental measurements have placed stringent constraints on neutron EDM, with current limits of $|d_n| < 2.9 \cdot 10^{-26} e\,\mathrm{cm}$ [28]. These measurements require θ_{eff} to be extraordinarily small ($\theta_{\text{eff}} \lesssim 10^{-10}$), giving rise to what is known as the strong CP problem: why is this parameter, which could naturally be of order unity, constrained to be so vanishingly small? This fine-tuning problem demands a theoretical explanation, and the axion naturally addresses this issue through a dynamical mechanism that we explore in the following section.

3.1.1 Peccei-Quinn Model

Within the SM, there is no natural mechanism to ensure $\theta_{\text{eff}} = 0$, leaving the strong CP problem unresolved. To address this, Peccei and Quinn proposed an ingenious **dynamical mechanism** that automatically drives θ_{QCD} to zero through non-perturbative effects. Their solution introduces a new global symmetry, now known as the Peccei-Quinn (PQ) symmetry, which acts on quarks according to the transformation:

$$q_{L_n} \to e^{ie^n_{PQ}\beta/2}q_{L_n} \quad \text{and} \quad q_{R_n} \to e^{-ie^n_{PQ}\beta/2}q_{R_n}, \tag{3.6}$$

where e^n_{PQ} represents the axion charge (or PQ charge) of the nth quark. Assuming that the charges of the six quarks sum up to unity, $\sum_n e_n^{PQ} = 1$, this symmetry transformation modifies the determinant of the quark mass matrix according to arg det$(M) \to$ arg det$M + \beta$. In the SM, however, this symmetry is explicitly broken by the Yukawa couplings given by:

$$\mathcal{L}_Y = Y^d\bar{Q}_L\phi d_R + Y^u\bar{Q}_L\tilde{\phi}u_R, \tag{3.7}$$

where $Y^{u,d}$ represent the Yukawa coupling matrices for the down- and up-type quarks, respectively; Q_L denotes the left-handed quark doublet containing u_L and d_L; d_R

and u_R are the right-handed down- and up-type quarks, which are singlets under $SU(2)_L$; ϕ is the Higgs doublet field with components ϕ^+ and ϕ^0; and $\tilde{\phi}$ represents the conjugate Higgs field, defined as $\tilde{\phi} = i\sigma_2\phi^*$.

To preserve the PQ symmetry, Peccei and Quinn introduced a second Higgs doublet, modifying the Higgs sector such that $\phi \to (H_1, H_2)$, where H_1 and H_2 transform as $H_1 \to e^{i\beta/6}H_1$ and $H_2 \to e^{-i\beta/6}H_2$. This structure allows each Higgs doublet to couple exclusively to either up-type or down-type quarks, ensuring that the PQ symmetry remains preserved in the Yukawa sector. The modified Yukawa Lagrangian becomes:

$$\mathcal{L}_Y = y^d \bar{Q}_L H_1 d_R + y^u \bar{Q}_L \tilde{H}_2 u_R, \tag{3.8}$$

where H_1 couples to the down-type quarks and H_2 couples to the up-type quarks, maintaining invariance under PQ transformations. The spontaneous breaking of the PQ symmetry is achieved through the introduction of a scalar field Φ that carries PQ charge. The potential for this field takes the form:

$$V(\Phi) = \lambda_\Phi \left(|\Phi|^2 - \frac{f_a^2}{2} \right)^2, \tag{3.9}$$

where λ_Φ represents a self-coupling constant, and f_a denotes the PQ symmetry-breaking scale. This potential attains its minimum at $|\Phi| = f_a/\sqrt{2}$, indicating the spontaneous breaking of the PQ symmetry. When the PQ symmetry undergoes spontaneous breaking, the Higgs doublets acquire non-zero vacuum expectation values (VEVs):

$$\langle H_1 \rangle = \frac{1}{\sqrt{2}} \begin{pmatrix} 0 \\ v_1 \end{pmatrix}, \quad \langle H_2 \rangle = \frac{1}{\sqrt{2}} \begin{pmatrix} 0 \\ v_2 \end{pmatrix}, \tag{3.10}$$

where v_1 and v_2 are the VEVs of H_1 and H_2, respectively, with $v_1^2 + v_2^2 = v^2 \approx (246\,\mathrm{GeV})^2$. When these Higgs doublets acquire non-zero vacuum expectation values, they spontaneously break the PQ symmetry at low energies. This symmetry breaking generates a massless Nambu-Goldstone boson — the axion — associated with the angular degree of freedom in the broken $U(1)_{\mathrm{PQ}}$ symmetry. However, the axion differs from typical Nambu-Goldstone bosons because it acquires a small mass through non-perturbative QCD effects. These instanton effects explicitly violate the PQ symmetry, transforming the axion into a pseudo-Nambu-Goldstone boson. These anomalies generate a small potential for the axion via QCD instantons, giving it a mass:

$$m_a \sim \frac{\Lambda_{\mathrm{QCD}}^2}{f_a}, \tag{3.11}$$

where f_a represents the PQ symmetry-breaking scale, and Λ_{QCD} denotes the QCD scale. This mechanism transforms the axion into a pseudo-Nambu-Goldstone boson, making it a viable solution to the strong CP problem and compelling DM candidate. Despite the elegance of the PQ mechanism in resolving the strong CP problem, the original model faces significant experimental challenges. In its simplest formulation, the axion was expected to have relatively strong interactions with the SM particles, making it detectable in both astrophysical and laboratory experiments. However, extensive searches have yielded no evidence for such an axion, and much of the parameter space predicted by the original model has been experimentally excluded. Astrophysical constraints, in particular, have provided stringent limits on the axion's coupling to photons, electrons, and nucleons. For example, the duration of the neutrino burst from supernova SN1987A constrains the axion-nucleon coupling, as efficient axion emission would have shortened the observed burst duration [29]. Similarly, white dwarf cooling rates place limits on the axion-electron coupling, as axion emission could accelerate their cooling [30]. These experimental null results have effectively ruled out the original PQ axion, necessitating the development of alternative models that preserve the dynamical solution to the strong CP problem while remaining consistent with observational constraints.

3.1.2 Alternative Models: KSVZ and DFSZ

To address the observational limitations and construct a viable axion model, several extensions of the original PQ model were proposed. Two major ones are KSVZ (Kim-Shifman-Vainshtein-Zakharov) and DFSZ (Dine-Fischler-Srednicki-Zhitnitsky) models. These models introduce modifications that decouple the axion's properties from experimental constraints, opening up viable parameter spaces.

KSVZ Model: The KSVZ model introduces new heavy quarks Q that carry a PQ charge but are singlets under electroweak interactions. The Lagrangian includes terms:

$$\begin{aligned}\mathcal{L}_{\text{KSVZ}} = \bar{Q}_L i\not{D} Q_L + \bar{Q}_R i\not{D} Q_R + (y_Q \Phi \bar{Q}_L Q_R + \text{h.c.}) \\ + |\partial_\mu \Phi|^2 - V(\Phi),\end{aligned} \tag{3.12}$$

where Φ is the PQ scalar field that transforms as $\Phi \to e^{i\alpha}\Phi$ under the PQ symmetry, and $Q_{L,R}$ transform as:

$$\begin{aligned}Q_L \to e^{-i\alpha/2} Q_L, \\ Q_R \to e^{i\alpha/2} Q_R.\end{aligned} \tag{3.13}$$

The potential $V(\Phi)$ takes the Mexican hat form:

$$V(\Phi) = \lambda_\Phi (|\Phi|^2 - \frac{f_a^2}{2})^2, \tag{3.14}$$

leading to spontaneous symmetry-breaking when Φ acquires a vacuum expectation value $\langle \Phi \rangle = f_a/\sqrt{2}$. The heavy quarks obtain masses $m_Q = y_Q f_a/\sqrt{2}$ through their Yukawa coupling to Φ. The axion field $a(x)$ emerges as the phase of Φ:

$$\Phi(x) = \frac{f_a + \rho(x)}{\sqrt{2}} e^{ia(x)/f_a}, \tag{3.15}$$

where $\rho(x)$ is the massive radial mode. The axion couples to gluons through the heavy quark loop, generating the effective interaction:

$$\mathcal{L}_{a\text{-gluon}} = \frac{\alpha_s}{8\pi}\frac{a}{f_a}G^a_{\mu\nu}\tilde{G}^{\mu\nu a}, \tag{3.16}$$

which provides the mechanism for solving the strong CP problem.

DFSZ Model: The DFSZ model extends the Higgs sector with two Higgs doublets H_1, H_2 and a complex scalar Φ. The Yukawa interactions in the DFSZ model take the form:

$$\mathcal{L}_Y = y_d\bar{Q}_L H_1 d_R + y_u\bar{Q}_L H_2 u_R + y_e\bar{L}H_1 e_R + \text{h.c.}, \tag{3.17}$$

allowing the axion to couple to SM fermions through their Higgs interactions. Both models predict an axion mass related to the decay constant f_a through QCD effects:

$$m_a \approx 5.7\,\mu\text{eV}\left(\frac{10^{12}\,\text{GeV}}{f_a}\right). \tag{3.18}$$

The coupling to photons, which is crucial for experimental searches, differs between the models:

$$g_{a\gamma\gamma} = \frac{\alpha}{2\pi f_a}C_{a\gamma\gamma}, \tag{3.19}$$

where $C_{a\gamma\gamma}$ is a model-dependent coefficient [31] [32]:

$$C_{a\gamma\gamma} = \begin{cases} -1.92 & \text{(KSVZ)} \\ 0.75 & \text{(DFSZ)} \end{cases} \tag{3.20}$$

For both models, the axion decay constant f_a must be large ($f_a \gg 10^8$ GeV) to satisfy astrophysical constraints, making the axion very light and weakly coupled. This parameter space, known as the "invisible axion" window, remains viable and is the focus of current experimental searches. The specific phenomenology and detection prospects depend on the model-dependent couplings and will be discussed in detail in subsequent sections.

3.2 Axion and SM Particles Interactions

Since the axion emerges as a pseudo-Nambu-Goldstone boson from the spontaneous breaking of a global PQ symmetry, its interactions are inherently suppressed and take specific forms dictated by the underlying symmetry. These interactions are essential for understanding the production mechanism in the early universe and are also used in experimental detection strategies. The fundamental interactions of the axion with Standard Model particles can be described by the Goldberger-Treiman relation [33], which provides the general framework for the coupling of the pseudo-Nambu-Goldstone boson to conserved currents. This relation takes the form:

$$\mathcal{L}_a = \frac{1}{f_a}\partial_\mu a J^\mu_{PQ}, \tag{3.21}$$

where $\mathcal{L}_a$ represents the axion interaction term, $\partial_\mu a$ is the derivative of the axion field, and J^μ_{PQ} denotes the PQ current. The scale f_a is the PQ symmetry-breaking scale, which we introduced in the previous section and which governs the overall strength of axion interactions. The derivative coupling in this expression is characteristic of Nambu-Goldstone bosons, reflecting the fact that these particles couple weakly at low energies. The PQ current itself is constructed from the fermionic fields that carry PQ charge:

$$J^\mu_{PQ} = \sum_f e_f^{PQ} \cdot \bar{f}\gamma^\mu\gamma^5 f, \tag{3.22}$$

where the sum runs over all fermion species f (quarks and leptons), e_a^f represents the PQ charge of each fermion species as defined in Section 3.1.1, $\bar{f}$ denotes the Dirac adjoint of the fermion field, and $\gamma^\mu\gamma^5$ represents the axial current operator. This expression demonstrates that axions couple to the axial-vector currents of fermions, with the strength of each coupling determined by the fermion's PQ charge. Using the expression for the PQ current in the axion Lagrangian and partially integrating yields:

$$\mathcal{L}_a = \frac{a}{f_a}\sum_f e_a^f \partial_\mu(\bar{f}\gamma^\mu\gamma_5 f) = \frac{a}{f_a}\sum_f \frac{e_f^a}{2} \cdot \bar{f}\gamma^\mu\gamma^5 f. \tag{3.23}$$

The factor of 1/2 arises from the partial intergration and symmetrization of the derivative coupling. The Eq. (3.23) explicitly shows how the axion field couples to the axial currents of different fermion species with strengths proportional to their PQ charges. Beyond axion-fermion interactions, the axion also couples to gauge fields through anomalous interactions. These couplings arise because the PQ symmetry-breaking scale enters through quantum corrections, connecting the axion to the topological structure of non-Abelian gauge theories. The interaction with gluons, which is fundamental to the resolution of the strong CP problem discussed in Section 3.1, takes the form:

$$\mathcal{L}_{ga} = \frac{\alpha_s a}{8\pi f_a} \cdot G^a_{\mu\nu}\tilde{G}^{\mu\nu a}, \tag{3.24}$$

where $\alpha_s = g_s^2/(4\pi)$ is the strong coupling constant, $G^a_{\mu\nu}$ is the gluon field strength tensor, and $\tilde{G}^{\mu\nu a} = \frac{1}{2}\epsilon^{\mu\nu\rho\lambda}G^a_{\rho\lambda}$ denotes its dual. Levi-Civita tensor $\epsilon^{\mu\nu\rho\lambda}$ ensures that this interaction respects the pseudo-scalar nature of the axion field. Similarly, the axion couples to photons through the electromagnetic anomaly:

$$\mathcal{L}_{\gamma a} = C_\gamma \frac{\alpha a}{8\pi f_a} \cdot F_{\mu\nu}\tilde{F}^{\mu\nu}, \tag{3.25}$$

where C_γ is a dimensionless, model-dependent constant (such as -1.92 for KSVZ models or 0.75 for DFSZ models), $\alpha = e^2/(4\pi)$ represents the electromagnetic fine structure constant, $F_{\mu\nu}$ is the electromagnetic field strength tensor, and $\tilde{F}^{\mu\nu} = \frac{1}{2}\epsilon^{\mu\nu\rho\lambda}F_{\rho\lambda}$ is its dual. This photon coupling (extremely weak due to the large value of f_{a}) provides a basis for many experimental searches for axions. The gluon interaction plays a dual role in axion physics. First, it generates the small mass of the axion through QCD effects (as described in Section 3.1). Second, in the early universe, when QCD undergoes its own phase transition at temperatures around $\Lambda_{\rm QCD} \approx$ 200 MeV, this coupling drives the axion field toward CP conserving minimum of its potential, thereby dynamically solving the strong CP problem.

3.3 Axion Production

Several mechanisms can produce axions in the early universe, each resulting in different abundance and momentum distribution characteristics. These production channels determine whether axions can account for all or part of the observed DM. In this section we review the main production mechanisms: thermal production, the misalignment mechanism, and generation from topological defects. These mechanisms operate under different cosmological conditions and predict different constraints on the axion parameters.

3.3.1 Thermal Axions

Thermal axions follow the standard relic scenario from Section 1.2.1. The axion number density evolves according to the Boltzmann equation through interactions with QCD plasma. Main production channels include:

- Quark-gluon scattering: $q + g \to q + a$
- Quark-quark scattering: $q + q \to g + a$
- Gluon fusion: $g + g \to g + a$.

For relativistic axions in thermal equilibrium, the number density follows the Fermi-Dirac or Bose-Einstein distribution appropriate for fermions or bosons. Since axions are bosons, their equilibrium density is given by:

$$n_a^{eq} = \frac{\zeta(3)}{\pi^2} T^3 \tag{3.26}$$

where $\zeta(3)$ is the Riemann zeta function. The rate of thermal axion production through these QCD processes can be estimated from dimensional analysis. The thermally averaged cross-section scales approximately as:

$$\langle \sigma v \rangle \approx \frac{\alpha_s^3}{32\pi^2 f_a^2}. \tag{3.27}$$

The resulting relic density from thermal production can be formulated using the freeze-out formalism. For typical values of f_a required to satisfy astrophysical constraints $f_a > 10^8$ GeV, the thermal contribution to the axion abundance is:

$$\Omega_a h^2 \approx 10^{-6} \left(\frac{f_a}{10^{12}\ \text{GeV}} \right)^2 \left(\frac{T_d}{10^8\ \text{GeV}} \right)^3, \tag{3.28}$$

where T_d represents the decoupling temperature. This estimate reveals that thermal production alone is not sufficient to account for observed DM abundance, motivating the consideration of non-thermal mechanisms.

3.3.2 The Misalignment Mechanism

The misalignment mechanism represents a fundamentally different approach to axion production, operating through non-thermal dynamics of the axion field itself. This mechanism relies on the dynamics of the axion field in the early universe, where the axion potential arises due to QCD instantons at temperatures below $T_{\rm QCD}$. At high temperatures ($T \gg \Lambda_{\rm QCD}$), the axion field is effectively massless, and the potential for the field vanishes. In this regime, the axion field $\bar{\theta} = \theta + \frac{a}{f_a}$ can take any initial value within $\bar{\theta}_i \in [0, 2\pi)$, with no reason to assume $\bar{\theta}_i = 0$. As the universe cools and the QCD potential forms, the axion field acquires a mass and begins to oscillate coherently around the minimum of its potential at $\bar{\theta} = 0$ (See Fig. 3.1). These oscillations result in a relic population of axions, which behave as CDM. The physics underlying this mechanism is elegantly simple yet profound. As the universe cools and the QCD scale is reached, instantons generate a potential for the axion field:

$$V(a) \sim \Lambda_{\rm QCD}^4 \left(1 - \cos\left(\frac{a}{f_a}\right)\right), \tag{3.29}$$

and the axion mass dynamically emerges:

$$m_a^2 = \left.\frac{\partial^2 V(a)}{\partial a^2}\right|_{a=0} \sim \frac{\Lambda_{\rm QCD}^4}{f_a^2}. \tag{3.30}$$

As this potential develops, the axion field begins to roll toward the minimum and oscillating, These oscillations behave like classical field with the energy density $\rho_a \propto a^{-3}$, characteristic of CDM. Fig. 3.1 illustrates this evolution, showing how the initially static field begins oscillating as the potential forms. To fully describe

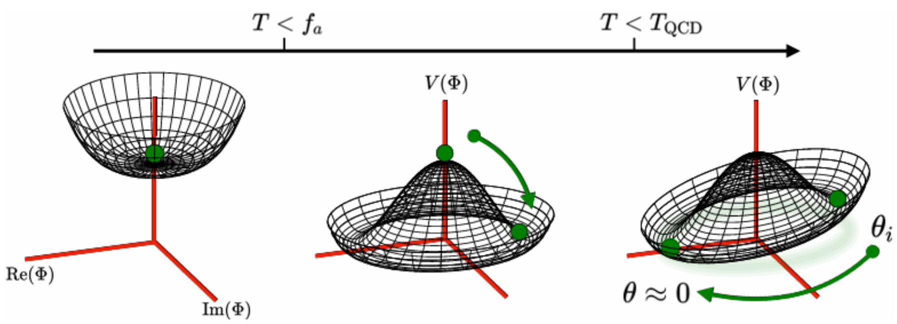

Figure 3.1: Evolution of the axion field $\bar{\theta}$ as the universe cools, showing the onset of oscillations as the potential forms. Figure from [31]

the axion dynamics, we consider the equation of motion in an expanding universe:

$$\ddot{a} + 3H\dot{a} + \frac{\partial V(a)}{\partial a} = 0, \tag{3.31}$$

where H is the Hubble parameter. Expressing the field in terms of the angle $a = f_a\theta$, this becomes:

$$\ddot{\theta} + 3H\dot{\theta} + m_a^2(T)\sin(\theta) = 0, \tag{3.32}$$

where $m_a(T)$ is a function of temperature as:

$$m_a(T) = \begin{cases} 0 & \text{at } T \gg \Lambda_{QCD} \\ m_0 \left(\frac{\Lambda_{QCD}}{T}\right)^n & \text{at } T > \Lambda_{QCD}. \end{cases} \tag{3.33}$$

The Eq.(3.32) is very similar to the scalar field evolution but there is $\sin\theta$ term which makes it unique. Although for initial value of $\theta_i \ll 1$ the difference is not important, for some $\theta_i \approx \pi$ this affects the dynamics and adds corrections. Another distinction is the mass term which is temperature function now. While the full temperature-dependence of the axion can be computed in more details (See Ref. [34], [35]), we focus on simple treatment and approximate it as given in (3.33). From the scalar field evolution in the expanding universe we can expect that the axion field does not evolve during $m_a(T) \ll H(T)$ and starts to oscillate only at $m_a \approx H(T)$ [9]. The oscillation temperature $T_{\rm osc}$ can be estimated by equating these quantities. Then the energy density of the axion field can be expressed in terms average initial misalignment angle:

$$\rho_a(T_{osc}) \approx m_a^2(T_{osc}) f_a^2 \bar{\theta}_i^2. \tag{3.34}$$

From this, number density then can be estimated as:

$$n_a(T_{osc}) \approx \frac{\rho_a(T_{osc})}{m_a(T_{osc})} \approx m_a(T_{osc}) f_a^2 \bar{\theta}_i^2 = H_a(T_{osc}) f_a^2 \bar{\theta}_i^2, \tag{3.35}$$

where we have used the relation $m_a(T_{osc}) \approx H_a(T_{osc})$. Following standard cosmological evolution, the comoving number density remains constant, allowing us to track the abundance to the present epoch:

$$\frac{n_a}{s} = \frac{H(T_{osc}) f_a^2 \bar{\theta}_i^2}{\frac{2\pi^2}{45} g_* T_{osc}^3}. \tag{3.36}$$

The present day mass density of axions is then:

$$\rho_0 = \frac{n_a}{s} m_a s_0 \approx \frac{m_a f_a^2 s_0 \bar{\theta}_i^2}{\sqrt{g_*} T_{osc} M_{Pl}}, \tag{3.37}$$

where we can already obtain preliminary estimate by setting the $T_{osc} \approx 1$ GeV:

$$\Omega_a = \rho_0/\rho_c = \left(\frac{10^{-6}\text{eV}}{m_a}\right) \bar{\theta}_i^2. \tag{3.38}$$

We can obtain a good DM candidate for $\bar{\theta}_i \approx O(1)$, with an axion mass around $10^{-5} - 10^{-7}$ eV, resulting in cold DM where the effective pressure of the oscillating field is zero. One can prove that our estimations are quite reasonable by utilizing the explicit expression for Eq. (3.33) and result in:

$$\Omega_a \approx 0.2 \left(\frac{10^{-6}\text{ eV}}{m_a}\right)^{1.2} \frac{\bar{\theta}_i}{2h^2}, \tag{3.39}$$

where the inverse proportional relationship to the axion mass might seem counter-intuitive: as the axion mass becomes heavier, the relic density decreases. However, this is fully justified, as the temperature at the onset of oscillations, T_{osc}, determines the initial number density. Heavier axions begin oscillating earlier, at higher T_{osc}, resulting in a larger initial number density. As a result, this population gets more diluted as the universe expands. In contrast, lighter axions start oscillating later, at lower T_{osc}, and experience less dilution due to shorter time between their onset of oscillations and the present day.

We now need to account for the initial angle $\bar{\theta}_i$ to obtain a better estimate for the axion mass. Considering that the angle squared can take any value between 0 and π^2, the average value of a random distribution of $\bar{\theta}_i^2$ is given by:

$$\langle\bar{\theta}_i^2\rangle = \frac{1}{\pi}\int_0^\pi \theta^2\, d\theta = \frac{\pi^2}{3}. \tag{3.40}$$

However, this result can be further corrected by considering the non-linear terms in the axion potential. Since the potential is not quadratic but instead follows a cosine form (See Eq.(3.29)) the dynamics of the axion field deviate from the simple harmonic oscillator approximation. Taking these effects into account, the effective average value of the squared initial angle is modified to [36]:

$$\langle\bar{\theta}_i^2\rangle \approx 4.5. \tag{3.41}$$

Our estimates hold for the case where the PQ symmetry was broken after inflation (see Fig. 3.2). If the PQ symmetry is broken during the inflationary stage, then the value of the initial angle will be constant across the visible universe. The inflationary stage takes an initially small causally connected region and inflates it to a region larger than the present horizon as shown in Fig. 3.2. In this case we get more simplified picture of the misalignment mechanism, with a single term - initial angle. By examining equation (3.39) and requiring $\Omega_{DM}h^2 = 0.12$ to match observations, we can identify which combinations of axion mass and initial angle θ_i lead to overproduction or underproduction of DM (See Fig. 3.3). In order to obtain small axion mass, we can fine-tune the θ_i to avoid overproduction. Meanwhile the massive axions cannot produce required abundance of the DM. We have another constraint, maximum allowed Hubble scale, to fit the isocurvature to the Planck bound. Since inflation also enhances the vacuum fluctuations of light scalar fields, including the axion field, those fluctuations result in isocurvature perturbations with an amplitude:

$$\frac{\delta\theta}{\theta_i} \approx \frac{H_I}{2\pi f_a}, \tag{3.42}$$

where H_I is the Hubble parameter during inflation. These isocurvature perturbations are constrained by cosmic microwave background (CMB) observations, leading to an upper bound on the inflation scale:

$$H_I \lesssim 10^7\ \text{GeV}\left(\frac{f_a}{10^{11}\ \text{GeV}}\right). \tag{3.43}$$

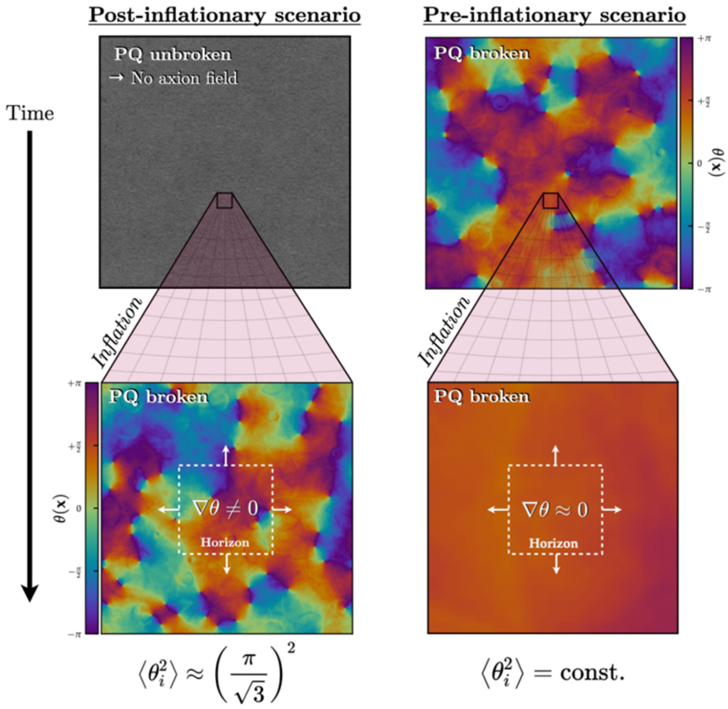

Figure 3.2: Schematic illustration of the two possible scenarios for PQ symmetry-breaking relative to inflation. *Left*: PQ symmetry breaks after inflation, leading to different θ_i values in different patches of the universe and a predictive axion mass around 10^{-5} eV. *Right*: PQ symmetry breaks before or during inflation, resulting in a uniform θ_i across the observable universe and allowing for a wider range of viable axion masses. Figure from [32]

By fine-tuning the θ_i to achieve the observed DM density (3.39) with larger values of f_a, corresponding to lower axion masses, we obtain:

$$m_a \approx 10^{-6}\ \text{eV} \left(\frac{\theta_i}{\pi}\right)^2 . \tag{3.44}$$

3.3.3 Axion Production from Topological Defects

In addition to the thermal and misalignment mechanisms, axions can be produced through the decay of topological defects formed during phase transitions in the early universe. When the universe undergoes global symmetry breaking, such as the spontaneous breaking of the PQ symmetry, topological defects inevitably form through the Kibble mechanism. The Kibble mechanism explains how causally disconnected regions of the universe independently choose their vacuum state during rapid symmetry breaking. When these regions come into causal contact, incompatibilities between their vacuum choices necessitate the formation of topological defects. These defects can be classified by their dimensionality: domain walls (2D), cosmic strings (1D), and monopoles (0D). For the global $U(1)_{\text{PQ}}$ symmetry breaking that gives rise to

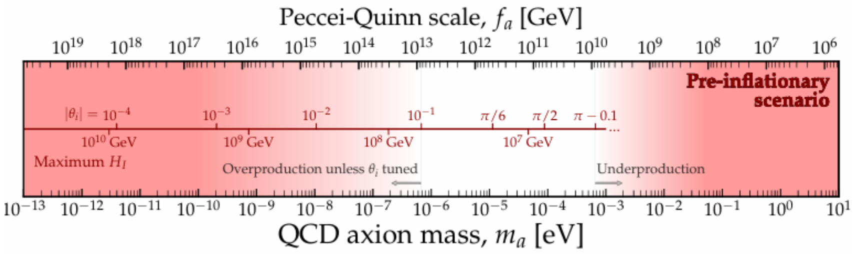

Figure 3.3: Pre-inflationary scenario constraints on the QCD axion mass. The red line in the middle of the figure represents the θ_i value to meet the observed DM abundance. Figure from [31]

axions, the relevant defects are cosmic strings (at temperature $T \lesssim f_a$) and domain walls (at temperature $T \lesssim \Lambda_{\text{QCD}}$), each contributing to the axion abundance though distinct mechanisms.

Cosmic Strings

Cosmic strings form when the temperature drops below the PQ symmetry breaking scale. These string-like topological defects form due to the "winding" of the axion field when neighboring regions choose different values of θ. Although the Goldstone nature of θ works to homogenize its value within each horizon volume, different horizon patches can have different values. The energy density stored in these cosmic strings is characterized by their tension (energy per unit length):

$$\mu_{string} \approx \pi\sigma^2 \ln\left(\frac{t}{\delta_s\sqrt{\xi}}\right), \tag{3.45}$$

where $\delta_s \approx (\sqrt{\lambda}\sigma)^{-1}$ represents the string core width, and ξ is a dimensionless parameter that quantifies the network density. Numerical simulations demonstrate that string networks evolve toward a scaling regime where the energy density maintains a constant ratio to the horizon scale [37–39]:

$$\rho_{string}(t) = \frac{\xi\mu_{string}}{t^2}, \tag{3.46}$$

This scaling behavior requires continuous emission of axions to maintain equilibrium, as the network continually loses energy through radiation. The change in axion abundance per entropy density, per Hubble time, required for this scaling behavior is [40]:

$$\Delta(n_a/s) \sim \frac{\mu_{string}t^2}{\omega T^3}\Delta(Ht), \tag{3.47}$$

where ω is the average energy of the radiated axion. This production mechanism shares conceptual similarities with the energy dissipation from moving bubble walls during the bubble expansion phase described in Section 2.4, particularly in how the energy from a field configuration is converted into particle radiation. However, unlike the bubble wall case where radiation occurs during collision events, the axion radiation from strings is a continuous process that occurs throughout the evolution of the string network.

Domain Walls

Domain walls form at the QCD phase transition temperature when axions acquire mass. The structure and stability of these walls depend on the domain wall number N_{DW} [41], which represents the discrete symmetry of the axion potential:

$$N_{DW} \equiv \frac{(\text{periodicity of } a)}{2\pi f_a}. \tag{3.48}$$

For a single complex scalar field $\Phi \propto \exp(ia/\sigma)$, the field a has a periodicity $2\pi\sigma$, which leads to the following relation:

$$N_{DW} = \frac{\sigma}{f_a}. \tag{3.49}$$

The width of domain walls is estimated as $\delta_w \approx m_a^{-1}$ and the surface mass density of domain walls is given by:

$$\sigma_{wall} \approx 9.23 m_a f_a^2, \tag{3.50}$$

where the coefficient 9.23 includes the contribution from the structure of the neutral pion field [42, 43].

Classification and Evolution

The fate of the string-wall systems is different depending on whether $N_{DW} = 1$ or $N_{DW} > 1$, leading to distinct evolution scenarios analogous to the different bubble expansion modes discussed in Section 2.4

Short-lived Domain Walls ($N_{DW} = 1$) For models with $N_{DW} = 1$, one domain wall is attached to each string. Such string-wall systems are unstable and decay due to the tension of walls soon after formation [44]. The energy of domain walls per horizon volume is estimated as $\sim \sigma_{wall} t_1^2$, and their energy density is given by:

$$\rho_{wall}(t_1) = \frac{A\sigma_{wall}}{t_1}, \tag{3.51}$$

where A is a numerical coefficient known as the area parameter, which can be estimated from numerical simulations [42, 45]. The number density of axions produced by the decay of these short-lived string-wall systems is:

$$n_{a,dec}(t) = \frac{\rho_{string-wall}(t_d)}{\bar{\omega}_a} \left(\frac{a(t_d)}{a(t)} \right)^3, \tag{3.52}$$

where $\bar{\omega}_a$ is the mean energy of axions produced by this decay process, and t_d is the decay time of the system.

Long-lived Domain Walls ($N_{DW} > 1$) For models with $N_{DW} > 1$, more than two domain walls are attached to a single string. Such string-wall networks are stable and long-lived since the strings are sustained by tension of the walls from multiple directions, creating a more complex network than the simple bubble coalescence scenarios examined in Chapter 2. After the time t_2 (defined by equating the tension of strings and walls), we can ignore the effect of strings on the dynamics of the string-wall systems, and the energy density is dominated by domain walls:

$$\rho_{wall}(t) = \frac{A\sigma_{wall}}{t}. \tag{3.53}$$

Since this energy density decreases more slowly than matter ($\propto a^{-3}$) or radiation ($\propto a^{-4}$), domain walls would eventually overclose the universe [46]. However, this problem can be avoided by introducing a "bias" term in the potential:

$$V_{bias}(\Phi) = -\Xi\sigma^3(\Phi e^{-i\delta} + h.c.), \tag{3.54}$$

where Ξ and δ are dimensionless parameters. If Ξ takes a small but nonvanishing value, the N_{DW} degenerate vacua are lifted, causing the lowest energy vacuum to dominate and the walls to annihilate.

Contribution to Dark Matter Abundance

The total axion relic abundance includes contributions from these topological defects, adding to the misalignment mechanism discussed in Section 3.3.2. For models with $N_{DW} = 1$, the contribution from string-wall systems is given by [47]:

$$\begin{aligned}\Omega_{a,dec}h^2 =& 7.88 \times 10^{-3} \times \frac{A+\xi}{\sqrt{1+\epsilon_w^2}} \left(\frac{\beta_2}{62}\right)^{2/(4+n)} \left(\frac{g_{*,2}}{75}\right)^{-(2+n)/2(4+n)} \\ & \left(\frac{f_a}{10^{10}\ \mathrm{GeV}}\right)^{(6+n)/(4+n)} \left(\frac{\Lambda_{QCD}}{400\ \mathrm{MeV}}\right), \end{aligned} \tag{3.55}$$

where ϵ_w parameterizes the average momentum of axions at the time of the decay of string-wall systems. For models with $N_{DW} > 1$, assuming exact scaling, the contribution is [47]:

$$\Omega_{a,dec}h^2 = 0.756 \times \sqrt{\frac{C_d}{1+\epsilon_a^2}} \left(\frac{A^3 N_{DW}^4}{(1-\cos(2\pi/N_{DW}))}\right)^{1/2} \tag{3.56}$$

$$\left(\frac{\Xi}{10^{-52}}\right)^{-1/2} \left(\frac{f_a}{10^{10}\ \mathrm{GeV}}\right)^{-1/2} \left(\frac{\Lambda_{QCD}}{400\ \mathrm{MeV}}\right)^3, \tag{3.57}$$

where C_d is a numerical coefficient related to the decay time of domain walls, and ϵ_a characterizes the mean momentum of radiated axions. Recent numerical simulations [42,45,47,48] have significantly improved our understanding of these processes. Studies with large grid sizes (up to 32768^2 in 2D and 512^3 in 3D) have allowed more precise determinations of parameters such as A, ϵ_w, ϵ_a, and C_d. These simulations reveal that the contribution from topological defects can be larger than that from the misalignment mechanism, making the constraints on axion model parameters more strict. The increased precision in these calculations has led to updated estimates of the axion mass required for the observed DM abundance. For models with $N_{DW} = 1$, axions can account for the observed DM density with a mass range of $m_a \approx (0.9 - 1.4) \times 10^{-4}$ eV [47]. For models with $N_{DW} > 1$, a wider mass range of $m_a \approx \mathcal{O}(10^{-4} - 10^{-2})$ eV is possible with a mild tuning of parameters [47].

In both scenarios, the axion production from topological defects provides a significant contribution to the cold DM of the universe, rivaling or exceeding the contribution from the misalignment mechanism discussed in Section 3.3.2. The evolution and decay of these topological defects represent an interplay between quantum field theory, phase transitions, and early universe cosmology that complements our understanding of the dynamics discussed in previous chapter.

3.4 Constraints and Searches

Having discussed various production mechanisms that could produce the observed axion abundance, we now turn to the experimental search strategies designed to detect these elusive particles. As mentioned in Section 3.1.1, the original PQ model predicted relatively strong axion interactions that have been experimentally ruled out, necessitating the development of alternative models such as KSVZ and DFSZ. The search for axions has therefore focused on exploring extremely weak interactions, characterized by very large decay constants f_a, typically $f_a \geq 10^8$ GeV. This section examines the main experimental constraints on the axion parameters, drawing on astrophysical observations, laboratory experiments, and cosmological data.

3.4.1 Stellar Evolution

Astrophysical environments provide some of the strongest constraints on axion properties, since the presence of axions with detectable couplings would significantly alter the energy balance and evolution of stars. These constraints derive primarily from energy loss arguments, where axion emission would provide an additional channel for energy transport, modifying observable stellar properties.

Primakoff Process $(\gamma + Ze \to Ze + a)$ converts photons into axions in the presence of charged particles (e.g., in the dense plasma of stars). The rate of axion production through this process is proportional to $g^2_{a\gamma\gamma}$. For the Sun, the axion luminosity from the Primakoff process is given by [49]:

$$L_a \approx 1.85 \cdot 10^{-3} \left(\frac{g_{a\gamma\gamma}}{10^{-10}\,\mathrm{GeV}^{-1}} \right)^2 \cdot L_\odot, \tag{3.58}$$

where $L_\odot = 3.85 \times 10^{33}$ erg/s represents the Sun's photon luminosity. If this axion emission was too efficient, it would accelerate the solar cooling beyond what is observationally allowed, given the Sun's well-established age and helioscopically measured properties. Helioscope experiments, such as CAST (CERN Axion Solar Telescope), directly search for solar axions by attempting to convert them back to photons in laboratory magnetic fields. These experiments have established some of the strongest model-independent bounds on the axion-photon coupling: [50]:

$$g_{a\gamma\gamma} < 1.16 \cdot 10^{-10}\,\mathrm{GeV}^{-1}, \quad \text{for } m_a \lesssim 0.02\,\mathrm{eV}. \tag{3.59}$$

Electron-Axion Bremsstrahlung In stellar environments, axions can also be produced via electron-nucleus bremsstrahlung ($e + Ze \to Ze + e + a$). This process depends on the axion-electron coupling g_{ae}, which affects the evolution of stars in the Red Giant Branch (RGB) and White Dwarf stages. Observations of the tip of the RGB in globular clusters constrain the axion-electron coupling $g_{ae} < 1.6 \cdot 10^{-13}$ [51].

Supernova Axions Core-collapse supernovae, such as SN1987A, provide additional constraints. In the dense core of a supernova, axions can be produced via nucleon-nucleon bremsstrahlung ($N + N \to N + N + a$). If axions escape too efficiently, they would reduce the energy available for neutrino emission, shortening the observed neutrino burst duration. The observed duration of the neutrino burst from SN1987A constrains the axion decay constant $f_a \gtrsim 10^8\,\mathrm{GeV}$ [52]. This limit corresponds to a lower bound on f_a and ensures that $m_a \lesssim 10^{-2}\,\mathrm{eV}$.

3.4.2 Light-Shining-Through-Walls

LSW experiments like ALPS search for photon-axion-photon conversion by shining laser beam at wall and apply a strong magnetic field to convert photons into axions and back to photons on the other side. The conversion probability of photon into axions is:

$$P(\gamma \to a) = 4\frac{g_{a\gamma}^2 B^2 \omega^2}{m_a^2} \sin^2\left(\frac{m_a^2 L}{4\omega}\right), \tag{3.60}$$

where ω represents the photon energy, B magnetic field and L is its length. The constraints from LSW are around $g_{\phi\gamma} \leq 7 \cdot 10^{-8}$ GeV^{-1} for $m_a \leq 10^{-3}$eV. Fig. 3.4 summarizes the constraints on the axion parameter space in terms of the axion mass m_a and f_a. The shaded regions represent excluded parameter space based on various experiments and astrophysical observations.

3.5 Isocurvature Perturbations

The study of primordial fluctuations in the CMB provides one of the most powerful constraints on axion dark matter models. While standard inflationary scenarios predict adiabatic perturbations—where all energy density components fluctuate together—certain axion models can generate isocurvature perturbations, which represent relative fluctuations between different energy components without changing the total energy density. Understanding these perturbations is essential for connecting axion models to cosmological observations. Isocurvature perturbations arise naturally in axion models where the Peccei-Quinn symmetry breaks before or during inflation. In such scenarios, the axion field acquires quantum fluctuations during

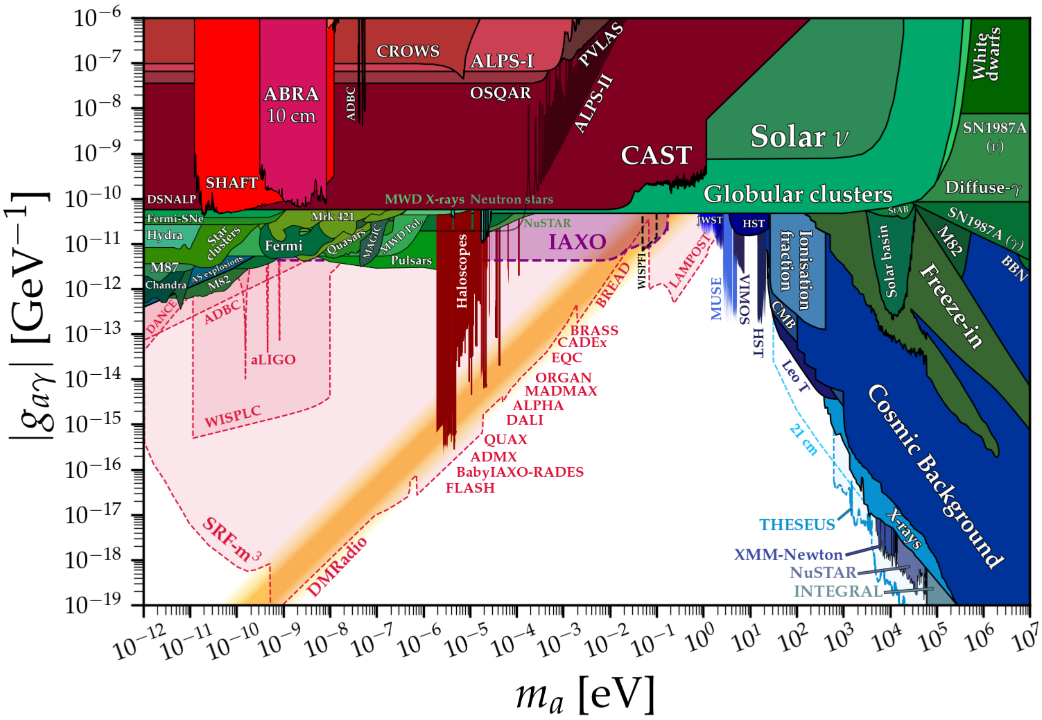

Figure 3.4: Current experimental constraints (shaded regions) and future sensitivities (lines) for the axion-photon coupling $g_{a\gamma\gamma}$ versus axion mass m_a. The yellow band represents the predictions for the QCD axion models KSVZ and DFSZ. The various colored regions show excluded parameter space from different experiments and astrophysical observations: stellar evolution constraints including the horizontal branch stars (HB), helioscopes like CAST, haloscopes like ADMX, and other laboratory experiments. Future projections include proposed experiments like IAXO and ALPSII. Figure from [53].

inflation, leading to spatial variations in the initial misalignment angle $\bar{\theta}_i$ across the observable universe. These variations translate directly into density perturbations in the axion dark matter component, while leaving the radiation and baryon densities relatively unperturbed. To understand how these perturbations emerge, consider an axion field with value of θ at different locations during inflation. The quantum fluctuations of this field during inflation can be characterized by their spectrum:

$$\Delta^2\theta = \left(\frac{H_\mathrm{I}}{2\pi f_a}\right)^2, \tag{3.61}$$

where H_I is the Hubble parameter during inflation, and the fluctuations arise from de Sitter vacuum fluctuations inherent to inflationary spacetime. These fluctuations persist after inflation ends and imprint themselves on the axion abundance through the misalignment mechanism discussed in Section 3.3.2. The power spectrum of axion isocurvature fluctuations scales as:

$$P_{\rm iso} \propto \left(\frac{H_{\rm I}}{2\pi f_a}\right)^2. \tag{3.62}$$

This expression reveals the fundamental tension in pre-inflationary PQ breaking scenarios: large values of $H_{\rm I}$ enhance isocurvature modes, while large values of f_a suppress them. The amplitude of isocurvature perturbations relative to curvature perturbations is given by:

$$\alpha_{\rm iso} = \frac{P_{\rm iso}}{P_{\rm adiabatic}} \approx \frac{(H_{\rm I} f_a \theta_i)^2}{M_{\rm Pl} V_{\rm Inf}^{1/2}}, \tag{3.63}$$

where $V_{\rm Inf}$ represents the inflationary potential and $M_{\rm Pl}$ is reduced Planck mass. Current CMB observational measured bound requires [54]:

$$\alpha_{\rm iso} \leq 0.038 \qquad \text{(at 95\% confidence level)} \tag{3.64}$$

which can be directly translated to:

$$H_I \lesssim 10^7\,{\rm GeV}\left(\frac{f_a}{10^{11}\,{\rm GeV}}\right). \tag{3.65}$$

This relationship imposes severe upper bounds on the axion decay constant [31, 32]. The impact of isocurvature also depends on the timing of PQ symmetry-breaking relative to inflation. If PQ symmetry breaks before inflation, the axion field becomes homogenized across the observable universe, and isocurvature modes arise solely from inflationary quantum fluctuations. In this scenario, constraints on H_I become critical, and fine-tuning of the initial misalignment angle $\bar{\theta}_i$ is required to match the observed DM abundance while avoiding excessive isocurvature modes. Alternatively, if PQ symmetry breaks after inflation, the axion field varies randomly in causally disconnected regions, leading to suppressed isocurvature effects and different dynamics governed by the decay of topological defects such as cosmic strings and domain walls.

These constraint axions with higher decay constants and restrict the inflationary energy scale. Future CMB experiments and large-scale structure surveys, such as CMB-S4, have the potential to further tighten these bounds and probe subdominant isocurvature modes, providing deeper insights into axion cosmology and the nature of inflation.

Chapter 4

Bubble Misalignment Mechanism

In Chapter 3, we discussed the axion as a compelling candidate for DM arising from the Peccei-Quinn solution to the strong CP problem. We explored how axions can be produced through various mechanisms, including the misalignment mechanism. Chapter 2 introduced the theoretical framework for FOPTs in the early universe. Building on these foundations, we now investigate how FOPTs affect axion dynamics and their implications for DM production. This chapter presents a replication of the recent work by Lee et al. [2] on the bubble misalignment mechanism for axions. While building upon their theoretical framework, this thesis contributes several significant original results: we develop novel multi-bubble simulations that verify the predicted $N^{1/3}$ scaling of axion number density with bubble count, implement dynamic bubble wall evolution incorporating axion pressure feedback effects, and conduct systematic investigations revealing distinct velocity-dependent scaling regimes. Our numerical simulations extend beyond previous work by including realistic pressure effects that modify bubble wall dynamics, providing the first comprehensive verification of Fermi acceleration mechanisms in multi-bubble environments, and demonstrating how axion-induced pressure influences the coupled bubble-field evolution.

In conventional axion cosmology, the misalignment mechanism assumes a relatively smooth evolution of the axion mass with temperature. However, in scenarios where axions couple to non-Abelian gauge fields undergoing a FOPT from a deconfined to a confined phase, the axion mass can change discontinuously. Nakagawa et al. [1] demonstrated that such discontinuous changes can significantly enhance the abundance of axions compared to scenarios with continuous mass evolution. Their study, however, did not account for the spatial inhomogeneities inherent in bubble nucleation processes. Lee et al. [2] extended this analysis by explicitly considering bubble formation and coalescence during FOPTs. As they note, "bubble formation and coalescence in the FOPTs create spatial inhomogeneity, an effect that has not been considered in previous literature."

This spatial inhomogeneity fundamentally alters axion dynamics in several important ways. When bubbles of true vacuum nucleate within the false vacuum during FOPTs, the axion mass differs between the inside and outside of these bubbles. This mass difference creates an effective potential barrier in the bubble walls. Depending on the axion mass ratio and the velocity of the bubble wall, axions can be initially expelled from the bubbles. Expelled axion waves then propagate through the false vacuum and scatter off other expanding bubble walls.

A key insight from the "bubble misalignment mechanism" is the identification of a Fermi acceleration process for axion waves. When axion waves repeatedly scatter off multiple bubble walls, they gain energy with each collision, analogous to the Fermi acceleration mechanism familiar from cosmic ray physics. As these axion waves become more energetic, they eventually gain sufficient momentum to penetrate the bubbles, maintaining the conservation of the axion number. This mechanism can substantially modify both the abundance and momentum distribution of axion DM compared to scenarios discussed in Chapter 3.3. For certain parameter regimes, axion production can be significantly enhanced, with implications for the viable parameter space of axion models. Additionally, the resulting spatial inhomogeneities could lead to the formation of axion miniclusters and other observable signatures.

In this chapter, we will systematically analyze the bubble misalignment mechanism, classify the different regimes of axion dynamics, and examine the physics of axion-bubble interactions. We will also discuss the how the multiple bubbles affect the system. Throughout this chapter, we follow the convention where m_0 represents the axion mass inside bubbles (true vacuum), m_b represents the axion mass outside bubbles (false vacuum) at the bubble nucleation temperature, H_b represents the Hubble parameter at bubble nucleation, and β represents the inverse duration of the phase transition.

4.1 Classification of Axion Dynamics during Phase Transitions

The interplay between axion oscillations and bubble nucleation during FOPTs leads to rich phenomenology compared to the conventional misalignment mechanism discussed in Section 3.3.2. The dynamics can be classified based on the hierarchy between four critical timescales: m_0, m_b, H_b, and β. In our analysis, we assume $\beta > H_b$ (the phase transition proceeds faster than cosmic expansion) and $m_0 > m_b$ (the axion mass increases inside bubbles), which are natural conditions for many realistic FOPT scenarios. Based on these parameters, we can classify the axion dynamics into four distinct regimes.

(a) Late Oscillation Regime $(3H_b > m_0)$ In this regime, the axion does not oscillate even after the FOPTs are completed, but begins oscillations later when $m_0 \approx 3H$. The oscillation temperature is given by:

$$T_{\mathrm{osc},(a)} \simeq \left(\frac{10}{\pi^2 g_{*,\mathrm{osc}}}\right)^{1/4} \sqrt{\frac{M_{Pl}}{m_0}} \tag{4.1}$$

The resulting axion energy density follows the standard result for constant-mass axions:

$$\rho_\phi^{(a)}/s = \frac{45}{4\pi^2 g_{*s,\mathrm{osc}}} \left(\frac{\pi^2 g_{*,\mathrm{osc}}}{10}\right)^{3/4} \frac{m_0^{1/2}\phi_0^2}{M_{Pl}^{3/2}} \tag{4.2}$$

This matches our earlier discussion in Section 3.3.2, as expected since in this case the axion only begins oscillating after the FOPT is complete.

(b) Rapid Transition Regime ($\beta > m_0 > m_b, 3H_b$) In this regime, FOPTs occurs more rapidly than any other relevant timescale. This regime can be further subdivided into two cases.

Case b1: $m_b < 3H_b$ — The axion has not yet started oscillating before the FOPTs. After the transition, it immediately begins oscillating with mass m_0, giving:

$$\rho_\phi^{(b1)}/s = \frac{45 m_0^2 \phi_0^2}{4\pi^2 g_{*s,b} T_b^3} \tag{4.3}$$

Case b2: $m_b > 3H_b$ — The axion has already started oscillating before the FOPTs. The energy density after the transition depends on the oscillation phase α_b:

$$\rho_\phi^{(b2)}(T_b) = \frac{\bar{\phi}_b^2}{2}(m_b^2 \cos^2 \alpha_b + m_0^2 \sin^2 \alpha_b) \tag{4.4}$$

This shows a potential enhancement of up to m_0^2/m_b^2 compared to scenarios with continuous mass evolution.

(c) Early Oscillation Regime ($m_b > \beta$) In this regime, the axion has already begun oscillating before the FOPTs, and it continues oscillating outside the bubbles during the transition. The key feature distinguishing this case from the previous ones is the interaction between axion waves and bubble walls. As we shall see later, when m_0 exceeds γm_b (where γ is the Lorentz factor of the bubble wall), the axions are initially reflected from the bubble walls rather than transmitted through them. This reflection creates a situation where axion waves bounce between expanding bubble walls. With each reflection, the axion waves gain energy through a mechanism analogous to Fermi acceleration. Eventually, after multiple reflections, the axions gain sufficient energy to penetrate the bubbles. Importantly, while the axion abundance in this regime remains similar to that in the second-order phase transition case, the momentum distribution is changed by this acceleration process. This can have significant implications for the subsequent formation of structures and potentially observable signatures.

(d) Intermediate Regime ($m_0 > \beta > m_b, 3H_b$) In the final regime, the axion does not oscillate outside the bubbles during the FOPTs, but the transition proceeds slowly enough so that the axion field responds to the changing mass inside the bubbles. This creates a unique phenomenon described as "axion shock waves" – where the axion field is depleted inside bubbles and forms a propagating wave front. The axion shock wave propagates outward from each bubble at the speed of light, creating a distinctive spatial distribution where the axion field transitions from zero inside the bubble to its initial value far from the bubble. As these shock waves encounter other bubble walls, they undergo Fermi acceleration similar to case (c), but with different initial conditions. A key characteristic of this regime is that the resulting axion number density scales inversely with the typical distance between bubbles. This distinguishes it from case (c), where the axion is distributed throughout space

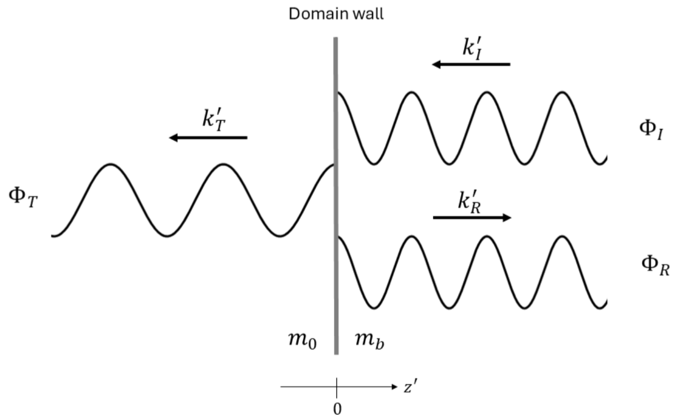

Figure 4.1: Schematic representation of axion wave reflection and transmission at a domain wall in the wall's rest frame. The incident wave Φ_I with wavevector k_I' approaches the wall from the right. Part of the wave is reflected back (Φ_R with wavevector k_R'), while another part is transmitted through the wall (Φ_T with wavevector k_T'). The difference in axion mass (m_0 inside versus m_b outside) determines the reflection and transmission coefficients. Reproduced from [2]

before the FOPTs. The velocity dependence of this phenomenon has been verified through detailed numerical simulations. In the following sections, we will explore the physics of each regime in greater detail, focusing particularly on the novel wave dynamics at bubble walls in cases (c) and (d).

4.2 Wave Dynamics at Bubble Walls

The effect of bubble wall passage on oscillating axion fields can be analyzed in terms of reflection and transmission of axion waves. While the full dynamics involves randomly generated spherical bubble walls throughout space, the essential physics can be understood by examining the interaction of axion waves with planar bubble walls.

4.2.1 Reflection and Transmission Analysis

To analyze this process, we consider a bubble wall moving along the z-axis with velocity v. It is convenient to define a coordinate system (t, z) such that the position of the wall is represented by $z = vt$. For analysis of transmission and reflection, we transform to the rest frame of the bubble wall using the Lorentz transformation:

$$t' = \gamma(t - vz) \tag{4.5}$$
$$z' = \gamma(z - vt) \tag{4.6}$$

where $\gamma = 1/\sqrt{1 - v^2}$ is the Lorentz factor, and the wall is located at $z' = 0$ in this frame. In the wall's rest frame, an incident axion wave propagating from the positive to negative direction along the z'-axis can be written as:

$$\Phi_I = \phi_0 \exp[i(\omega' t' + k'_I z')] \tag{4.7}$$

where the real part of Φ corresponds to the axion field value. When this wave encounters the bubble wall, part of it is transmitted into the bubble (Φ_T) and the other part is reflected (Φ_R). At the wall ($z' = 0$), the following boundary conditions must be satisfied:

$$\Phi_I[t', 0] + \Phi_R[t', 0] = \Phi_T[t', 0] \tag{4.8}$$

$$\partial_{z'}\Phi_I[t', 0] + \partial_{z'}\Phi_R[t', 0] = \partial_{z'}\Phi_T[t', 0] \tag{4.9}$$

to ensure the continuity of the field and its derivative across the wall. While these boundary conditions may appear to be imposed externally, they in fact arise naturally from the requirement that the axion field must satisfy the Klein-Gordon equation in a distributional sense across the discontinuity in the mass term. Specifically, if we integrate the equation $(\Box + m^2(t, r))\phi(t, r) = 0$ in an infinitesimally thin region containing the bubble wall, the requirement that the equation remains well defined implies the continuity of both ϕ and $\partial_z\phi$. These conditions also ensure that the energy density remains finite everywhere, preventing unphysical singularities at the wall interface. Solving these equations yields:

$$\Phi_R[t', z'] = \frac{k'_I - k'_T}{k'_I + k'_T}\phi_0 \exp[i(\omega' t' - k'_R z')] \tag{4.10}$$

$$\Phi_T[t', z'] = \frac{2k'_I}{k'_I + k'_T}\phi_0 \exp[i(\omega' t' + k'_T z')] \tag{4.11}$$

with:

$$k'_R = k'_I, \quad k'_T = \sqrt{k'^2_I + m_b^2 - m_0^2} \tag{4.12}$$

A crucial feature of this solution is the conservation of axion number during wall interactions:

$$k'_I|\Phi_I[t', 0]|^2 = k'_R|\Phi_R[t', 0]|^2 + k'_T|\Phi_T[t', 0]|^2 \tag{4.13}$$

This equation expresses that the axion flux incident on the wall equals the sum of reflected and transmitted fluxes, confirming that axions are neither created nor destroyed during wall interactions.

4.2.2 Conditions for Transmission and Reflection

In case (c) described in Section 4.1, the axion field just before bubble nucleation can be expressed as:

$$\Phi_I(t, z) = \bar{\phi}_b \exp[im_b t] \tag{4.14}$$

in the cosmological frame, where $\bar{\phi}_b$ is the oscillation amplitude of the axion field at the time of bubble nucleation. Transforming to the wall frame, this becomes:

$$\Phi_I(t', z') = \bar{\phi}_b \exp[i(\omega_0' t' + k_{I0}' z')], \tag{4.15}$$

with $\omega_0' = m_b\gamma$ and $k_{I0}' = m_b v\gamma$. The momentum of the transmitted wave is then:

$$k_{T0}' = \sqrt{\gamma^2 m_b^2 - m_0^2}. \tag{4.16}$$

This equation shows crucial condition for our mechanism: when $m_0 > \gamma m_b$, the value of k_{T0}' becomes imaginary, indicating that the axion field exponentially decays inside the bubble – a signature of total reflection. In this scenario, the amplitudes of the reflected and incident waves are nearly equal, differing only by a phase shift. It means that repeated reflections modify the wave's energy, eventually leading to transmission when energy becomes sufficiently high. This is the fundamental difference between the standard mechanisms and the bubble misalignment mechanism.

4.2.3 Implication for Axion Abundance

Unlike the spatially uniform case discussed in Section 3.3.2, where the axion number can change during a sudden mass increase, the bubble misalignment mechanism preserves the total axion number. This conservation is evident in Eq. (4.13), which maintains the continuity of the axion flux across the bubble walls. In the case where the axions are already oscillating before FOPTs, the final abundance remains similar to the second-order phase transition. However, the momentum distribution of these axions is dramatically altered by the Fermi acceleration process, potentially leading to different observational signatures. For case (d), the situation is more complex. Axion shock waves form around expanding bubbles, and the number density of axions scales inversely with the typical distance between bubbles. This happens because in case (d), axion waves are limited to the area just outside the bubbles, leading to a unique arrangement that is very different from case (c). To analyze the detailed evolution of these processes, we performed multiple numerical simulations.

4.3 Fermi Acceleration of Axion Waves

The reflection of axion waves from bubble walls established in the previous section causes a mechanism by which these waves gain energy through multiple scatterings. This process is very similar to Fermi acceleration, originally proposed as an explanation for high-energy cosmic rays [55].

4.3.1 The Acceleration Mechanism

Examination of the wave dynamics of the axion requires consideration of a simplified $(1+1)$d spacetime model with two bubble walls approaching, each moving with velocity v. The wall moving in the positive z-direction may be designated as the "up wall," while its counterpart moving in the negative direction constitutes the "down wall." An axion wave with four-momentum $\{\omega, -k\}$ in the cosmological frame transforms when encountering the up wall. The Lorentz transformation matrix connecting the cosmological frame to a frame moving with velocity v is given by:

$$\Lambda(v) = \begin{pmatrix} \gamma & v\gamma \\ v\gamma & \gamma \end{pmatrix}, \tag{4.17}$$

where $\gamma = 1/\sqrt{1-v^2}$ represents the Lorentz factor. For the up wall moving with velocity v, the inverse transformation $\Lambda(-v)$ gives the wave's momentum in the wall's rest frame: $\Lambda(-v) \cdot \{\omega, -k\}$. There is a negative sign in $\Lambda(-v)$ to account for transforming to the reference frame of a wall moving with velocity $+v$ in the cosmological frame. Upon reflection, the spatial component of momentum reverses while the energy remains invariant in the wall's rest frame. This reflection corresponds to application of the parity operator $\hat{P} = \mathrm{diag}(1, -1)$, yielding a post-reflection momentum of $\hat{P} \cdot \Lambda(-v) \cdot \{\omega, -k\}$ in the wall frame. The parity operator has 1 in the time component because energy is conserved during reflection in the wall frame, and -1 in the spatial component because momentum direction reverses during reflection. Transformation back to the cosmological frame requires application of $\Lambda(v)$, resulting in $\Lambda(v) \cdot \hat{P} \cdot \Lambda(-v) \cdot \{\omega, -k\}$ for the momentum after one reflection. This transformation sequence captures the energy transfer from the moving wall to the axion, making it similar to the Fermi acceleration. After n reflections between the approaching walls, the momentum becomes:

$$p^{\mu}[n] = \hat{P}^{n} \cdot (\Lambda(-v))^{2n} \cdot \{\omega, -k\}, \tag{4.18}$$

and we can express it using rapidity ψ (defined by $\tanh\psi = v$) as:

$$p^{\mu}[n] = \hat{P}^{n} \cdot \begin{pmatrix} \cosh(2n\psi) & \sinh(-2n\psi) \\ \sinh(-2n\psi) & \cosh(2n\psi) \end{pmatrix} \cdot \{\omega, -k\}. \tag{4.19}$$

The angular frequency component evolves as:

$$p^{0}[n] = \frac{1}{2}\left[(w+k)\left(\frac{1+v}{1-v}\right)^{n} + (w-k)\left(\frac{1-v}{1+v}\right)^{n}\right]. \tag{4.20}$$

For large n and nonzero $(w+k)$, the first term dominates since $(1+v)/(1-v) > 1$ for positive v. This establishes exponential energy growth with reflection number. The physical interpretation is clear: axion waves gain energy with each reflection, similar to how cosmic rays are accelerated by colliding shock fronts.

4.3.2 Number of Reflections and Critical Energy

The acceleration process eventually stops due to the finite duration of the phase transition and the approaching bubble walls. Determining the maximum reflection number requires tracking the wall separation throughout the process. Denoting the initial wall separation as L and the separation at the n-th reflection as $L_w[n]$, with $L_w[1] = L$, the separation evolution follows from the relative motion of walls and axion waves. After the first reflection from the wall, the wave propagates toward the other wall. The time required for the propagation can be estimated using the wall velocity (we denote that the axion wave travels at speed of light for simplicity) as $L/(1+v)$. During the time of propagation, the walls distance changes as well by $2v \cdot L/(1+v)$, which gives us the separation for the second reflection:

$$L_w[2] = L - 2v\frac{L}{1+v} = L\left(1 - \frac{2v}{1+v}\right) = \frac{1-v}{1+v}L. \tag{4.21}$$

Continuing this analysis establishes the recursive relation:

$$L_w[n+1] = \left(\frac{1-v}{1+v}\right)^n L, \tag{4.22}$$

and we can generalize this relation to calculate the reflection number n for a given wall separation:

$$n = \frac{\log \frac{L}{L_w[n+1]}}{\log \frac{1+v}{1-v}}. \tag{4.23}$$

For axion waves with initial angular frequency $\omega = m_b$ and negligible initial momentum ($k = 0$), which approximates newly oscillating axions, the energy after n reflections becomes:

$$p^0[n] = \frac{m_b}{2}\left(\frac{L}{L_w[n+1]} + \frac{L_w[n+1]}{L}\right). \tag{4.24}$$

This directly correlates energy gain with wall separation reduction, providing understanding of the acceleration process.

4.3.3 Transmission Probability and Momentum Distribution

Acceleration continues until axion waves gain sufficient energy for transmission through bubble walls. In the wall rest frame, transmission occurs when:

$$\omega'_n > m_0. \tag{4.25}$$

The critical reflection number n_c depends on both the wall velocity v and the mass ratio m_0/m_b. Lower velocities give smaller energy gains per reflection, requiring more reflections to achieve transmission. Similarly, larger mass ratios increase the transmission threshold, also requiring additional reflections. Fig. 4.2 illustrates this dependence, showing that smaller v and larger m_0/m_b result in higher values of n_c. Upon reaching the critical energy threshold, axion waves begin transmitting into bubbles with increasing probability in subsequent reflections. Transmission and reflection coefficients at the (n_c+i)-th collision are determined by:

$$t_i = \left|\frac{2k'_{I,n_c+i}}{k'_{I,n_c+i} + k'_{T,n_c+i}}\right|^2 \times \frac{k'_{T,n_c+i}}{k'_{I,n_c+i}} \tag{4.26}$$

$$r_i = \left|\frac{k'_{I,n_c+i} - k'_{T,n_c+i}}{k'_{I,n_c+i} + k'_{T,n_c+i}}\right|^2, \tag{4.27}$$

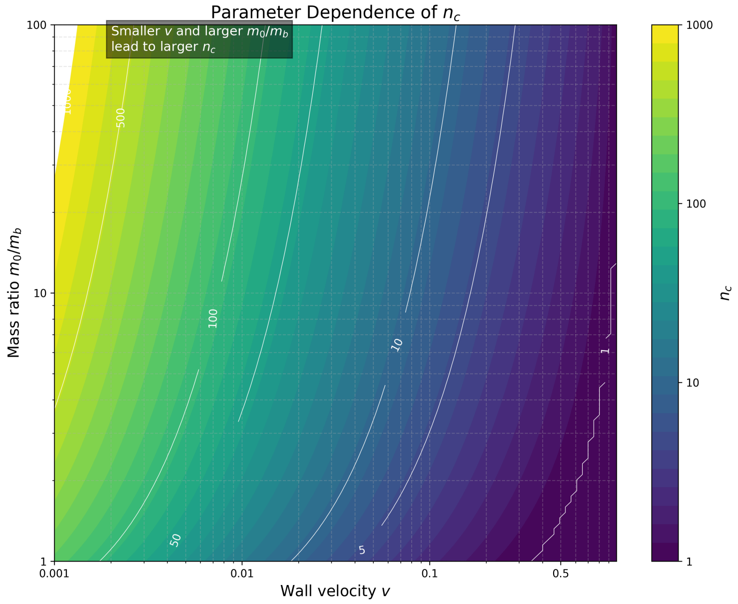

Figure 4.2: Dependence of the critical reflection number n_c on wall velocity v and mass ratio m_0/m_b. Smaller v and larger m_0/m_b lead to higher n_c, as more reflections are required to reach the transmission threshold. Reproduced from [2].

where $k'_{I,n} = \sqrt{\omega_n'^2 - m_b^2}$ and $k'_{T,n} = \sqrt{\omega_n'^2 - m_0^2}$ represent momenta outside and inside the bubble, respectively. The fraction of axions transmitted at the $(n_c + i)$-th collision, denoted F_i, follows:

$$F_0 \equiv t_0 \tag{4.28}$$

$$F_i \equiv t_i \cdot r_0 \cdots r_{i-1} \quad (i \geq 1). \tag{4.29}$$

This represents the probability of i reflections after reaching critical energy before transmission at the $(n_c + i)$-th collision. The sum of all F_i approaches unity, preserving total axion number.

4.3.4 Spatial Inhomogeneities and Structure Formation

The Fermi acceleration process generates axions with a non-thermal momentum distribution, as axions gain energy through discrete, directional collisions with bubble walls rather than random thermal interactions. We can approximate that the transmitted axion momentum (approximated by k_{T,n_c}) scales as $\sqrt{v}$ for $v < O(0.1)$, due to the limited energy gain per collision. For $v > O(0.1)$, the transmitted momentum spans a broader range, including negative values that indicate outward propagation in the bubble. Accordingly, these transmitted axions will exhibit mostly non-relativistic or marginally non-relativistic momenta. Because the axions are marginally non-relativistic, the spatial inhomogeneities induced during the FOPTs may persist throughout cosmic evolution, potentially enabling structure formation

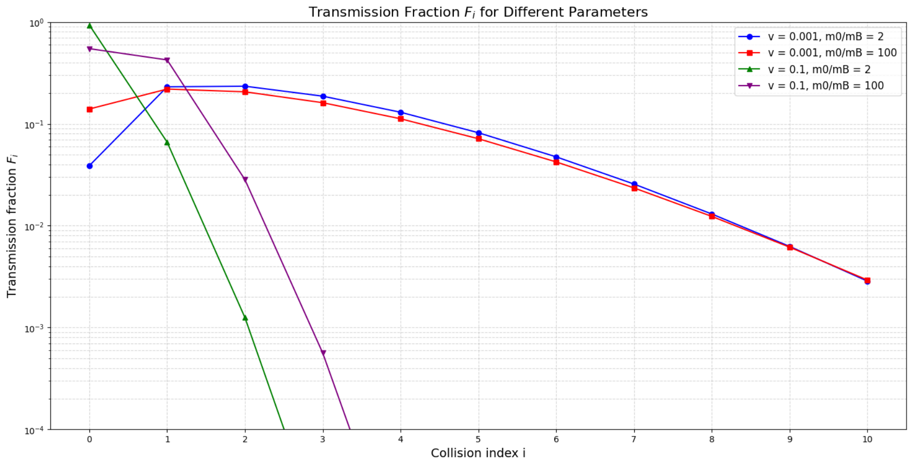

Figure 4.3: Transmission fraction F_i as a function of the collision index i for different values of wall velocity v and mass ratio m_0/m_b. Higher velocities result in faster transmission, while smaller velocities require more reflections before significant transmission occurs. Reproduced from [2].

at small scales - important requirement for DM candidates discussed in Section 1.1.3. The characteristic spatial scale of these inhomogeneities is estimated as:

$$l \simeq R \left(\frac{1-v}{1+v} \right)^{n_c} \simeq \frac{v}{\beta} \frac{m_b}{2m_0}, \tag{4.30}$$

where $R \approx v/\beta$ represents typical inter-bubble distance at formation. This scale corresponds to bubble wall separation at initial axion transmission, establishing the fundamental scale of axion field inhomogeneities post-FOPTs. Subsequently, these inhomogeneities evolve under cosmic expansion and axion kinetic energy. Axions free-stream approximately $(k_{T,n_c}/m_0)H_b^{-1}$ during one Hubble time. When this free-streaming length is smaller than the characteristic scale l, spatial inhomogeneities persist, potentially seeding axion minicluster formation. This condition requires β/H_b to be relatively small (phase transition timescale is greater than Hubble time) and transmitted axion velocities remain below bubble wall velocity. These conditions allow the bubble misalignment mechanism to create distinctive small-scale DM structures not seen in other standard production models. The Fermi acceleration mechanism thus fundamentally modifies both momentum and spatial distributions of axion DM, with significant implications for structure formation and potentially observable consequences in cosmic large-scale structure.

4.4 Axion Shock Waves

While Section 4.3 focused on the dynamics of case (c) where axions were already oscillating before the FOPTs, this section examines the unique phenomena for case (d), where $m_0 > \beta > m_b, 3H_b$. In this regime, the axion does not oscillate outside the bubbles during the phase transition, but the transition proceeds slowly enough

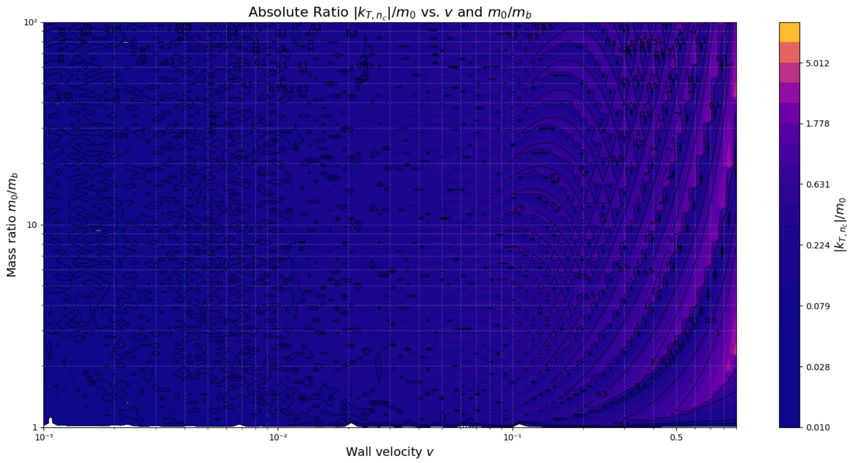

Figure 4.4: Absolute ratio $|k_{T,n_c}|/m_0$ as a function of wall velocity v and mass ratio m_0/m_b. For $v < O(0.1)$, the transmitted momentum scales approximately as $\sqrt{v}$, while for larger velocities, it spans a broader range. Negative values correspond to outward propagation inside the bubble. Reproduced from [2].

that the axion field responds to the changing mass inside the bubbles. This leads to the formation of what paper [2] describes as 'axion shock waves'. To analyze the axion dynamics just after bubble nucleation in case (d), we consider the equation of motion for a spherically symmetric configuration:

$$\left(\frac{\partial^2}{\partial t^2} - \frac{1}{r^2}\frac{\partial}{\partial r}r^2\frac{\partial}{\partial r} + m^2(t,r)\right)\phi(t,r) = 0. \tag{4.31}$$

This can be rewritten in terms of the variable $u = r\phi$:

$$\left(\frac{\partial^2}{\partial t^2} - \frac{\partial^2}{\partial r^2} + m^2(t,r)\right)u(t,r) = 0, \tag{4.32}$$

where the mass term $m^2(t,r)$ is given by:

$$m^2(t,r) = \begin{cases} m_0^2 & \text{for } 0 \le r < vt \\ m_b^2 & \text{for } r > vt. \end{cases} \tag{4.33}$$

In case (d) with $m_b < \beta$, we can approximate $m_b \approx 0$ during the FOPTs. The initial conditions are:

$$\phi(t=0,r) = \phi_b, \quad \frac{\partial\phi}{\partial t}(t=0,r) = 0. \tag{4.34}$$

As the bubble expands, the axion field inside the bubble rapidly oscillates due to the large mass m_0, and these oscillations cause the field to effectively average to zero. This depletion of the axion field inside the bubble propagates outward from the bubble wall at the speed of light, creating a characteristic wave front. For bubble

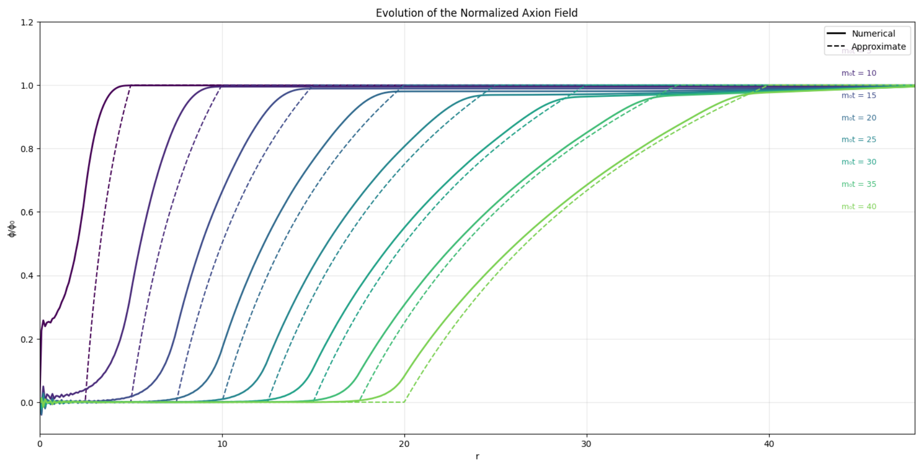

Figure 4.5: Comparison between the numerical solution (solid lines) and the approximate solution (dashed lines) for the evolution of the normalized axion field. The agreement improves at later times, confirming the validity of the approximation. Reproduced from [2].

wall velocities smaller than the speed of light, an approximate solution for the axion field can be derived:

$$\phi(t,r) \approx \begin{cases} 0 & \text{for } 0 \le r < vt \\ \left[1 - \frac{v(t-r)}{(1-v)r}\right]\phi_b & \text{for } vt \le r < t \\ \phi_b & \text{for } r \ge t. \end{cases} \tag{4.35}$$

This solution describes a field configuration where inside the bubble ($r < vt$), the axion field is basically zero; in an intermediate region ($vt \le r < t$), the field transitions from zero to its initial value; and beyond the light cone from the nucleation point ($r \ge t$), the field remains at its initial value ϕ_b. This field configuration, "axion shock wave," differs fundamentally from the oscillating waves discussed in case (c). The shock wave represents a propagating disturbance in the axion field that carries energy outward from the expanding bubble. In Fig. 4.5, we illustrate the evolution of the axion field, comparing the approximate analytical solution with numerical results. As seen in the figure, the approximate solution closely follows the numerical simulation, particularly at later times, validating its applicability. The energy of the radiated axion wave can be estimated by integrating over the transitional region:

$$E_\phi \equiv 4\pi \int_{\mathrm{vt}}^{t} dr\, r^2 \frac{(\partial_t\phi)^2 + (\partial_r\phi)^2}{2} \approx 2\pi \frac{v(1+v)}{1-v}\phi_b^2 t. \tag{4.36}$$

The typical momentum of the axion field in this shock wave is approximately:

$$k_{\mathrm{typ}} \equiv \left.\frac{\partial_r\phi}{\phi}\right|_{r=(1+v)t/2} \approx \frac{4v}{(1-v^2)t}. \tag{4.37}$$

From these quantities, the axion number associated with a single bubble before collisions can be estimated:

$$N_\phi \equiv \frac{E_\phi}{k_{\rm typ}} \approx \frac{\pi\phi_b^2}{2}(1+v)^2 t^2. \tag{4.38}$$

This shows that the **axion number increases quadratically** with time, indicating that axion waves continue to be produced as the bubble expands. Since axion number is conserved in reflections and transmissions at bubble walls, the final axion number density after the FOPTs can be expressed as:

$$n_\phi \equiv \frac{N_\phi}{L^3} \approx \frac{\pi\phi_b^2}{2L}. \tag{4.39}$$

where L is the typical distance between bubbles. A crucial point here is that the axion number density is inversely proportional to L, in contrast to case (c), where the axion number density is independent of the bubble separation. This inverse relationship occurs because in case (d), axion waves are produced only in the region just outside the bubble walls, rather than being present throughout space from the beginning as in case (c). Consequently, as the distance between bubbles increases, fewer axion waves are produced per unit volume. To determine the energy density from this number density, we must consider that after the axions penetrate the bubble walls through the Fermi acceleration process, they acquire the mass m_0 of the true vacuum. The energy density is thus obtained by multiplying the number density by the axion mass:

$$\rho_\phi^{(d)} = n_\phi \times m_0 = \frac{\pi\phi_b^2}{2L} \times m_0. \tag{4.40}$$

This expression reveals the distinctive scaling of the axion energy density in the intermediate regime: it is inversely proportional to the typical bubble separation L and directly proportional to both the initial field value squared and the axion mass inside bubbles. Substituting $L \approx v/\beta$, which relates the bubble separation to the wall velocity and transition rate, we obtain:

$$\rho_\phi^{(d)} \simeq \frac{\pi\phi_b^2\beta}{2v} \times m_0. \tag{4.41}$$

This scaling makes the intermediate regime particularly sensitive to the dynamics of the phase transition, with the axion abundance enhanced for rapid transitions (large β) and suppressed for high wall velocities (large v).

4.4.1 Numerical Verification

Three-dimensional lattice simulations with periodic boundary condition numerically verified the analytical predictions from previous sections. The simulation placed a single bubble at the center of a cubic lattice box with periodic boundaries, which effectively models an infinite array of bubbles separated by the box size L. The computational grid had a resolution of $N_{\rm grid}^3$ grid points and used a smooth transition model for the axion mass to avoid abrupt step function discontinuities. The timestep was selected using the Courant-Friedrichs-Lewy (CFL) condition to ensure numerical stability, with the condition typically requiring that the timestep satisfy $\Delta t \leq \frac{\Delta x}{v_{\max}}$, where Δx represents the spatial grid spacing and $v_{\max}$ is the maximum wave propagation velocity in the system.

In these simulations, the bubble walls were assigned a constant expansion velocity v. Although bubbles physically nucleate at rest ($v = 0$), this assigned velocity represents the terminal velocity that bubbles would rapidly reach due to interactions with the surrounding plasma.

The field evolution employed a Velocity Verlet symplectic integrator, a numerical method particularly suited for oscillatory systems like the axion field. This integration scheme uses staggered momentum and position updates to preserve the Hamiltonian structure of the field equations, ensuring accurate long-term evolution without spurious energy drift. The algorithm first updates momentum by a half-step, advances the position fully, and then completes the momentum update, effectively maintaining the physical properties of the system [56]. The small value of m_b was chosen to align with the theoretical assumptions, ensuring that the axion field dynamics closely matched the predicted theoretical behavior. The energy evolution in such a setup is shown in Fig. 4.11, illustrating the total energy density and the energy contained inside the bubble as a function of time. The simulations used $N_{\text{grid}} = 128$

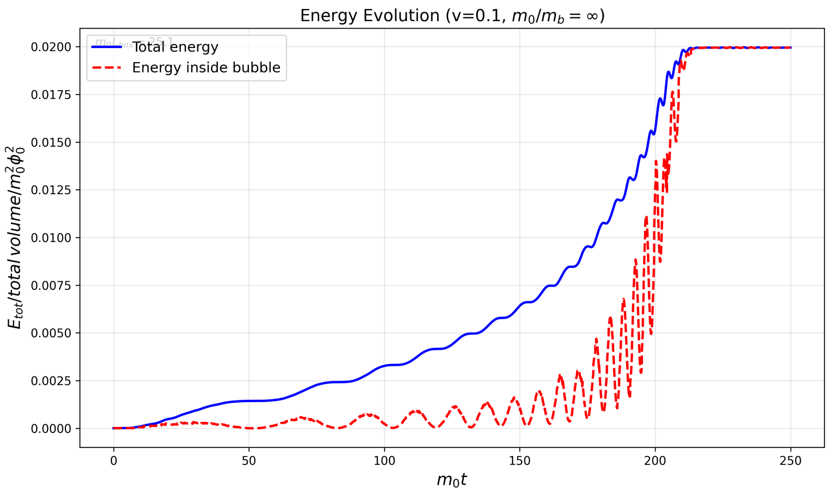

Figure 4.6: Evolution of the total energy density (solid blue) and energy inside the bubble (dashed red) for $v = 0.1$ and $m_0/m_b = \infty$. The results are obtained from three-dimensional lattice simulations, confirming that energy accumulates inside the bubble before eventually stabilizing. Reproduced from [2].

resolution, a periodic box of size 8π, and a smooth transition model without a step function. The numerical results show that the axion number density after the phase transition scales as L^{-1} (Fig. 4.7), in excellent agreement with the analytical prediction shown earlier. Additionally, the dependence on the wall velocity v follows approximately:

$$n_\phi = C v^\alpha \frac{\phi_0^2}{L} \tag{4.42}$$

where $C \approx 1.3$ and $\alpha \approx 0.4$ for $v \lesssim 0.4$, while $C \approx 1.8$ and $\alpha \approx 0.8$ for $v \gtrsim 0.4$. Fig. 4.7 and Fig. 4.8 illustrate these relationships.

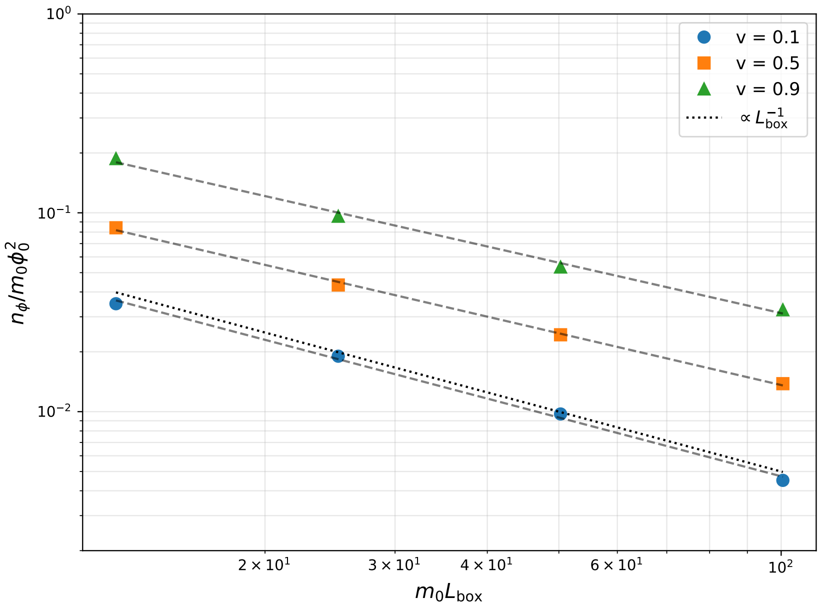

Figure 4.7: Axion number density n_ϕ as a function of box size L for different bubble wall velocities. The scaling approximately follows L^{-1}, as predicted analytically. Reproduced from [2]

The momentum distribution of axions after the phase transition is non-thermal and depends on the wall velocity (See Fig.4.9). The axions are typically marginally non-relativistic, with higher wall velocities producing more energetic axions. The momentum distribution of axions after the phase transition is calculated by transforming the axion field and its time derivative to Fourier space. For a given simulation with $L_{\rm box} = 16\pi$ for field values ϕ and $\dot{\phi}$ we compute::

$$n(k) = \frac{k^3}{2\pi^2 2\omega_k V}\left[\dot{\phi}_k^2 + \omega_k^2 \phi_k^2\right], \tag{4.43}$$

where ϕ_k and $\dot{\phi}_k$ are the Fourier transforms of the field and its time derivative respectively, $\omega_k = \sqrt{k^2 + m_0^2}$ is the energy of a mode with momentum k, and V is the simulation volume. The distribution is normalized by $m_0\phi_0^2$ to obtain dimensionless quantities suitable for comparison across different parameter sets. In summary, the axion shock waves produced in case (d) represent a different production mechanism for axion DM with distinctive features in both abundance and momentum distribution. This mechanism complements the Fermi acceleration process discussed in case (c), further enriching the phenomenology of the bubble misalignment mechanism.

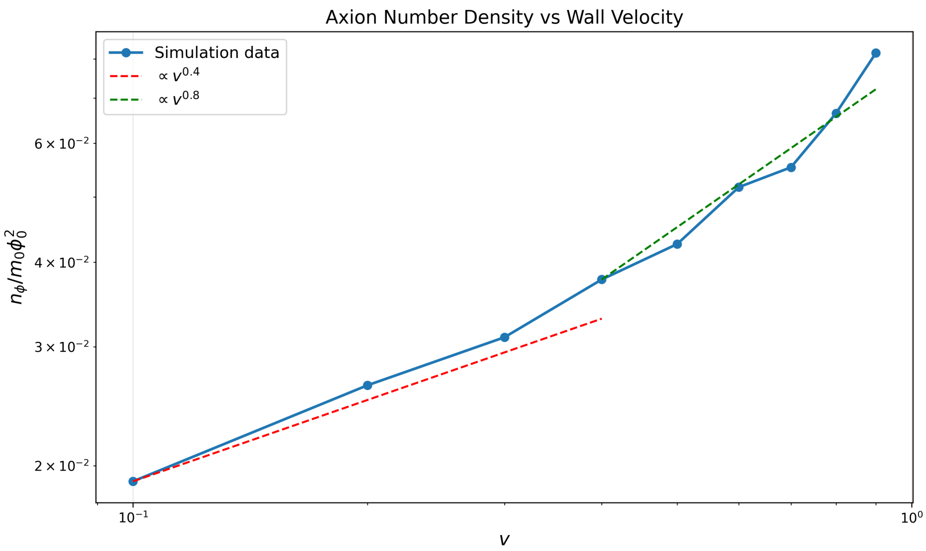

Figure 4.8: Axion number density n_ϕ as a function of bubble wall velocity v. Different velocity regimes exhibit distinct scaling behavior, with $n_\phi \propto v^{0.4}$ for $v \lesssim 0.4$ and $n_\phi \propto v^{0.8}$ for $v \gtrsim 0.4$. Reproduced from [2]

4.5 Axion Abundance

Having analyzed the dynamics of axion waves during first-order phase transitions, we now examine how these processes affect the relic abundance of axion dark matter. This section provides a summary of the key results and physical insights for each dynamical regime. Detailed derivations of all formulas can be found in Appendix B.

The bubble misalignment mechanism leads to distinctive abundance patterns across the different regimes classified in Section 4.1. To contextualize these results, we first consider the benchmark case of a second-order phase transition, where the axion mass evolves continuously with temperature according to:

$$\chi(T) \approx \begin{cases} \chi_0 & \text{for } T < \Lambda \\ \chi_0 \left(\frac{T}{\Lambda}\right)^{-p} & \text{for } T \geq \Lambda. \end{cases} \tag{4.44}$$

In this scenario, the axion abundance is given by:

$$\rho_\varphi^{(2nd)}/s = \frac{45}{4\pi^2 g_{*s,\mathrm{osc}}} \left(\frac{\pi^2 g_{*,\mathrm{osc}}}{10}\right)^{\frac{p+6}{2(p+4)}} \frac{m_0 \varphi_0^2}{(m_b^2 M_{\mathrm{Pl}}^{p+6} T_b^p)^{\frac{1}{p+4}}}. \tag{4.45}$$

This expression serves as our reference point for examining how first-order transitions modify axion production.

4.5.1 Physical Insights Across Dynamical Regimes

Case (a): Late Oscillation Regime ($3H_b > m_0$) In this regime, the axion remains effectively massless throughout the phase transition and begins oscillating only after

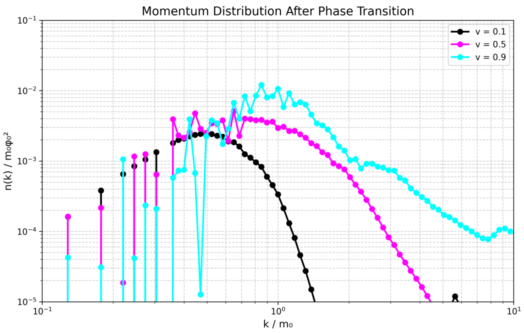

Figure 4.9: Momentum distribution $n(k)$ of axions after the phase transition for different bubble wall velocities $v = 0.1$ (black), $v = 0.5$ (magenta), and $v = 0.9$ (cyan). Higher wall velocities produce axions with more energetic momentum distributions, as expected from the Fermi acceleration process. The distributions confirm that the axions are marginally non-relativistic. Reproduced from [2]

the FOPT has completed. The bubble dynamics therefore have no impact on the axion evolution, and the abundance follows the standard misalignment result for constant-mass axions:

$$\rho_\varphi^{(a)}/s = \frac{45}{4\pi^2 g_{*s,\mathrm{osc}}} \left(\frac{\pi^2 g_{*,\mathrm{osc}}}{10}\right)^{3/4} \frac{m_0^{1/2}\varphi_0^2}{M_{\mathrm{Pl}}^{3/2}}. \tag{4.46}$$

The key physical insight here is that when the axion mass remains smaller than the Hubble parameter throughout the transition, the FOPT's spatial inhomogeneity does not significantly impact the axion dynamics.

Case (b): Rapid Transition Regime ($\beta > m_0 > m_b, 3H_b$) This regime is characterized by a phase transition that proceeds more rapidly than any other relevant timescale, effectively appearing as an instantaneous mass change from the axion's perspective. The results depend on whether the axion had already begun oscillating before the transition: For case (b1) with $m_b < 3H_b$, the axion has not yet started oscillating before the FOPT. The energy density is:

$$\rho_\varphi^{(b1)}/s = \frac{45 m_0^2 \varphi_0^2}{4\pi^2 g_{*s,b} T_b^3}. \tag{4.47}$$

This expression reveals that the abundance depends directly on the nucleation temperature T_b rather than an oscillation temperature, leading to potentially different abundance patterns compared to continuous scenarios. For case (b2) with $m_b > 3H_b$, the axion has already started oscillating before the FOPT. The energy density depends on the oscillation phase α_b at the transition:

$$\rho_\varphi^{(b2)}/s \propto (m_b^2 \cos^2\alpha_b + m_0^2 \sin^2\alpha_b). \tag{4.48}$$

The phase-dependent term can enhance the abundance by up to a factor of m_0^2/m_b^2 compared to continuous mass evolution. This enhancement occurs when the phase transition happens to coincide with the moment when the axion field is at maximum displacement and zero velocity (maximum potential energy).

Case (c): Early Oscillation Regime ($m_b > \beta$)

In this case, the axion is already oscillating before the FOPT, and the transition proceeds slowly enough that the axion field dynamically responds to the expanding bubbles. The key physical effect is the conservation of axion number through the reflection and transmission processes at bubble walls, yielding:

$$\rho_\varphi^{(c)}/s = \frac{45}{4\pi^2 g_{*s,\mathrm{osc}}}\left(\frac{\pi^2 g_{*,\mathrm{osc}}}{10}\right)^{\frac{p+6}{2(p+4)}} \frac{m_0\varphi_0^2}{(m_b^2 M_{\mathrm{Pl}}^{p+6} T_b^p)^{\frac{1}{p+4}}}. \tag{4.49}$$

Remarkably, the abundance in this case equals that of a second-order transition, despite the fundamentally different dynamics. This is a direct consequence of axion number conservation during wall interactions. However, as we've seen in Section 4.3, the momentum distribution is dramatically modified by the Fermi acceleration process, with potential implications for structure formation.

Case (d): Intermediate Regime ($m_0 > \beta > m_b, 3H_b$) This regime exhibits the most distinctive behavior due to the formation of axion shock waves. For case (d1) with $m_b < 3H_b$, the energy density is:

$$\rho_\varphi^{(d1)}/s \simeq \frac{45Cv^{-1+\alpha}\beta m_0\varphi_0^2}{2\pi^2 g_{*s,b}T_b^3} \tag{4.50}$$

where C and α are velocity-dependent coefficients determined from simulations. The key physical insight is that the abundance scales with β and inversely with velocity, making it sensitive to the phase transition dynamics. This unique scaling arises from the interaction between axion shock waves and bubble walls, as discussed in Section 4.5.

For case (d2) with $m_b > 3H_b$, the result depends on the oscillation phase at the transition, with behavior ranging between case (b2) and case (d1) depending on the specific conditions.

4.5.2 Comparative Abundance Analysis

The ratio of axion abundance between first-order and second-order phase transitions provides a clear picture of the impact of bubble dynamics: For case (c), this ratio is unity due to axion number conservation:

$$\frac{\rho_\varphi^{(c)}}{\rho_\varphi^{(2nd)}} = 1. \tag{4.51}$$

For case (b1), the ratio depends on the oscillation temperature:

$$\frac{\rho_\varphi^{(b1)}}{\rho_\varphi^{(2nd)}} = \left(\frac{m_b}{m_0}\right)^{6/p} \times \left(\frac{T_{\mathrm{osc}}}{T_b}\right)^{(p+6)/2}. \tag{4.52}$$

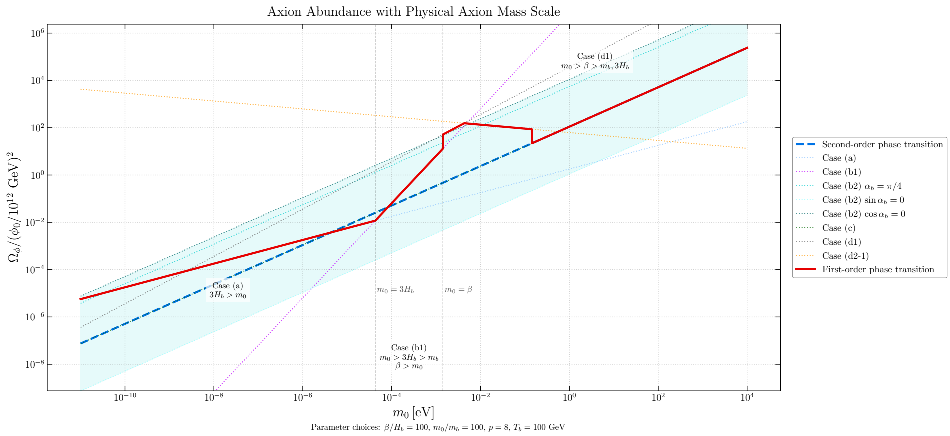

Figure 4.10: Normalized axion abundance $\Omega_\phi/(\phi_0/10^{12}\ \mathrm{GeV})^2$ as a function of axion mass m_0 for first-order (solid red line) and second-order (dashed blue line) phase transitions. Dotted lines show individual contributions from different dynamical regimes: (a) late oscillation regime ($3H_b > m_0$), (b1/b2) rapid transition regime with different oscillation phases, (c) early oscillation regime, and (d1/d2) intermediate regime. Vertical lines mark important transitions at $m_0 = 3H_b$ and $m_0 = \beta$. The light cyan shaded region indicates the range of possible values in the case (b2) regime due to different oscillation phases α_b at the time of transition. Key parameter values used in this calculation: $\beta/H_b = 100$, $m_0/m_b = 100$, $p = 8$, and $T_b = 100$ GeV.

For case (d1), the ratio becomes:

$$\frac{\rho_\varphi^{(d1)}}{\rho_\varphi^{(2nd)}} = Cv^{-1+\alpha} \times \frac{\beta}{H_b} \times \frac{T_b}{T_{\rm osc}} \times \left(\frac{m_b}{.} m_0\right)^{(4+p)/p} \tag{4.53}$$

These results demonstrate that the bubble misalignment mechanism provides a rich phenomenology for axion DM production. Depending on the specific parameters of the phase transition, the axion abundance can be enhanced, suppressed, or unchanged compared to continuous mass evolution scenarios, while the momentum distribution and spatial clustering properties may be significantly modified regardless of the abundance impact.

To better visualize the abundance of axions in different dynamical regimes, Fig. 4.10 presents the normalized axion density parameter,$\Omega_\phi/(\phi_0/10^{12}\ \mathrm{GeV})^2$, as a function of the axion mass, m_0. Normalization by $(\phi_0/10^{12}\ \mathrm{GeV})^2$ removes the dependence on the initial value of the axion field, allowing a direct comparison between different production scenarios. The solid red line represents the case of a FOPT, and the blue dashed line corresponds to the standard SOPT scenario discussed in the literature.

The enhancement of axion abundance in FOPTs relative to SOPTs is evident in certain mass ranges, particularly in the intermediate regime (case d1), where $m_0 > \beta > m_b, 3H_b$. In this regime, axion shock wave formation during bubble expansion leads to scaling of the axion abundance as $\Omega_\phi^{(d1)} \propto Cv^{-1+\alpha}\beta m_0\phi_0^2/(T_b^3)$, resulting in steeper mass dependence than in the standard scenario. Moreover, clear transitions are evident at $m_0 = 3H_b$ and $m_0 = \beta$, precisely corresponding to the boundaries between the different dynamical regimes classified in our theoretical framework.

In the late oscillation regime ($3H_b > m_0$, case a), both first- and second-order cases produce similar results, as predicted by our analysis in Eq. (4.2) and Eq. (4.3). This is because the axion only begins to oscillate after the phase transition has completed in both scenarios. The rapid transition regime (case (b)) shows moderate enhancement depending on the oscillation phase, α_b, as represented by the light cyan shaded region. The bubble misalignment mechanism significantly modifies the axion abundance in the intermediate regime (case (d1)), where spatial inhomogeneities from bubble nucleation play a crucial role.

4.6 Multiple Bubble Simulation

We further analysed the dynamics of axions in a more realistic setting by performing simulations involving multiple bubbles and applying periodic boundary conditions. Unlike the single-bubble approach described in previous sections, this method randomly generates multiple nucleation centres for bubbles within a cubic lattice. This allows us to investigate the effect of interactions between multiple expanding bubbles on the evolution of the axion field.

As in single-bubble simulations, the bubbles in these simulations expand at constant velocities. These velocities represent those that bubbles attain rapidly due to interactions with the surrounding plasma in a realistic phase transition, effectively bypassing the initial acceleration phase that occurs after nucleation. During physical phase transitions, bubbles initially nucleate at rest, but then rapidly accelerate to a terminal velocity, which is determined by the balance between the vacuum energy that drives expansion and the friction from cosmic plasma.

Fig. 4.11 shows the time evolution of energy in systems with different numbers of bubbles at various wall velocities. As the number of bubbles increases, the total energy of the system reaches higher values and plateaus earlier than in single-bubble simulations. This behavior aligns with our theoretical expectations, as more bubbles create more bubble walls and shock wavefronts, resulting in more opportunities for axion production and Fermi acceleration.

In Section 4.4, we established that the axion number density scales as $n_\phi \propto L^{-1}$ in the single-bubble scenario, where L represents the typical distance between bubbles. In our multiple-bubble system, we can extend this understanding by considering how the effective interbubble separation changes with bubble number. With N bubbles distributed uniformly in a cubic volume, the typical distance between bubble walls scales approximately as $L/N^{1/3}$, where L is the box size. According to our theoretical model, we would therefore expect the axion number density to scale as $n_\phi \propto N^{1/3}$.

Fig. 4.12 confirms this scaling relationship and presents the average final energy density from 100 simulations with randomly distributed multiple bubbles for different wall velocities. The data points follow the predicted $N^{1/3}$ scaling remarkably well, with velocity-dependent coefficients that align with our earlier findings on the velocity dependence of axion production. The correlation is strong, with R^2 values of 0.966, 0.985, and 0.966 for wall velocities of 0.1, 0.5, and 0.9, respectively.

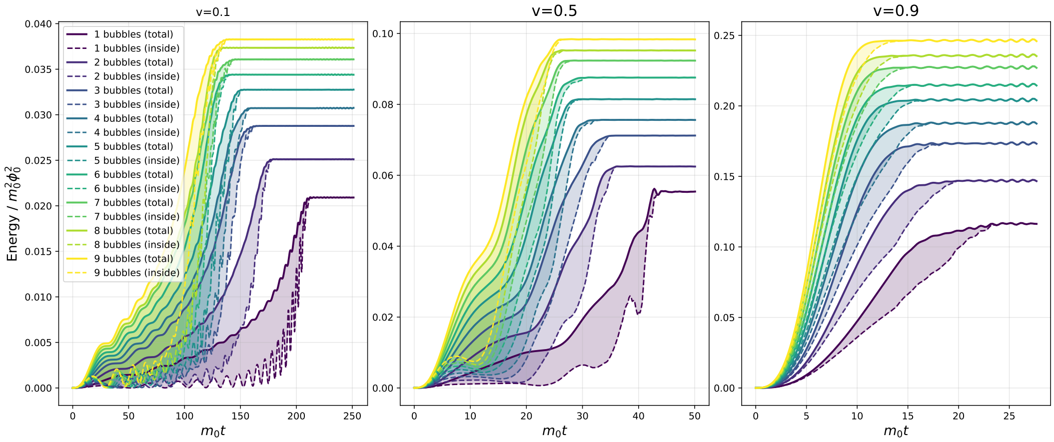

Figure 4.11: Energy evolution for different bubble wall velocities: $v = 0.1$, $v = 0.5$, and $v = 0.9$. Each plot shows the total energy and energy inside bubbles for varying numbers of bubbles. The horizontal axis represents m_0t, and the vertical axis shows the normalized energy $E/(m_0^2\phi_0^2)$.

The momentum distributions, shown in Fig. 4.13, exhibit complex dependencies on both bubble count and wall velocity. Multiple bubbles lead to broader distributions with more extended high-momentum tails, reflecting the complex multi-scattering dynamics which occurs when axion waves interact with multiple bubble walls simultaneously. This effect is particularly noticeable for lower velocities ($v = 0.1$), where the 5-bubble configuration maintains significant population at momentum values for which the 1- and 3-bubble distributions have already declined. The velocity dependence of the momentum distribution is also clearly visible across the three panels in Fig. 4.13. At $v = 0.1$ (slow walls), the distribution peaks at relatively low momenta, consistent with our earlier finding that transmitted axion momentum scales approximately as $\sqrt{v}$ for low velocities. As the velocity increases to $v = 0.5$ and $v = 0.9$, the distributions broaden and shift toward higher momenta, reflecting the more efficient energy transfer during wall collisions at higher velocities. These multi-bubble simulations provide a more realistic picture of axion production during a first-order phase transition and further validate our theoretical model of the bubble misalignment mechanism. The results confirm that both the number density and momentum distribution of axions depend strongly on the bubble nucleation rate (which determines the typical interbubble distance) and the bubble wall velocity, factors that would vary in different cosmological phase transition scenarios.

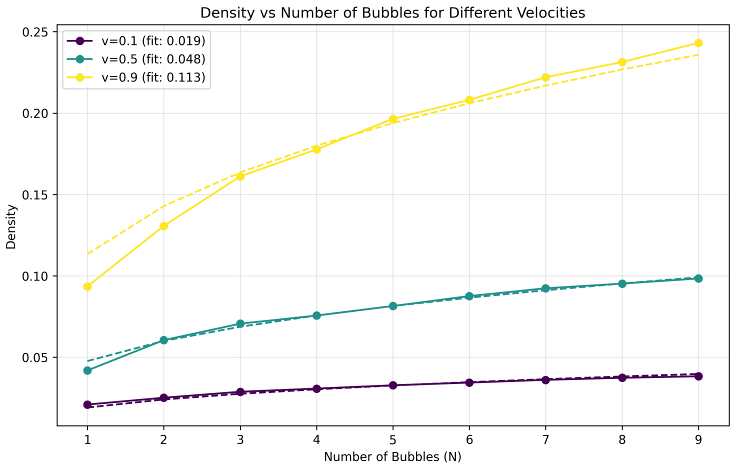

Figure 4.12: Final energy density versus number of bubbles for different wall velocities. Solid curves represent the measured density, while dashed lines show the theoretical fit to the scaling law density $= c \cdot N^{1/3}$, where c is the velocity-dependent scaling coefficient and N is the number of bubbles. The fit coefficients for each velocity are indicated in the legend.

4.7 Bubble Wall Dynamics with Axion Pressure Feedback

Having analyzed the multiple bubble system in the previous section, we now focus on a more comprehensive treatment that incorporates the pressure of axion waves on the bubble walls themselves. In our previous simulations, the bubble walls were assigned fixed velocities that remained constant throughout the evolution. This extension significantly improves the physical completeness of our model, enabling us to examine the coupled dynamics between the expanding bubble and the axion field.

The motion of a bubble wall in a FOPT is usually determined by the balance of three main forces: vacuum energy, which drives expansion; surface tension, which minimizes the bubble's surface area; and pressure, which is exerted by fields interacting with the wall. A complete equation of motion for the bubble wall can be expressed as follows [57]:

$$\gamma^3 \sigma \frac{d^2 R}{dt^2} = \Delta V - P_\phi, \tag{4.54}$$

where σ denotes the surface tension of the bubble wall, R is the bubble radius, ΔV corresponds to the vacuum energy difference that drives the expansion, and P_ϕ represents the pressure exerted by the axion field on the wall. The axion pressure term arises from the field's kinetic energy density concentrated at the wall and can be derived by considering the energy-momentum tensor of the axion field. The pressure can be approximated as [57]:

$$P_\phi = -\frac{\Delta f^2}{2} \langle \dot{\phi}^2 \rangle + \frac{\gamma^2}{2} \left(\frac{\Delta f^2}{f^2} \right) f^2 \langle \dot{\phi}^2 \rangle, \tag{4.55}$$

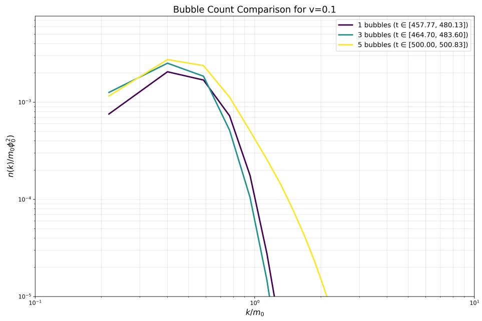

(a) $v = 0.1$

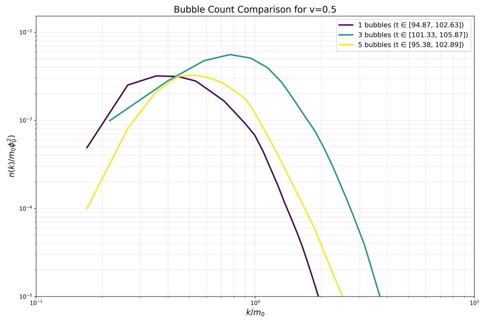

(b) $v = 0.5$

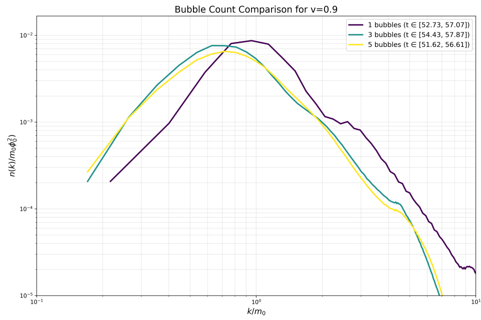

(c) $v = 0.9$

Figure 4.13: Momentum distribution $n(k)$ for different numbers of bubbles at various wall velocities. The horizontal axis represents k/m_0, and the vertical axis shows the normalized momentum distribution $n(k)/(m_0\phi_0^2)$.

where the term $\Delta f^2 = f^2 - f_{\text{inside}}^2$ represents the difference in the axion decay constant squared between the outside and inside of the bubble, and $\langle\dot{\phi}^2\rangle$ denotes the average of the squared time derivative of the axion field evaluated at the bubble wall.

To incorporate this pressure feedback mechanism into our numerical simulations, we developed a multi-step approach. At each time step, the simulation identifies grid points in the immediate vicinity of each bubble wall by calculating the distance from each grid point to the bubble center and selecting the points whose distances lie within a small tolerance of the current bubble radius. Then it computes the average squared time derivative of the axion field at these wall-adjacent points, thereby measuring the local kinetic energy density of the axion field. Using Eq. (4.55), we calculate the pressure and update the bubble wall velocity according to the differential equation:

$$\frac{dv}{dt} = \frac{\Delta V - P_\phi}{\gamma^3\sigma}, \tag{4.56}$$

In our approach, the wall velocity evolves in response to the axion field it generates, creating a feedback loop which captures the physics of the system more accurately.

Our simulations with pressure feedback reveal several important features of the bubble-axion interaction. When axion pressure feedback is included, we found that bubble walls initially accelerate to high velocities ($v \approx 1$) due to the vacuum energy difference driving the expansion, until the axion pressure becomes significant enough to slow down the walls. Fig. 4.14 illustrates this characteristic time evolution of bubble wall velocity, demonstrating a distinctive pattern of initial acceleration followed by substantial deceleration as the axion pressure builds up, eventually reaching an equilibrium velocity.

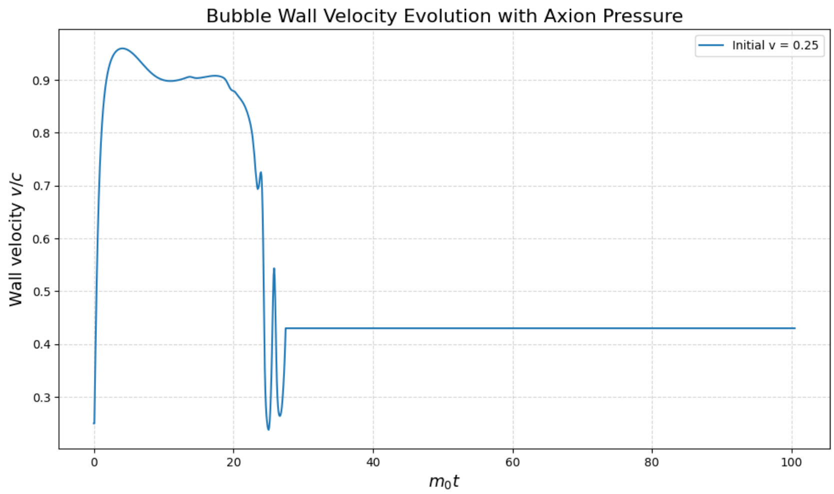

Figure 4.14: Time evolution of bubble wall velocity for different parameter sets.

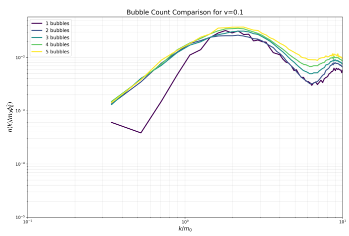

(a) $v = 0.1$

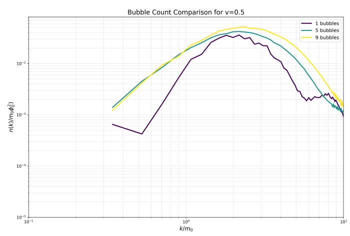

(b) $v = 0.5$

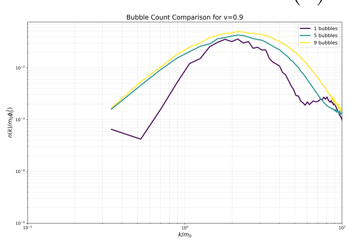

(c) $v = 0.9$

Figure 4.16: Momentum distribution $n(k)/(m_0\phi_0^2)$ versus k/m_0 for pressure-enabled simulations with different numbers of bubbles at various wall velocities. The distributions show characteristic peaks that shift to higher momenta as velocity increases, with more populated high-momentum states as bubble count increases.

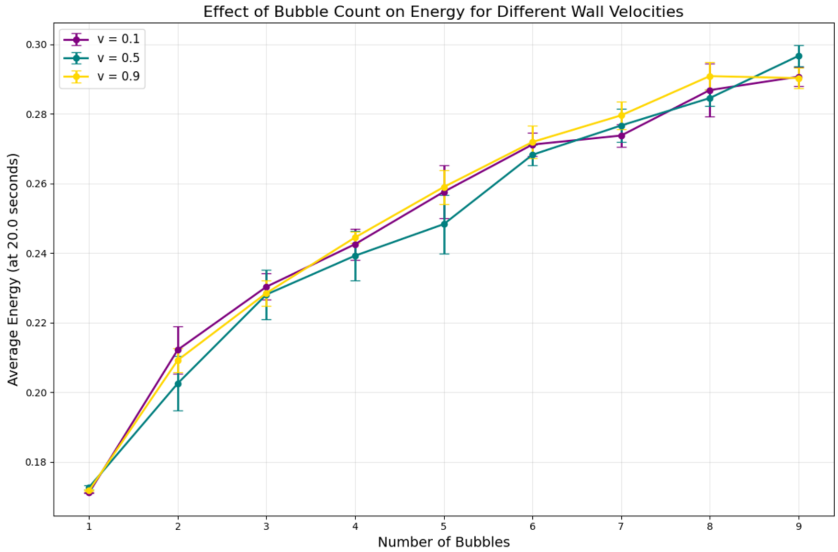

Figure 4.15: Average energy versus number of bubbles for systems with pressure feedback at a fixed time (after bubbles have filled the simulation box). Unlike the constant velocity case, all velocity variants reach similar final energy values due to the initial acceleration spike that equalizes bubble filling times.

This dynamic behavior fundamentally differs from the constant-velocity approximation used in previous sections, where we assumed fixed velocities throughout the simulation. Fig. 4.15 presents the relationship between the number of bubbles and the average energy at a fixed time for different initial wall velocities. Unlike Fig. 4.12, in pressure-enabled simulations, all velocity variants reach similar final energy values due to the initial acceleration spike that equalizes bubble filling times, effectively removing the velocity dependence seen in constant-velocity models.

We also analyzed the momentum distributions in pressure-enabled simulations for different wall velocities. Fig. 4.16 shows how the bubble count and wall velocity affect the energy transfer to axion waves in pressure-feedback systems. The distributions reveal characteristic peaks that shift to higher momenta as velocity increases, with more populated high-momentum states as bubble count increases.

The initial acceleration phase can be attributed to the vacuum energy difference dominating initially, while subsequent deceleration occurs as the axion field builds up sufficient energy near the wall to exert substantial pressure. This coupled dynamics between the axion field and bubble walls provides a more physically complete description of the bubble misalignment mechanism.

Chapter 5

Conclusions and Prospectives

In this thesis, we study the dynamics of the axion across first-order phase transitions (FOPTs) and investigate the bubble misalignment mechanism. First, we reviewed the evidence for dark matter at several scales and explored various production mechanisms, including thermal and non-thermal relics. Next, to understand phase transitions in the early universe, we discussed the key theoretical framework of quantum field theory at finite temperature, paying particular attention to the processes of bubble nucleation and expansion that characterize FOPTs. We then introduced the axion as a potential solution to the strong CP problem, examining its properties, interactions and production processes, including the conventional misalignment mechanism. While conventional axion production mechanisms such as the misalignment mechanism are well-established in the literature, the specific effects of FOPTs on axion production represent an area of ongoing research. The bubble misalignment mechanism, in particular, adds to our understanding of possible axion production channels in the early universe.

Following the analysis in Lee et al. [2], axion dynamics during FOPTs can be classified into four distinct regimes determined by the hierarchy between the Hubble parameter (H_b), axion masses inside and outside bubbles (m_0 and m_b), and the phase transition rate (β). The late oscillation regime, characterized by $3H_b > m_0$, features axions that begin oscillating only after the phase transition is complete, resembling the conventional misalignment mechanism with minimal modification. In the rapid transition regime, where $\beta > m_0 > m_b, 3H_b$, the phase transition proceeds more rapidly than any other relevant timescale, causing a nearly instantaneous change in the axion mass. This can enhance the axion abundance by up to a factor of $(m_0/m_b)^2$ depending on the oscillation phase at transition time.

The early oscillation regime occurs when $m_b > \beta$, meaning axions are already oscillating before the phase transition. In this scenario, we observed that axion waves undergo Fermi acceleration upon reflection from bubble walls, gaining energy with each reflection until they acquire sufficient momentum to penetrate the bubbles. Finally, the intermediate regime, defined by $m_0 > \beta > m_b, 3H_b$, features the formation of axion shock waves around expanding bubbles, with the axion number density scaling inversely with the typical distance between bubbles.

Our numerical simulations have verified these theoretical predictions and revealed several important physical insights. In our simulation setup, we initially modeled bubbles with constant velocities, representing the terminal velocities that bubble walls would rapidly reach due to interactions with the surrounding plasma in a realistic phase transition. While bubbles physically nucleate at rest, this simplification allows us to focus on the steady-state dynamics. The numerical simulations confirmed that axion waves undergo Fermi acceleration when reflecting off the bubble walls, eventually gaining sufficient energy to penetrate the bubbles. This mechanism preserves axion number while modifying the momentum distribution. The final energy density depends on both bubble wall velocity and mass ratio, with distinct scaling behaviors in different parameter regions. Our multi-bubble simulations verified the axion number density scaling with bubble number as $N^{1/3}$, with correlation coefficients $R^2 > 0.96$ across different wall velocities. This scaling relationship follows directly from the theoretical prediction that axion production occurs primarily at bubble walls, with typical inter-bubble distance scaling as $N^{-1/3}$. The numerical results identified distinct velocity-dependent scaling regimes for the axion number density, with $n_\phi \propto v^{0.4}$ for $v \lesssim 0.4$ and $n_\phi \propto v^{0.8}$ for $v \gtrsim 0.4$.

We also considered the case where bubble dynamics is affected by the pressure caused by the axions. While in physical reality bubbles nucleate at rest, they quickly accelerate due to the vacuum energy difference driving the phase transition. In our pressure-enabled simulations, we found that the walls initially reach high velocities ($v \approx 1$) until axion pressure becomes significant and slows down the walls. This dynamic evolution differs from constant-velocity simulations, in which a fixed wall speed was imposed to represent the terminal velocity that the bubbles would reach through interaction with the surrounding plasma. Incorporating axion pressure feedback allows us to examine a different physical scenario, in which the velocity of the bubble wall evolves dynamically and is determined by the interplay between driving vacuum energy and opposing axion pressure.

Compared to standard scenarios, the bubble misalignment mechanism alters both the abundance and momentum distribution of axion dark matter. As shown in Fig. 4.10, for certain parameter regimes, particularly in the intermediate regime (case d1), axion production is significantly enhanced compared to second-order phase transitions. This enhancement affects the viable parameter space of axion models across different mass ranges. The spatial inhomogeneities resulting from this mechanism could lead to formation of axion miniclusters and produce other observable signatures.

The simulations used in this work have certain limitations. The axion potential was approximated as $V = m^2\phi^2$ instead of the full cosine form, which is valid for small field values but excludes anharmonic effects. Future work could use the full nonlinear potential and explore wider ranges of wall velocities and mass ratios. Higher-resolution simulations would also provide more insight into the momentum distribution, especially for cases where pressure is enabled.

This work enhances understanding of axion production mechanisms during first-order phase transitions. The findings have implications for the phenomenology of axion dark matter, particularly with regard to abundance estimates and momentum distributions in cosmological scenarios involving phase transitions.

Appendix A

Foundations of Modern Cosmology

A.1 The Cosmological Principle and FLRW metric

Modern cosmology is built upon the Cosmological Principle, which states that the Universe is homogeneous and isotropic on large scales (> 100 Mpc). Although these properties clearly do not hold on small scales, where we observe structures like galaxies and clusters, observations support these assumptions when averaged over sufficiently large volumes. These symmetry requirements uniquely determine the form of the metric describing spacetime, known as the Friedmann-Lemaître-Robertson-Walker (FLRW) metric:

$$ds^2 = dt^2 - a^2(t)\left[\frac{dr^2}{1-kr^2} + r^2(d\theta^2 + \sin^2\theta d\phi^2)\right], \tag{A.1}$$

where $a(t)$ is the scale factor describing the expansion of space, and k is the spatial curvature parameter. The coordinates (r, θ, ϕ) are comoving coordinates that remain fixed for observers moving with the cosmic expansion. The curvature parameter k can take three values: $k = +1$ corresponds to a closed universe with positive curvature, $k = 0$ to a flat universe, and $k = -1$ to an open universe with negative curvature. The scale factor $a(t)$ is normalized to unity at the present time, $a(t_0) = 1$. The expansion rate of the universe is characterized by the Hubble parameter $H(t)$, defined as $H(t) = \frac{\dot{a}}{a}$, where the dot denotes differentiation with respect to cosmic time t. The current value of the Hubble parameter, H_0, is one of the most important parameters in cosmology, though its precise value remains subject to some tension between different measurement methods.

A.2 Einstein Equations and Energy-Momentum Tensor

The dynamics of the Universe are governed by Einstein's field equations:

$$G_{\mu\nu} = 8\pi G T_{\mu\nu}, \tag{A.2}$$

where $G_{\mu\nu}$ is the Einstein tensor derived from the metric and its derivatives, and $T_{\mu\nu}$ is the energy-momentum tensor. For cosmological purposes, we can model the content of the universe as a perfect fluid, which is characterized by its energy density ρ and pressure p in its rest frame. The energy-momentum tensor for a perfect fluid takes the form:

$$T_{\mu\nu} = (\rho + p)u_\mu u_\nu - p g_{\mu\nu}, \tag{A.3}$$

where u_μ is the 4-velocity of the fluid and $g_{\mu\nu}$ is the metric tensor. The 4-velocity satisfies the normalization condition $u^\mu u_\mu = 1$. The relationship between pressure and density is specified by the equation of state $p = w\rho$, where w is the equation of state parameter. For non-relativistic matter (also called dust), the pressure is negligible compared to the energy density, giving $w = 0$. Radiation and other relativistic matter have $w = 1/3$, which can be derived from the radiation stress-energy tensor. The cosmological constant, or vacuum energy, has $w = -1$, which follows from its interpretation as a constant energy density in vacuum.

A.3 Friedmann Equations

Applying Einstein's equations to the FLRW metric yields the Friedmann equations. The time-time component gives the first Friedmann equation:

$$H^2 = \left(\frac{\dot{a}}{a}\right)^2 = \frac{8\pi G}{3}\rho - \frac{k}{a^2}, \tag{A.4}$$

while the space-space components, after combining with the first equation, give the second Friedmann equation:

$$\frac{\ddot{a}}{a} = -\frac{4\pi G}{3}(\rho + 3p). \tag{A.5}$$

From the conservation of energy-momentum, expressed as the covariant divergence $\nabla_\mu T^{\mu\nu} = 0$, we obtain an additional equation:

$$\dot{\rho} + 3H(\rho + p) = 0. \tag{A.6}$$

This continuity equation describes how the density of each component evolves with the expansion. For a component with equation of state parameter w, this equation can be integrated to give:

$$\rho \propto a^{-3(1+w)}. \tag{A.7}$$

A.4 Solutions for Different Cosmic Eras

The evolution of the universe is determined by the dominant energy component at any given time. For a universe dominated by a single component with equation of state w, we can solve the Friedmann equations to find the time dependence of the scale factor and other cosmological parameters. During matter domination ($w = 0$), the density scales to $\rho \propto a^{-3}$, reflecting the dilution of matter as space expands. The scale factor evolves as:

$$a(t) \propto t^{2/3}, \quad H(t) = \frac{2}{3t}. \tag{A.8}$$

For radiation domination ($w = 1/3$), the additional factor of a^{-1} in the density scaling comes from the redshifting of photon energies, giving $\rho \propto a^{-4}$. The solutions are:

$$a(t) \propto t^{1/2}, \quad H(t) = \frac{1}{2t}. \tag{A.9}$$

In the case of dark energy domination ($w = -1$), the density remains constant as the universe expands, leading to exponential expansion:

$$a(t) \propto e^{Ht}, \quad H = \text{constant}. \tag{A.10}$$

A.5 Density Parameters and Critical Density

The critical density $\rho_c = 3H^2/8\pi G$ represents the total energy density required for a flat universe ($k = 0$). It is convenient to express the energy content of the universe in terms of density parameters $\Omega_i = \rho_i/\rho_c$ for each component i. The first Friedmann equation can then be written as:

$$\sum \Omega_i + \Omega_k = 1, \tag{A.11}$$

where $\Omega_k = -k/(a^2H^2)$ represents the curvature contribution. The density parameters evolve with time according to:

$$\Omega_i(a) = \Omega_{i,0}\frac{a^{-3(1+w_i)}}{(H/H_0)^2}, \tag{A.12}$$

where $\Omega_{i,0}$ represents the present-day value. Current observations from the Planck satellite indicate that we live in a spatially flat universe dominated by dark energy ($\Omega_\Lambda \approx 0.68$) and matter ($\Omega_m \approx 0.32$), with negligible curvature ($|\Omega_k| < 0.01$).

Appendix B

Full Derivation of Axion Energy Density

In this appendix, we present detailed derivations of the axion energy density expressions for the various regimes discussed in Chapter 4. We begin with the fundamental equations governing axion dynamics and systematically derive the abundance in each scenario.

B.1 Fundamental Equations and Conventions

We start with the equation of motion for the axion field in an expanding universe:

$$\ddot{\phi} + 3H\dot{\phi} + m_\phi^2(T)\phi = 0, \tag{B.1}$$

where H is the Hubble parameter, and $m_\phi(T)$ is the temperature-dependent axion mass. We assume that the axion mass has the following temperature dependence:

$$m_\phi(T) = \begin{cases} m_0 & (T < \Lambda) \\ m_0 \left(\frac{T}{\Lambda}\right)^{-p/2} & (T \geq \Lambda), \end{cases} \tag{B.2}$$

where m_0 is the zero-temperature axion mass, Λ is a characteristic scale (approximately the QCD scale for QCD axions), and $p \approx 8$ for the QCD axion.

In a radiation-dominated universe, the Hubble parameter is:

$$H(T) = \sqrt{\frac{\pi^2 g_*}{90}} \frac{T^2}{M_{Pl}}, \tag{B.3}$$

where g_* is the effective number of relativistic degrees of freedom and M_{Pl} is the reduced Planck mass. The axion energy density can be calculated as:

$$\rho_\phi = \frac{1}{2}\dot{\phi}^2 + \frac{1}{2}m_\phi^2\phi^2. \tag{B.4}$$

To relate the present-day axion abundance to the cosmological parameters, we need to account for the entropy conservation. The entropy density is:

$$s = \frac{2\pi^2}{45} g_{*s} T^3, \tag{B.5}$$

where g_{*s} is the effective number of relativistic degrees of freedom for entropy. The axion-to-entropy ratio $Y_\phi = n_\phi / s$ remains constant as the universe expands (assuming no entropy production). The present-day axion density parameter is:

$$\Omega_\phi h^2 = \frac{\rho_\phi(t_0) h^2}{\rho_{c,0}} = \frac{m_\phi s_0 Y_\phi h^2}{\rho_{c,0}}, \tag{B.6}$$

where $\rho_{c,0} \approx 1.05 \times 10^{-5} h^2$ GeV/cm^3 is the critical density today [54].

B.2 Axion Abundance in Different Dynamical Regimes

B.2.1 Case (a): Late Oscillation Regime ($3H_b > m_0$)

In this regime, the axion begins oscillating only after the first-order phase transition (FOPT) is completed. The oscillation condition is:

$$m_0 \approx 3H(T_{osc}). \tag{B.7}$$

Solving for the oscillation temperature:

$$T_{osc,(a)} \approx \left(\frac{10}{\pi^2 g_{*,osc}} \right)^{1/4} \sqrt{\frac{M_{Pl}}{m_0}}. \tag{B.8}$$

The axion energy density at the onset of oscillations is:

$$\rho_\phi(T_{osc}) = \frac{1}{2} m_0^2 \phi_0^2. \tag{B.9}$$

To calculate the present-day abundance, we use the relation $\frac{\rho_\phi(T_0)}{\rho_\phi(T_{osc})} = \frac{s(T_0)}{s(T_{osc})}$ which gives:

$$\rho_\phi(T_0) = \rho_\phi(T_{osc}) \frac{s(T_0)}{s(T_{osc})} = \frac{1}{2} m_0^2 \phi_0^2 \frac{s(T_0)}{s(T_{osc})}. \tag{B.10}$$

The entropy density ratio is:

$$\frac{s(T_0)}{s(T_{osc})} = \frac{g_{*s,0}}{g_{*s,osc}} \left(\frac{T_0}{T_{osc}} \right)^3. \tag{B.11}$$

Substituting the expression for T_{osc}:

$$\begin{aligned} \rho_\phi(T_0) &= \frac{1}{2} m_0^2 \phi_0^2 \frac{g_{*s,0}}{g_{*s,osc}} \left(\frac{T_0}{\left(\frac{10}{\pi^2 g_{*,osc}} \right)^{1/4} \sqrt{\frac{M_{Pl}}{m_0}}} \right)^3 \\ &= \frac{1}{2} m_0^2 \phi_0^2 \frac{g_{*s,0}}{g_{*s,osc}} \left(\frac{\pi^2 g_{*,osc}}{10} \right)^{3/4} \frac{T_0^3 m_0^{3/2}}{M_{Pl}^{3/2}}. \end{aligned} \tag{B.12}$$

Converting to the density parameter:

$$\begin{aligned}\frac{\rho_\phi(T_0)}{s(T_0)} &= \frac{1}{2}m_0^2\phi_0^2\frac{1}{s(T_{osc})}\left(\frac{\pi^2 g_{*,osc}}{10}\right)^{3/4}\frac{m_0^{3/2}}{M_{Pl}^{3/2}} \\ &= \frac{1}{2}m_0^2\phi_0^2\frac{45}{2\pi^2 g_{*s,osc}T_{osc}^3}\left(\frac{\pi^2 g_{*,osc}}{10}\right)^{3/4}\frac{m_0^{3/2}}{M_{Pl}^{3/2}},\end{aligned} \tag{B.13}$$

and substituting for T_{osc}:

$$\frac{\rho_\phi(T_0)}{s(T_0)} = \frac{45}{4\pi^2 g_{*s,osc}}\left(\frac{\pi^2 g_{*,osc}}{10}\right)^{3/4}\frac{m_0^{1/2}\phi_0^2}{M_{Pl}^{3/2}}. \tag{B.14}$$

This gives us the final result for case (a):

$$\rho_\phi^{(a)}/s = \frac{45}{4\pi^2 g_{*s,osc}}\left(\frac{\pi^2 g_{*,osc}}{10}\right)^{3/4}\frac{m_0^{1/2}\phi_0^2}{M_{Pl}^{3/2}}. \tag{B.15}$$

B.2.2 Case (b): Rapid Transition Regime ($\beta > m_0 > m_b, 3H_b$)

Case (b1): $m_b < 3H_b$

In this case, the axion has not started oscillating before the FOPT. After the transition, it immediately begins oscillating with mass m_0. The axion energy density just after the transition is:

$$\rho_\phi(T_b) = \frac{1}{2}m_0^2\phi_0^2. \tag{B.16}$$

The ratio of this energy density to the entropy density at the nucleation temperature T_b is:

$$\begin{aligned}\frac{\rho_\phi(T_b)}{s(T_b)} &= \frac{1}{2}m_0^2\phi_0^2\frac{45}{2\pi^2 g_{*s,b}T_b^3} \\ &= \frac{45m_0^2\phi_0^2}{4\pi^2 g_{*s,b}T_b^3}.\end{aligned} \tag{B.17}$$

This gives us the final result for case (b1):

$$\rho_\phi^{(b1)}/s = \frac{45m_0^2\phi_0^2}{4\pi^2 g_{*s,b}T_b^3}. \tag{B.18}$$

Case (b2): $m_b > 3H_b$

In this case, the axion has already started oscillating before the FOPT. The oscillation temperature for the pre-FOPT axion is:

$$m_b(T_{osc,(b2)}) \approx 3H(T_{osc,(b2)}). \tag{B.19}$$

Substituting the mass dependence:

$$m_0 \left(\frac{T_{osc,(b2)}}{\Lambda} \right)^{-p/2} \approx 3 \sqrt{\frac{\pi^2 g_*}{90}} \frac{T_{osc,(b2)}^2}{M_{Pl}}, \tag{B.20}$$

then solving for $T_{osc,(b2)}$:

$$T_{osc,(b2)} \approx \left(\frac{10}{\pi^2 g_{*,osc}} \right)^{1/(4+p)} \left(\frac{m_0 M_{Pl}}{\Lambda^{p/2}} \right)^{2/(4+p)}. \tag{B.21}$$

The axion field amplitude at the bubble nucleation temperature T_b is:

$$\bar{\phi}(T_b) = \phi_0 \left(\frac{T_b}{T_{osc,(b2)}} \right)^{(p+6)/4}. \tag{B.22}$$

Just after the phase transition, the axion field value and its derivative are:

$$\phi \approx \bar{\phi}_b \sin \alpha_b, \quad \dot{\phi} \approx m_b \bar{\phi}_b \cos \alpha_b, \tag{B.23}$$

where α_b is the phase of oscillation at the transition. The energy density just after the transition is:

$$\rho_\phi(T_b) = \frac{\bar{\phi}_b^2}{2} (m_b^2 \cos^2 \alpha_b + m_0^2 \sin^2 \alpha_b). \tag{B.24}$$

The corresponding energy density to entropy ratio is:

$$\frac{\rho_\phi(T_b)}{s(T_b)} = \frac{\bar{\phi}_b^2}{2} (m_b^2 \cos^2 \alpha_b + m_0^2 \sin^2 \alpha_b) \frac{45}{2\pi^2 g_{*s,b} T_b^3}. \tag{B.25}$$

Substituting for $\bar{\phi}_b$ and simplifying:

$$\begin{aligned} \frac{\rho_\phi(T_b)}{s(T_b)} &= \phi_0^2 \left(\frac{T_b}{T_{osc,(b2)}} \right)^{(p+6)/2} \frac{(m_b^2 \cos^2 \alpha_b + m_0^2 \sin^2 \alpha_b)}{2} \frac{45}{2\pi^2 g_{*s,b} T_b^3} \\ &= \frac{45 \phi_0^2 (m_b^2 \cos^2 \alpha_b + m_0^2 \sin^2 \alpha_b)}{4\pi^2 g_{*s,b} T_b^3} \left(\frac{T_b}{T_{osc,(b2)}} \right)^{(p+6)/2}. \end{aligned} \tag{B.26}$$

Further substituting the expression for $T_{osc,(b2)}$:

$$\rho_\phi^{(b2)}/s = \frac{45}{4\pi^2 g_{*s,osc}} \left(\frac{\pi^2 g_{*,osc}}{10} \right)^{(p+6)/2(p+4)} \frac{\phi_0^2}{(m_b^{p+6} M_{Pl}^{p+6} T_b^p)^{1/(p+4)}} (m_b^2 \cos^2 \alpha_b + m_0^2 \sin^2 \alpha_b). \tag{B.27}$$

This is the final result for case (b2).

B.2.3 Case (c): Early Oscillation Regime ($m_b > \beta$)

In this case, the axion number is conserved due to reflection and transmission processes at bubble walls. The axion abundance remains the same as in a second-order phase transition:

$$\rho_\phi^{(c)}/s = \frac{45}{4\pi^2 g_{*s,osc}} \left(\frac{\pi^2 g_{*,osc}}{10}\right)^{(p+6)/2(p+4)} \frac{m_0 \phi_0^2}{(m_b^2 M_{Pl}^{p+6} T_b^p)^{1/(p+4)}}. \tag{B.28}$$

The derivation follows the same steps as for case (b2), but with an additional factor of m_0/m_b to account for the increase in axion mass after the phase transition while preserving axion number.

B.2.4 Case (d): Intermediate Regime ($m_0 > \beta > m_b, 3H_b$)

Case (d1): $m_b < 3H_b$

Based on the numerical simulations described in Section 4.5, the axion number density just after the FOPT is:

$$n_\phi(T_b) \approx C v^{-1+\alpha} \beta \phi_0^2, \tag{B.29}$$

where C and α are parameters determined from the simulations. The energy density is:

$$\rho_\phi(T_b) = m_0 n_\phi(T_b) \approx C v^{-1+\alpha} \beta m_0 \phi_0^2. \tag{B.30}$$

The corresponding energy density to entropy ratio is:

$$\begin{aligned} \frac{\rho_\phi(T_b)}{s(T_b)} &= \frac{C v^{-1+\alpha} \beta m_0 \phi_0^2}{s(T_b)} = \frac{C v^{-1+\alpha} \beta m_0 \phi_0^2}{2\pi^2 g_{*s,b} T_b^3/45} \\ &= \frac{45 C v^{-1+\alpha} \beta m_0 \phi_0^2}{2\pi^2 g_{*s,b} T_b^3}. \end{aligned} \tag{B.31}$$

This gives us the final result for case (d1):

$$\rho_\phi^{(d1)}/s = \frac{45 C v^{-1+\alpha} \beta m_0 \phi_0^2}{2\pi^2 g_{*s,b} T_b^3}. \tag{B.32}$$

Case (d2-1): $m_b > 3H_b$ **with** $\phi = \phi_b$, $\dot{\phi} = 0$ **at FOPT**

If the axion field is at its maximum value at the transition, the dynamics follow case (d1), but we need to account for the evolution of the axion field before the transition. The oscillation amplitude at T_b is:

$$\bar{\phi}(T_b) = \phi_0 \left(\frac{T_b}{T_{osc,(b2)}}\right)^{(p+6)/4}. \tag{B.33}$$

The axion number density just after the FOPT is:

$$n_\phi(T_b) \approx Cv^{-1+\alpha}\beta\bar{\phi}^2(T_b) = Cv^{-1+\alpha}\beta\phi_0^2\left(\frac{T_b}{T_{osc,(b2)}}\right)^{(p+6)/2}. \tag{B.34}$$

The energy density is:

$$\rho_\phi(T_b) = m_0 n_\phi(T_b) \approx Cv^{-1+\alpha}\beta m_0\phi_0^2\left(\frac{T_b}{T_{osc,(b2)}}\right)^{(p+6)/2}. \tag{B.35}$$

The corresponding energy density to entropy ratio is:

$$\begin{aligned}\frac{\rho_\phi(T_b)}{s(T_b)} &= \frac{Cv^{-1+\alpha}\beta m_0\phi_0^2\left(\frac{T_b}{T_{osc,(b2)}}\right)^{(p+6)/2}}{2\pi^2 g_{*s,b}T_b^3/45}\\ &= \frac{45Cv^{-1+\alpha}\beta m_0\phi_0^2}{2\pi^2 g_{*s,b}T_b^3}\left(\frac{T_b}{T_{osc,(b2)}}\right)^{(p+6)/2}.\end{aligned} \tag{B.36}$$

Substituting the expression for $T_{osc,(b2)}$:

$$\rho_\phi^{(d2-1)}/s = \frac{45Cv^{-1+\alpha}}{2\pi^2 g_{*s,b}}\left(\frac{\pi^2 g_{*,osc}}{10}\right)^{(p+6)/2(p+4)}\frac{\beta m_0\phi_0^2}{(m_b^{p+6}M_{Pl}^{p+6}T_b^p)^{1/(p+4)}}. \tag{B.37}$$

Case (d2-2): $m_b > 3H_b$ with $\phi = 0$ at FOPT

If the axion field is at zero at the transition, the bubble formation does not affect the axion field, and the result matches case (b2) with $\sin\alpha_b = 0$:

$$\rho_\phi^{(d2-2)}/s = \frac{45}{4\pi^2 g_{*s,osc}}\left(\frac{\pi^2 g_{*,osc}}{10}\right)^{(p+6)/2(p+4)}\frac{m_b^2\phi_0^2}{(m_b^{p+6}M_{Pl}^{p+6}T_b^p)^{1/(p+4)}}. \tag{B.38}$$

B.3 Ratio of Axion Abundance

To quantify the enhancement or suppression of axion abundance due to the bubble misalignment mechanism, we compare the results derived above with the standard second-order phase transition scenario. The axion abundance in a second-order phase transition is:

$$\rho_\phi^{(2nd)}/s = \frac{45}{4\pi^2 g_{*s,osc}}\left(\frac{\pi^2 g_{*,osc}}{10}\right)^{(p+6)/2(p+4)}\frac{m_0\phi_0^2}{(m_b^2 M_{Pl}^{p+6}T_b^p)^{1/(p+4)}}. \tag{B.39}$$

For case (c), the ratio is unity since the axion number is conserved:

$$\frac{\rho_\phi^{(c)}}{\rho_\phi^{(2nd)}} = 1. \tag{B.40}$$

For case (b1), the ratio is:

$$\frac{\rho_\phi^{(b1)}}{\rho_\phi^{(2nd)}} = \frac{\frac{45 m_0^2 \phi_0^2}{4\pi^2 g_{*s,b} T_b^3}}{\frac{45}{4\pi^2 g_{*s,osc}} \left(\frac{\pi^2 g_{*,osc}}{10}\right)^{(p+6)/2(p+4)} \frac{m_0 \phi_0^2}{(m_b^2 M_{Pl}^{p+6} T_b^p)^{1/(p+4)}}}. \tag{B.41}$$

Assuming $g_{*s,b} \approx g_{*s,osc}$ for simplicity:

$$\begin{aligned}\frac{\rho_\phi^{(b1)}}{\rho_\phi^{(2nd)}} &= \frac{m_0^2 \phi_0^2 T_b^{-3}}{m_0 \phi_0^2 (m_b^2)^{-1/(p+4)} (M_{Pl}^{p+6} T_b^p)^{-1/(p+4)} \left(\frac{\pi^2 g_{*,osc}}{10}\right)^{(p+6)/2(p+4)}} \\ &= \frac{m_0}{m_0} \frac{T_b^{-3}}{(m_b^2)^{-1/(p+4)} (M_{Pl}^{p+6} T_b^p)^{-1/(p+4)} \left(\frac{\pi^2 g_{*,osc}}{10}\right)^{(p+6)/2(p+4)}} \\ &= \frac{(m_b^2)^{1/(p+4)} (M_{Pl}^{p+6})^{1/(p+4)} (T_b^p)^{1/(p+4)} \left(\frac{\pi^2 g_{*,osc}}{10}\right)^{-(p+6)/2(p+4)}}{T_b^3}. \end{aligned} \tag{B.42}$$

Using $T_{osc}^{(p+6)/2} \approx (T_b)^3 (m_b/m_0)^{6/p}$, we get:

$$\frac{\rho_\phi^{(b1)}}{\rho_\phi^{(2nd)}} = \left(\frac{m_b}{m_0}\right)^{6/p} \left(\frac{T_{osc}}{T_b}\right)^{(p+6)/2}. \tag{B.43}$$

For case (d1), the ratio becomes:

$$\frac{\rho_\phi^{(d1)}}{\rho_\phi^{(2nd)}} = \frac{\frac{45 C v^{-1+\alpha} \beta m_0 \phi_0^2}{2\pi^2 g_{*s,b} T_b^3}}{\frac{45}{4\pi^2 g_{*s,osc}} \left(\frac{\pi^2 g_{*,osc}}{10}\right)^{(p+6)/2(p+4)} \frac{m_0 \phi_0^2}{(m_b^2 M_{Pl}^{p+6} T_b^p)^{1/(p+4)}}}. \tag{B.44}$$

After simplification and using the relation $\beta \approx H_b T_b / H(T_{osc})$:

$$\frac{\rho_\phi^{(d1)}}{\rho_\phi^{(2nd)}} = C v^{-1+\alpha} \frac{\beta}{H_b} \frac{T_b}{T_{osc}} \left(\frac{m_b}{m_0}\right)^{(4+p)/p}. \tag{B.45}$$

These ratios illustrate how different dynamical regimes can significantly enhance or suppress the axion abundance relative to the standard scenario. The bubble misalignment mechanism thus provides a rich phenomenology for axion dark matter production in the early universe.

Bibliography

[1] S. Nakagawa et al. Axion dark matter from first-order phase transition, and very high energy photons from grb 221009a. *Physics Letters B*, 839:137824, 2023.

[2] J. Lee et al. Bubble misalignment mechanism for axions. *Journal of Cosmology and Astroparticle Physics*, 2024(05):122, 2024.

[3] M. Persic et al. The universal rotation curve of spiral galaxies—i. the dark matter connection. *Monthly Notices of the Royal Astronomical Society*, 281(1):27–47, 1996.

[4] K. Begeman et al. Extended rotation curves of spiral galaxies: Dark haloes and modified dynamics. *Monthly Notices of the Royal Astronomical Society*, 249(3):523–537, 1991.

[5] M. Cirelli et al. Dark matter, 2024.

[6] D. Clowe et al. A direct empirical proof of the existence of dark matter. *The Astrophysical Journal*, 648(2):L109, 2006.

[7] A. Arbey and F. Mahmoudi. Dark matter and the early universe: a review. *Progress in Particle and Nuclear Physics*, 119:103865, 2021.

[8] S. Dodelson and F. Schmidt. *Modern cosmology.* Academic press, 2020.

[9] E. W. Kolb et al. The early universe, 1991.

[10] L. J. Hall et al. Freeze-in production of fimp dark matter. *Journal of High Energy Physics*, 2010(3):1–33, 2010.

[11] E. G. Ferreira. Ultra-light dark matter. *The Astronomy and Astrophysics Review*, 29:1–186, 2021.

[12] J. Aalbers et al. Dark matter search results from 4.2 tonne-years of exposure of the lux-zeplin (lz) experiment, 2024.

[13] E. Aprile et al. First dark matter search with nuclear recoils from the xenonnt experiment. *Physical Review Letters*, 131(4), July 2023.

[14] Y. Meng et al. Dark matter search results from the pandax-4t commissioning run. *Physical Review Letters*, 127(26), December 2021.

[15] M. Shaposhnikov. Baryon asymmetry of the universe in standard electroweak theory. *Nuclear Physics B*, 287:757–775, 1987.

[16] E. Witten. Cosmic separation of phases. *Physical Review D*, 30(2):272, 1984.

[17] C. Hogan. Gravitational radiation from cosmological phase transitions. *Monthly Notices of the Royal Astronomical Society*, 218(4):629–636, 1986.

[18] L. Dolan and R. Jackiw. Symmetry behavior at finite temperature. *Physical Review D*, 9(12):3320, 1974.

[19] M. Hindmarsh et al. Phase transitions in the early universe. *SciPost Physics Lecture Notes*, pp. 024, 2021.

[20] D. Croon. Tasi lectures on phase transitions, baryogenesis, and gravitational waves. *arXiv preprint arXiv:2307.00068*, 2023.

[21] M. E. A. Vanvlasselaer et al. Dynamics of phase transitions in the early universe and cosmological consequences. 2022.

[22] L.-B. Chen et al. Higgs boson pair production at n3 lo qcd. *arXiv preprint arXiv:2011.04265*, 2020.

[23] S. Coleman. Fate of the false vacuum: Semiclassical theory. *Physical Review D*, 15(10):2929, 1977.

[24] C. G. Callan Jr and S. Coleman. Fate of the false vacuum. ii. first quantum corrections. *Physical Review D*, 16(6):1762, 1977.

[25] A. Andreassen et al. Direct approach to quantum tunneling. *Physical Review Letters*, 117(23):231601, 2016.

[26] A. Andreassen et al. Precision decay rate calculations in quantum field theory. *Physical Review D*, 95(8):085011, 2017.

[27] R.-G. Cai and S.-J. Wang. Effective picture of bubble expansion. *Journal of Cosmology and Astroparticle Physics*, 2021(03):096, 2021.

[28] C. Baker et al. Improved experimental limit on the electric dipole moment of the neutron. *Physical review letters*, 97(13):131801, 2006.

[29] M. S. Turner. Axions from sn1987a. *Physical Review Letters*, 60(18):1797, 1988.

[30] J. Isern et al. Axions and the cooling of white dwarf stars. *The Astrophysical Journal*, 682(2):L109, 2008.

[31] C. A. O'Hare. Cosmology of axion dark matter. *arXiv preprint arXiv:2403.17697*, 2024.

[32] D. J. Marsh. Axion cosmology. *Physics Reports*, 643:1–79, 2016.

[33] B. Berenji. Axion gamma-ray signatures from quark matter in neutron stars. *arXiv preprint arXiv:2004.08722*, 2020.

[34] D. J. Gross et al. Qcd and instantons at finite temperature. *Reviews of Modern Physics*, 53(1):43, 1981.

[35] O. Wantz and E. Shellard. Axion cosmology revisited. *Physical Review D—Particles, Fields, Gravitation, and Cosmology*, 82(12):123508, 2010.

[36] G. G. Di Cortona et al. The qcd axion, precisely. *Journal of High Energy Physics*, 2016(1):1–37, 2016.

[37] D. P. Bennett and F. R. Bouchet. High-resolution simulations of cosmic-string evolution. i. network evolution. *Physical Review D*, 41(8):2408, 1990.

[38] B. Allen and E. Shellard. Cosmic-string evolution: A numerical simulation. *Physical review letters*, 64(2):119, 1990.

[39] M. Yamaguchi et al. Evolution of axionic strings and spectrum of axions radiated from them. *Physical review letters*, 82(23):4578, 1999.

[40] R. Battye and E. Shellard. Global string radiation. *Nuclear Physics B*, 423(1):260–304, 1994.

[41] P. Sikivie. Axions, domain walls, and the early universe. *Physical Review Letters*, 48(17):1156, 1982.

[42] T. Hiramatsu et al. Axion cosmology with long-lived domain walls. *Journal of Cosmology and Astroparticle Physics*, 2013(01):001, 2013.

[43] M. Huang and P. Sikivie. Structure of axionic domain walls. *Physical Review D*, 32(6):1560, 1985.

[44] S. M. Barr et al. Some aspects of axion cosmology in unified and superstring models. *Nuclear Physics B*, 283:591–604, 1987.

[45] T. Hiramatsu et al. Production of dark matter axions from collapse of string-wall systems. *Physical Review D—Particles, Fields, Gravitation, and Cosmology*, 85(10):105020, 2012.

[46] Y. B. Zel'dovich et al. Cosmological consequences of spontaneous violation of discrete symmetry. *Zh. Eksp. Teor. Fiz.*, 40:3–11, 1974.

[47] M. Kawasaki et al. Axion dark matter from topological defects. *Physical Review D*, 91(6):065014, 2015.

[48] T. Hiramatsu et al. Evolution of string-wall networks and axionic domain wall problem. *Journal of Cosmology and Astroparticle Physics*, 2011(08):030, 2011.

[49] G. G. Raffelt. *Stars as laboratories for fundamental physics: The astrophysics of neutrinos, axions, and other weakly interacting particles.* University of Chicago press, 1996.

[50] A. Ljubičić. In search for axions. *Radiation Physics and Chemistry*, 74(6):443–453, 2005.

[51] N. Viaux et al. Neutrino and axion bounds from the globular cluster m5 (ngc 5904). *Physical Review Letters*, 111(23):231301, 2013.

[52] G. Raffelt and D. Seckel. Bounds on exotic-particle interactions from sn1987a. *Physical Review Letters*, 60(18):1793, 1988.

[53] C. O'Hare. cajohare/axionlimits: Axionlimits. `https://cajohare.github.io/AxionLimits/`, July 2020.

[54] N. Aghanim et al. Planck 2018 results-i. overview and the cosmological legacy of planck. *Astronomy & Astrophysics*, 641:A1, 2020.

[55] G. Pelletier. Fermi acceleration of astroparticles. In *Physics and Astrophysics of Ultra-High-Energy Cosmic Rays*, pp. 58–89. Springer, 2001.

[56] D. Donnelly and E. Rogers. Symplectic integrators: An introduction. *American Journal of Physics*, 73(10):938–945, 2005.

[57] I. G. Garcia and R. Petrossian-Byrne. Axion interactions with domain and bubble walls. *Journal of High Energy Physics*, 2025(4):1–39, 2025.